

A Multiphysics Numerical Framework for Epoxy Resins

Investigating Hygrothermal
Ageing in Laminated
Composites

R. J. van Leeuwen



A Multiphysics Numerical Framework for Epoxy Resins

Investigating Hygrothermal
Ageing in Laminated
Composites

by

R. J. van Leeuwen

to obtain the degree of Master of Science
at the Delft University of Technology,
to be defended publicly on Friday June 8, 2018 at 2:00 PM.

Student number: 4617355
Project duration: November 13, 2017 – June 8, 2018
Thesis committee: Dr. ir. F. P. van der Meer, TU Delft, chair & mentor
Prof. dr. ir. L. J. Sluijs, TU Delft, supervisor
I. B. C. M. Rocha, TU Delft; Knowledge Centre WMC, supervisor
Dr. M. A. Bessa, TU Delft, supervisor

An electronic version of this thesis is available at <http://repository.tudelft.nl/>.

Abstract

Epoxy resins are increasingly used in critical structural components with widespread applications in the transportation, construction and energy industries. The wind energy sector is one of the fastest growing commercial markets for epoxy resins, meaning that the structural behaviour of epoxy resins is becoming a key area of research, especially regarding its application to wind turbines. Wind turbines, particularly those in off-shore installations, are subject to a wide range of environmental conditions, most notably large variations in humidity and temperature. Both moisture and increased temperatures have been observed to have a significant impact on the stiffness and strength of epoxy resins. These environment effects, coupled with complex time dependent mechanical behaviour, means that the accurate prediction of the structural performance of epoxy resins has not yet been fully described.

This thesis presents a multiphysics framework for the simulation of hygrothermal ageing in epoxy resins. The constitutive model formulated in this thesis consists of a non-linear viscoelastic and viscoplastic mechanical model, physically coupled with a Fourier heat conduction model and a Fickian diffusion model. Degradation based on a glass transition surface is implemented to describe the multi-state behaviour of epoxy resins. To justify the model assumptions, DMA and creep tests are performed on epoxy resin specimens and their temperature dependent mechanical behaviour is established. A number of numerical benchmark tests and case studies are performed using a finite element implementation of the numerical framework. It is shown that the multiphysics framework can capture the characteristic mechanical and hygrothermal ageing behaviour exhibited by epoxy resins. Recommendations are provided for further development of the numerical model and calibration of the material properties. In a secondary study, a mesh sensitivity analysis is performed on an existing viscoelastic-viscoplastic-damage model and recommendations for an improved formulation are provided.

*R. J. van Leeuwen
Delft, June 2018*

Acknowledgements

I would like to acknowledge the people who have given me their time and support over the duration of my thesis:

My mentor and the chair of my committee, Frans van der Meer, for introducing me to the field of computational mechanics and giving me the opportunity to work on such an interesting topic. Thank you for always being available to discuss my project and for providing such positive and constructive feedback on my drafts.

Iuri Rocha, for his support throughout the entire duration of my thesis. Your willingness to promptly answer any question I had with great consideration was invaluable and the quality of your work in this field made my project much easier.

Bert Sluijs and Miguel Bessa, for providing interesting suggestions and invaluable feedback during my committee meetings, and for inspiring a rigorous academic approach.

All the people working at Knowledge Centre WMC, in particular Iuri Rocha, Sibrand Raijmaekers, Citty Visser and Francisco Lahuerta, who made the experimental component of my project possible and allowed me to use their experimental data in my thesis.

All the friends I have made working in room 6.54, for providing lively scientific discussion and for sharing the burden of thesis life.

My partner Lia, for her enormous support and meticulous proofing of my work.

Many thanks go to all the above people, without whom this thesis would not be possible.

Contents

Abstract	iii
Acknowledgements	v
1 Introduction	1
1.1 General Overview	1
1.2 Aim of the Research	2
1.3 Research Methodology.	2
1.4 Thesis Outline	3
2 Literature Review	5
2.1 Observed Behaviour of Epoxy Resin	5
2.1.1 Mechanical Behaviour	5
2.1.2 Hygrothermal Ageing Behaviour	7
2.1.3 Transport Behaviour	10
2.2 Modelling the Mechanical Behaviour of Epoxy	11
2.2.1 Deformation of Polymers	11
2.2.2 Viscoelasticity.	12
2.2.3 Viscoplasticity	14
2.2.4 Continuum Damage Mechanics.	14
2.2.5 Glass Transition Behaviour	16
2.3 Modelling the Transport Behaviour of Epoxy.	16
2.3.1 Thermal Conduction	16
2.3.2 Moisture Diffusion	17
2.4 Multiphysics Modelling	17
2.5 Existing Numerical Frameworks	18
2.5.1 Overview of the Yu Model	18
2.5.2 Overview of the Rocha Framework	18
2.6 Experimental Procedures	21
2.6.1 Dynamic Mechanical Analysis.	21
2.6.2 Creep Test	22
2.7 Conclusions.	22
3 Regularisation of the Damage Model	25
3.1 Overview of the Damage Model.	25
3.2 Mesh Dependency Study	26
3.2.1 Overview of the Analysis	26
3.2.2 Study 1: Original Damage Model	28
3.2.3 Study 2: No Plasticity After Damage.	29
3.2.4 Study 3: Zero Poisson's Ratio.	31
3.3 Conclusions and Recommendations	32

4 Experiments	35
4.1 Dynamic Mechanical Analysis	35
4.1.1 Experimental Procedure	35
4.1.2 Experimental Results	35
4.2 Creep Test.	37
4.2.1 Experimental Procedure	37
4.2.2 Experimental Results	38
5 Methods	41
5.1 Overview of the Framework	41
5.2 Formulation of the Heat Model	42
5.3 Formulation of the Diffusion Model	44
5.4 Formulation of the Mechanics Model.	45
5.4.1 Overview of the Mechanical Constitutive Models	46
5.4.2 Glass Transition Model.	46
5.4.3 Degradation Model.	48
5.4.4 Viscoelasticity Model.	49
5.4.5 Viscoplasticity	53
5.4.6 Coupled Non-Linear Viscoelasticity and Viscoplasticity.	55
5.5 Multiphysics Framework.	61
5.5.1 Heat Model	61
5.5.2 Diffusion Model	61
5.5.3 Mechanics Model.	61
6 Results	63
6.1 Validation of the Transport Model	63
6.1.1 Steady State Analysis	63
6.1.2 Transient Analysis	66
6.2 Constitutive Model 1 - Mechanics Model.	68
6.2.1 Monotonic Tension.	68
6.2.2 Loading-Unloading.	72
6.2.3 Loading-Unloading-Reloading	74
6.3 Multiphysics Model	76
6.3.1 Glass Transition Behaviour	76
6.3.2 Fatigue Test	79
6.4 Constitutive Model 2.	85
6.4.1 Loading-Unloading-Reloading	85
6.4.2 Capturing Experimental Behaviour	86
7 Conclusions and Recommendations	91
7.1 Conclusions.	91
7.2 Recommendations	93
Bibliography	97
A Material Model Mathematical Derivations	101
B Jive Implementation of the Constitutive Model	105
C MATLAB Optimisation Script for Model Calibration	109
D Experimental Data	115

List of Figures

2.1	Experimental and E-P-D model responses to a loading-unloading test with increasing amplitude [24].	5
2.2	Strain rate dependency behaviour of epoxy resin.	6
2.3	Strain rate dependency behaviour of epoxy resin.	7
2.4	Evolution of stress-strain loops during cyclic loading highlighting stress relaxation [29].	7
2.5	Creep compliance of an epoxy adhesive at different loading rates [3].	8
2.6	Degradation of shear strength with moisture saturation.	9
2.7	DMA results for neat epoxy resin samples showing the dependence of the glass transition on the moisture concentration and the dependence of the stiffness on the temperature [22].	9
2.8	Temperature of epoxy resin specimens during cyclic strain-controlled testing [32]. Note that the glass transition temperature for the test epoxy was 318 K.	10
2.9	Temperature dependence on polymer deformation rate [25].	11
2.10	Maxwell element.	12
2.11	Maxwell chain rheological model.	13
2.12	Viscoplastic rheological model.	14
2.13	Elementary damage model.	15
2.14	Domain simplification used in the implementation by Yu et al. [32].	19
2.15	Schematic representation of the multiphysics/multiscale model for hygrothermal ageing [23].	19
2.16	Schematic representation of the VE-VP-D model for epoxy resins [24].	20
2.17	Comparison of experimental results and numerical simulation for a loading-unloading-reloading test [24].	21
3.1	Response of the square geometry with the original damage model.	26
3.2	Response of the square geometry with the original damage model.	28
3.3	Response of the square geometry with the modified damage model.	29
3.4	Response of the tapered geometry with the modified damage model.	29
3.5	Constraint from the adjacent unloading elements causes transverse tensile stresses to develop in the damaging elements.	30
3.6	Transverse stresses in the damaged element for modified damage model.	30
3.7	Load displacement response of the square geometry with the modified damage model and $\nu = 0$	31
3.8	Load displacement response of the tapered geometry with the modified damage model and $\nu = 0$	32
3.9	Longitudinal strains in the undamaged elements for models with VE-VP off and VE-VP on. Square geometry with $n = 101$	33
4.1	Operating principle of the NETZSCH DMA 242 machine [19].	36
4.2	Photographs of the experimental setup and specimen.	36
4.3	Plot of the DMA parameters as a function of the temperature for each epoxy resin specimen.	36
4.4	Photograph of the a highly deformed epoxy resin specimen after a stress relaxation test.	37

4.5	Calculated elastic stiffness results from the creep test as a function of test time.	39
5.1	Overview of the multiphysics numerical framework.	41
5.2	Heat fluxes acting on a differential element.	42
5.3	Moisture fluxes acting on a differential element.	45
5.4	Glass transition diagram for an epoxy resin based on the glass transition surface used in this thesis.	48
5.5	Basis of the degradation model used in this thesis. Temperatures and corresponding degrees of glass transition relate to a dry state.	48
6.1	Problem description for the steady state heat analysis [27].	64
6.2	Steady state heat model results for varying mesh refinement and element type.	65
6.3	Heat model temperature field results for the super fine mesh refinement with QUAD8 elements.	65
6.4	Problem description for the transient heat analysis.	66
6.5	Transient heat model results at $t = 12$ s for varying element type.	67
6.6	Transient heat model results for the refined mesh at different time steps.	67
6.7	Numerical results for the constant strain rate tension tests.	70
6.8	Numerical load displacement response for the varying strain rate linear viscoelasticity tension tests.	71
6.9	Numerical stress-strain response for the varying strain rate linear viscoelasticity and viscoplasticity tension tests.	72
6.10	Numerical stress-strain response for the varying strain rate linear viscoelasticity loading-unloading tests.	73
6.11	Numerical stress-strain response for the varying strain rate linear viscoelasticity and viscoplasticity loading-unloading tests.	74
6.12	Numerical stress-strain response for the loading-unloading-reloading linear viscoelasticity and viscoplasticity tests.	75
6.13	Mesh used for the multiphysics model, showing the applied boundary conditions.	76
6.14	Contour plots of the temperature, moisture concentration and degree of glass transition for the multiphysics analysis.	77
6.15	Variation of temperature, moisture concentration and degree of glass transition with time.	78
6.16	3D mesh used for the fatigue analysis. Dimensions are identical to Figure 6.13, with a thickness of 3 mm. Boundary conditions as per Figure 6.13, except with $\omega_i = 0$ and $T_f = 298$ K.	80
6.17	Maximum temperature within the epoxy resin specimen vs. number of cycles for varying strain rates.	80
6.18	Total dissipation per cycle vs. number of cycles for varying strain rates.	80
6.19	Average temperature within the epoxy resin specimen vs. number of cycles for varying strain rates.	81
6.20	Load displacement response of the epoxy resin specimen for $\dot{\epsilon} = 0.4/s$	82
6.21	Maximum and average values of temperature and degree of glass transition within the epoxy resin specimen vs. number of cycles for $\dot{\epsilon} = 0.4/s$	82
6.22	Top surface contour plots of the temperature, longitudinal stress σ_{yy} and degree of glass transition for the fatigue analysis.	83
6.23	Equivalent plastic strain for cycle 3000 and cycle 3500.	84
6.24	Stress-strain response of an epoxy resin sample modelled with constitutive model 1 (linear viscoelasticity) and constitutive model 2 (non-linear viscoelasticity).	86

6.25	Experimental stress-strain response of an epoxy resin sample used for model calibration [24].	86
6.26	Experimental stress-strain response and calibrated numerical model using the first optimisation algorithm.	87
6.27	Experimental stress-strain response and calibrated numerical model using the second optimisation algorithm.	89
D.1	Raw experimental data from the creep test.	116
D.2	Raw experimental data from the failed stress relaxation tests at 75°C.	117

List of Tables

3.1	Material properties used in the mesh dependency analysis.	27
4.1	Dimensions of the epoxy resin specimen used in the DMA test.	35
4.2	Temperature, applied load and test duration for the creep tests.	38
4.3	Long term elastic modulus and maximum fibre stress.	40
6.1	Input for the steady state heat analysis.	63
6.2	Comparison of the steady state heat model results with Strand7 and, in parenthesis, NAFEMS.	64
6.3	Input for the transient heat analysis.	66
6.4	Comparison of the transient heat model results with Strand7 and, in parenthesis, Holman.	67
6.5	Material properties used in the mechanics model benchmark tests.	68
6.6	Temperature, moisture concentration and resulting ζ used in each constant strain rate tension test.	68
6.7	Analytical results for the constant strain rate tension test.	69
6.8	Temperature and strain rate used in each varying strain rate tension test. Note that a temperature of 298 K corresponds to $\zeta = 0$ and a temperature of 380 K corresponds to $\zeta = 1$	70
6.9	Analytical results for the varying strain rate tension test.	71
6.10	Temperature and strain rate used in each varying strain rate tension test. Note that a temperature of 298 K corresponds to $\zeta = 0$ and a temperature of 380 K corresponds to $\zeta = 1$	72
6.11	Material properties used for the multiphysics simulation investigating glass transition behaviour.	77
6.12	Material properties used for the multiphysics simulation investigating fatigue behaviour.	79
6.13	Material properties used in the non-linear viscoelastic loading-unloading-reloading tests.	85
6.14	Calibrated non-linear viscoelastic material properties using the first optimisation algorithm.	87
6.15	Calibrated non-linear viscoelastic material properties using the second optimisation algorithm.	88
D.1	Dimensions of the epoxy resin specimens used in the creep test.	115

List of Boxes

1.2.1	Numerical Research Questions	2
1.2.2	Experimental Research Questions	2
3.2.1	Verification of the Numerical Damage Results	27
5.4.1	Degradation of Linear Viscoelasticity Parameters	50
5.4.2	Degradation of Viscoplasticity Parameters	55
6.2.1	Monotonic Tension - Constant Strain Rate (VE): Analytical Results	69
6.2.2	Monotonic Tension - Varying Strain Rate (VE): Analytical Results	70
B.1	Constitutive Model Update Method	105
B.2	Coupled Return Mapping Algorithm	106

List of Symbols

Latin Symbols

A	Area	[m ²]
\mathbf{B}	Spatial derivative of FE shape functions	
\mathbf{b}	Body force vector	[N / m ³]
C	Compliance modulus	[m ² / N]
\mathbf{C}	Compliance matrix	
c	Specific heat capacity	[J / (kg · K)]
c_2	Non-linear viscoelastic material parameter	[-]
c_3	Non-linear viscoelastic material parameter	[-]
\mathbf{c}_h	Heat model damping matrix	
\mathbf{c}_ω	Diffusion model damping matrix	
\mathbf{D}	Mechanical constitutive matrix	
\mathbf{D}^e	Elastic mechanical constitutive matrix	
\mathbf{D}^{ve}	Viscoelastic mechanical constitutive matrix	
\mathbf{D}_∞	Long term mechanical constitutive matrix	
\mathbf{D}_ω	Diffusivity matrix	
D_ω	Moisture diffusivity	[m ² / s]
d	Damage variable	[-]
d_ω	Moisture degradation factor	[-]
d_ω^∞	Moisture degradation factor at saturation	[-]
d_{ve}	Non-linear viscoelastic multiplier	[-]
E	Elastic modulus	[N / m ²]
E'	Storage modulus	[N / m ²]
E''	Loss modulus	[N / m ²]
\mathcal{E}	Total strain vector	[-]
E_∞	Long term elastic modulus	[N / m ²]
F	Force	[N]
F_f	Force at failure	[N]
F_y	Force at yield	[N]
\mathbf{f}	Vector of forces	[N]
\mathbf{f}_b	Vector of applied body forces	[N]
f_d	Fracture surface	
\mathbf{f}_t	Vector of applied tractions	[N]
f_{obj}	Objective function used for global minimisation	
f_p	Yield surface	
f_{ve}	Non-linear viscoelastic yield surface	
g	Non-linear viscoelastic function	
G	Shear modulus	[N / m ²]
G^*	Fracture energy like parameter	[N / m]
G_{ve}	Viscoelastic shear modulus	[N / m ²]
\hat{G}	Total elastic shear modulus	[N / m ²]
H	Parameter describing glass transition range	[N / m ²]

H_c	Derivative of σ_c with respect to ε_{eq}^p	[N / m ²]
H_c	Derivative of σ_t with respect to ε_{eq}^p	[N / m ²]
h	Coefficient of heat transfer	[J / (s · m ² · K)]
\mathbf{h}_h	Heat model convective stiffness matrix	
I	Second moment of inertia	[m ⁴]
I_1	First invariant of the stress vector	[N / m ²]
I_1^{tr}	First invariant of the trial stress vector	[N / m ²]
i, k	Increment variables	
\mathbf{j}	Moisture flux vector	[m / s]
J_2	Second invariant of the deviatoric stress vector	[N ² / m ⁴]
J_2^{tr}	Second invariant of the deviatoric trial stress vector	[N ² / m ⁴]
K	Bulk modulus	[N / m ²]
K_{ve}	Viscoelastic bulk modulus	[N / m ²]
\widehat{K}	Total elastic bulk modulus	[N / m ²]
\mathbf{k}_h	Heat model stiffness matrix	
\mathbf{k}_m	Mechanics model stiffness matrix	
\mathbf{k}_ω	Diffusion model stiffness matrix	
L	Length	[m]
l_e	FE characteristic length	[m]
M	Bending moment	[N · m]
m_p	Viscoplastic exponent	[-]
m_{ve}	Viscoelastic exponent	[-]
\mathbf{N}	FE shape functions	
N	Number of viscoelastic stiffnesses	
\mathbf{n}	Unit vector normal to a boundary	[-]
p^{ve}	Volumetric viscoelastic stress	[N / m ²]
Q	Rate of heat generation per unit volume	[J / (m ³ · s)]
Q_{int}	Rate of internal heat generation per unit volume	[J / (m ³ · s)]
\mathbf{q}	Heat flux vector	[J / (m ² · s)]
q_i	Prescribed heat flux	[J / (m ² · s)]
$\mathcal{R}(x)$	Memory function	
r	Variable relating to the size of the fracture surface	
\mathbf{r}_h	Prescribed convective heat vector	[J / s]
\mathbf{r}_j	Prescribed moisture flux vector	[1 / s]
\mathbf{r}_q	Prescribed heat flux vector	[J / s]
\mathbf{r}_Q	Prescribed internal heat generation vector	[J / s]
\mathbf{S}	Deviatoric stress vector	[N / m ²]
\mathbf{S}^{tr}	Deviatoric trial stress vector	[N / m ²]
\mathbf{S}^{ve}	Deviatoric viscoelastic stress vector	[N / m ²]
T	Temperature	[K]
T_0	A reference temperature	[K]
T_f	Ambient fluid temperature	[K]
T_g	Glass transition temperature	[K]
T_i	Prescribed temperature	[K]
T_{init}	Initial temperature	[K]
t	Time	[s]
\mathbf{t}_h	Traction vector	[N / m ²]
u	Displacement	[m]
\mathcal{V}	Space of admissible weight functions	

W	Elastic section modulus	[N · m ³]
w	A scalar weight function	
X_c	Compressive fracture strength	[N / m ²]
X_t	Tensile fracture strength	[N / m ²]
x, y, z	Spatial coordinates	[m]

Greek Symbols

α	Plastic flow direction	
α_ω	Coefficient of moisture expansion	[-]
α_T	Coefficient of thermal expansion	[1/K]
Γ	Return mapping non-linear viscoelasticity function	
Γ_h	Boundary with a convective boundary condition	
Γ_j	Boundary with a moisture flux boundary condition	
Γ_q	Boundary with a heat flux boundary condition	
Γ_T	Boundary with a prescribed temperature	
Γ_t	Boundary with an applied traction	
Γ_{tol}	Return mapping non-linear viscoelasticity tolerance	
γ	Plastic multiplier	[m ² / N]
$\tan \delta$	Loss factor	[-]
ε	Strain	[-]
$\boldsymbol{\varepsilon}^e$	Elastic strain vector	[-]
$\boldsymbol{\varepsilon}^d$	Deviatoric elastic strain vector	[-]
ε_v	Volumetric elastic strain	[-]
$\boldsymbol{\varepsilon}^p$	Plastic strain vector	[-]
ε_{eq}^p	Equivalent plastic strain	[-]
$\boldsymbol{\varepsilon}_\omega$	Moisture swelling strain vector	[-]
$\boldsymbol{\varepsilon}_T$	Thermal expansion strain vector	[-]
ζ	Degree of glass transition	[-]
ζ_p	Volumetric plastic correction factor	[-]
ζ_s	Deviatoric plastic correction factor	[-]
η	Dashpot viscosity	[N · s / m ²]
η_p	Viscoplastic modulus	[N · s / m ²]
Θ	A material parameter	
κ	Thermal conductivity	[J / (s · m · K)]
$\Lambda \boldsymbol{\sigma}^{ve}$	Decayed historical viscoelastic stress vector	[N / m ²]
Λ_b	Chemical modulus related to bound moisture	[1 / s]
Λ_f	Chemical modulus related to free moisture	[1 / s]
λ	Relaxation time	[s]
λ_k	Bulk relaxation time	[s]
λ_g	Shear relaxation time	[s]
ν	Poisson's ratio	[-]
ν_∞	Long term Poisson's ratio	[-]
ν_p	Plastic Poisson's ratio	[-]
Ξ	Dissipation	[N / (m ² · s)]
Ξ^{ve}	Viscoelastic dissipation	[N / (m ² · s)]
Ξ^p	Viscoplastic dissipation	[N / (m ² · s)]
ξ	Non-linear viscoelastic parameter	[-]
π_c	A constant related to the glass transition surface	[N / m ²]

π_{tr}	Thermodynamic driving force of ζ	[N / m ²]
ρ	Density	[kg / m ³]
σ	Stress	[N / m ²]
σ^e	Elastic stress vector	[N / m ²]
σ^{ve}	Viscoelastic stress vector	[N / m ²]
σ^{tr}	Trial stress vector	[N / m ²]
σ_c, σ_t	Compressive and tensile yield strength respectively	[N / m ²]
σ^0	Yield strength at zero equivalent plastic strain	[N / m ²]
$\bar{\sigma}$	Equivalent Von Mises stress	[N / m ²]
σ_0	Stress at onset of non-linear viscoelasticity	[N / m ²]
σ_d	Stress at onset of damage	[N / m ²]
σ_f	Stress at onset of complete failure	[N / m ²]
σ_{eq}	Equivalent stress measure used in the damage model	[N / m ²]
σ_{num}	Stress obtained from a numerical analysis	[N / m ²]
σ_{exp}	Stress obtained from an experimental procedure	[N / m ²]
τ	An arbitrary time	[s]
Φ	Return mapping viscoplasticity function	
Φ_{tol}	Return mapping viscoplasticity tolerance	
Φ_{tr}	Glass transition surface	
ϕ_1	Non-linear viscoelasticity onset parameter	[N / m ²]
ϕ_2	Non-linear viscoelasticity plastic strain parameter	[-]
ϕ_ω	Moisture concentration glass transition parameter	[N / m ²]
ϕ_T	Temperature concentration glass transition parameter	[N / m ²]
Ω	Domain of a finite element model	
ω	Moisture concentration	[-]
ω_b	Moisture concentration of bound moisture	[-]
ω_f	Moisture concentration of free moisture	[-]
ω_l	Loading frequency	[1/s]

Other Symbols and Conventions

a, A	Italics denotes a scalar
\mathbf{a}	Lowercase bold denotes a vector
\mathbf{A}	Uppercase bold denotes a matrix
\dot{a}	Time derivative of a
δ_{ij}	Kronecker delta
δa	Denoting a small change in a
Δa	Denoting a change in a
$\mathbf{a} \cdot \mathbf{b}$	Dot product of vectors \mathbf{a} and \mathbf{b}
$\text{tr}(\mathbf{a})$	Trace of vector \mathbf{a}
$\mathbf{a}^T, \mathbf{A}^T$	Transpose of vector \mathbf{a} or matrix \mathbf{A}
∇a	Gradient of scalar a
$\nabla \cdot \mathbf{a}$	Divergence of vector \mathbf{a}
$\mathbf{a} \otimes \mathbf{b}$	Dyadic product of vector \mathbf{a} and \mathbf{b}
\mathbf{I}	Second order identity tensor
\mathbf{I}	Fourth order identity tensor
$\langle a \rangle$	Macaulay brackets
a_e	Value of a for the e^{th} element
a^{gla}	Value of a for an epoxy resin in a glassy state

a^{rub}	Value of a for an epoxy resin in a rubbery state
\tilde{a}	Effective value of a (damage model)
\mathbb{A}	Assembly operator

Abbreviations

E	Elasticity Model
P	Plasticity Model
VE	Viscoelasticity Model
VP	Viscoplasticity Model
D	Damage Model
E-P-D	Elastic-Plastic-Damage Model
VE-VP	Viscoelastic-Viscoplastic Model
VE-VP-D	Viscoelastic-Viscoplastic-Damage Model
DMA	Dynamic Mechanical Analysis
RVE	Representative volume element

Introduction

1.1. General Overview

The use of *laminated composites* is widespread amongst many industries, notably in the transportation, construction and energy sectors. Laminated composites provide many advantages over traditional materials. They are lightweight, have exceptional specific stiffness and strength characteristics and can be easily moulded into complex shapes [1]. Glass/epoxy composites, more commonly referred to as fibreglass, are one of the most prominent laminated composites and commonly consist of a woven glass fibre sheet thermoset into an epoxy polymer matrix. One of the prevalent applications of glass/epoxy composites is their use in the construction of wind turbines.

The wind energy sector is experiencing unprecedented growth [12] sparked by policies aimed towards the reduction of fossil fuel dependency. In Europe alone, the offshore wind energy capacity is forecast to expand by up to 21% annually [10]. Glass/epoxy composites are becoming a primary focus for scientific research due to the fact that they are the most common material used in the construction of wind turbine blades. Further, they are also the most expensive component of a wind turbine [18]. A primary focus of current research in wind turbine development is concerned with the structural optimisation of the blades, particularly in offshore installations, where increasing the blade size results in a reduced cost of energy [18]. Further research relating to the micro-mechanical behaviour of glass/epoxy composites builds on the optimisation philosophy, aiming to reduce the uncertainty associated with the structural design of these blades. With wind turbine blades designed to be in operation for up to 25 years, the high-cycle fatigue design of glass/epoxy composites is of particular importance.

In the offshore environment wind turbine blades are subjected to extreme environmental conditions, such as large variations in humidity and temperature as well as other undesirable environmental processes. The combined influence of thermal and moisture ingress has a significant impact on the fatigue life of glass/epoxy composite materials [5, 13] and is an ongoing area of research in the energy industry. Although this *hygrothermal ageing* process is a complex interaction between all the constituents of a laminated composite, understanding the behaviour of each individual component is crucial in quantifying fatigue behaviour.

This thesis focuses on the material behaviour of *epoxy resin*, which forms the matrix that binds a laminated composite together. Rigorous constitutive modelling of epoxy resins involves considering a multitude of complex time dependent mechanical and hygrothermal behaviour. While there have been many attempts to quantify this complex behaviour on an individual level, few have successfully unified the time dependent mechanical behaviour with coupled hygrothermal effects.

1.2. Aim of the Research

The intent of this research is to develop a constitutive numerical framework that accurately describes the physical behaviour of epoxy resins in order to better quantify the process of hygrothermal ageing. This thesis seeks to build upon the constitutive model developed by Rocha et al. [23, 24] by improving and expanding elements of the model that do not accurately represent the physical behaviour of epoxy resins.

A cursory study of the existing constitutive model by Rocha et al. has identified the following research questions as a formulaic approach in achieving the numerical aims of this thesis:

Numerical Research Questions

1. How well does the existing damage model address the issue of mesh dependency?
2. How can the existing constitutive model be extended to account for thermal effects?
3. How can the existing constitutive model be improved to better represent the elastic behaviour at large strains?
4. How well does the new constitutive model capture observed phenomena relating to the mechanical and hygrothermal ageing behaviour of epoxy resins?

Further to these numerical research questions, the following experimental research questions were formulated to provide experimental confirmation of the model assumptions and to instigate calibration of the material parameters:

Experimental Research Questions

5. What effect does temperature have on the stiffness of the epoxy resin system?
6. What are the long term stiffness properties of the epoxy resin system in different material states?

1.3. Research Methodology

Numerical Research

The numerical work in this thesis consists of the formulation of a *multiphysics* constitutive model, model implementation and model validation. The model formulation is predominantly theoretically grounded and, therefore, an extensive literature review is first undertaken to examine the behaviour of epoxy resins and the mathematical models used to describe this behaviour. The formulation adapts models from the literature describing individual material behaviour and combines them in an overarching numerical framework. The formulated numerical models are then implemented in the context of the finite element method and are programmed in C++ using the Jive programming toolkit. In this thesis, an existing finite element framework developed by Rocha et al. [23, 24] is adapted and new models are programmed to implement the developed constitutive models. Finally, the model formulation and implementation are validated by undertaking a series of numerical benchmark tests and case studies. The validation stage verifies the suitability of the implementation and highlights the capabilities of the formulated constitutive models.

Experimental Research

To answer the experimental research questions, two different types of tests are undertaken on a typical epoxy resin system. A dynamic mechanical analysis with a temperature sweep is performed to investigate the temperature dependent stiffness of the epoxy resin. Numerous creep tests are carried out to quantify the long term stiffness properties of the epoxy resin.

1.4. Thesis Outline

This thesis is structured such that the research questions are addressed in a logical manner. *Section 2* presents a critical review of the literature related to the observed behaviour of epoxy resins and the numerical tools that can be used to describe this behaviour. This section also assesses some of the existing numerical frameworks that are used to model epoxy resins and provides an overview of the theoretical background to the experimental procedures used in this thesis. *Section 3* focusses on the first research questions relating to the mesh dependency of the damage model. *Section 4* describes the experiments undertaken in this thesis relating to the fifth and sixth research questions and presents the results in order to provide context for the model formulation. In *Section 5* the new constitutive model is developed, addressing the second and third research questions. The mathematical and algorithmic aspects of the constitutive model are discussed in detail. *Section 6* addresses the fourth research question by presenting and discussing results relating to numerical model validations and physical case studies. Finally, *Section 7* summarises the findings of this thesis and presents recommendations for further research related to this topic.

2

Literature Review

2.1. Observed Behaviour of Epoxy Resin

In this section, key features of the mechanical behaviour of epoxy resins are described in order to enable the construction of a realistic constitutive model. The epoxy resin that is studied in this thesis, as well as by Rocha et al. [22–24], is the Momentive RIMR 135/EPIKURE RIMH 1366, with a ratio between the monomer and hardener of 100:30 in weight.

2.1.1. Mechanical Behaviour

The mechanical behaviour of epoxy, and polymers in general, is complex due to the fact that its response is time dependent. Unlike traditional construction materials, such as steel, timber and aluminium, capturing the time dependent behaviour of epoxy resins plays an important role in quantifying its material failure. Figures 2.1a and 2.1b show the typical mechanical response of epoxy resin and highlight its deviation from a traditional elasto-plastic damage (E-P-D) model.

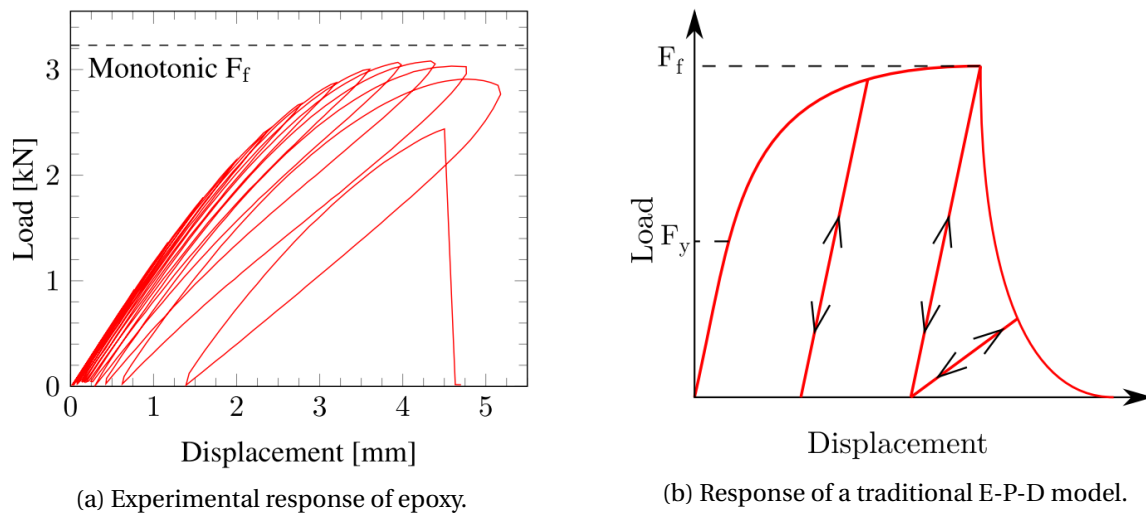
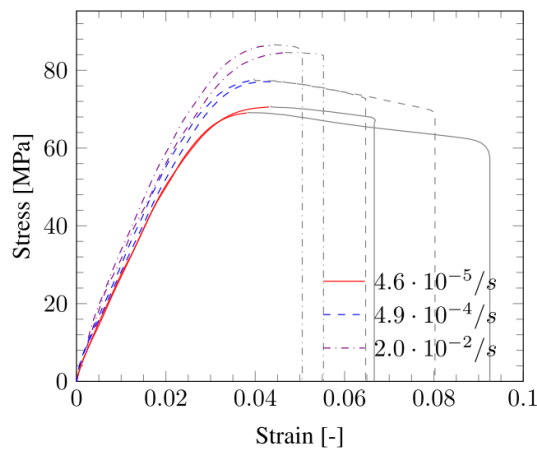


Figure 2.1: Experimental and E-P-D model responses to a loading-unloading test with increasing amplitude [24].

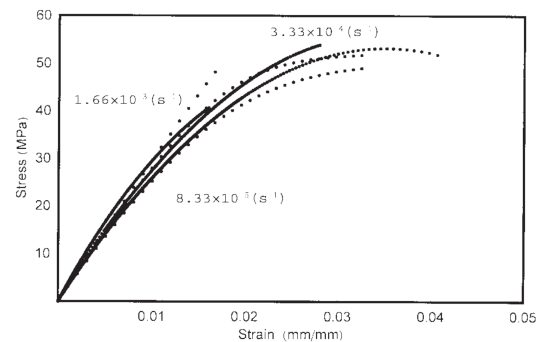
In Figure 2.1b it can be seen that a traditional E-P-D model responds in a linear manner up to the yield point of the material, F_y . After yield, the plasticity model causes a hardening response until failure occurs at F_f . Before failure, unloading and reloading occur elastically, with the model following a path matching the initial elastic stiffness. After reloading, the E-P-D model intersects

the load-displacement curve at the point at which unloading began. After this intersection, the monotonic response is once again followed. It is apparent that the mechanical behaviour of epoxy resin, summarised in Figure 2.1a, does not exhibit this loading-reloading behaviour and, as such, cannot be described by a traditional E-P-D model. Because of this, the features that distinguish the mechanical response of epoxy resin from a traditional E-P-D model are investigated in further detail below.

Epoxy resins, as well as most thermoset polymers, exhibit a strain rate dependency in their mechanical response. Figures 2.2a and 2.2b show that an increase in the strain rate results in an increase in stiffness and failure strength. Figure 2.2a shows that this behaviour is also accompanied by a reduction in the failure strain. This strain rate dependency of the epoxy resin can be attributed to its behaviour at polymer level [15].



(a) Response of epoxy to a quasi-static tension test [24].



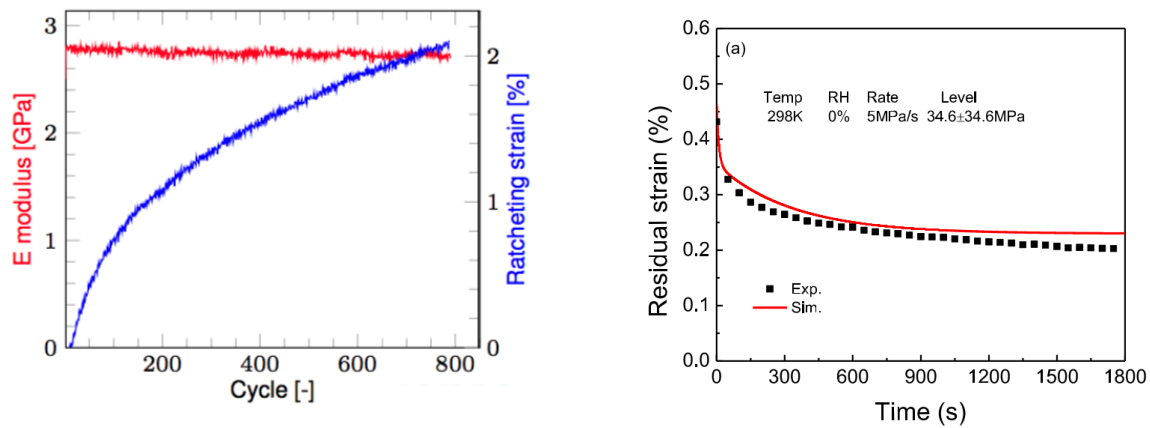
(b) Tensile stress-strain response of epoxy at three different strain rates (thick lines are experimental data) [15].

Figure 2.2: Strain rate dependency behaviour of epoxy resin.

Ratcheting, which relates to strain accumulation during cyclic loading, is a significant, yet complex, phenomenon that occurs in epoxy resins. Ratcheting in traditional materials is generally attributed to the accumulation of plastic strains. However, in the case of materials with significant time dependent behaviour, a component of ratcheting strains can originate from an elastic source [24, 28]. While the elastic ratcheting strain component does not have a direct effect on the fatigue behaviour of epoxy resins [28], isolating the ratcheting component related to plastic strain accumulation is crucial in predicting fatigue failure [32]. Figure 2.3a shows that the non-linear development of ratcheting strain can occur without any appreciable reduction in elastic stiffness. Figure 2.3b shows that the ratcheting strain is composed of a recoverable elastic component and an accumulating, non-recoverable plastic component.

While the phenomenon of ratcheting is observed during load controlled tests, stress relaxation occurs during displacement controlled testing and relates to the relief of stress under constant strain. In a cyclic displacement controlled loading of an epoxy resin, it is observed that the mean stress reduces with time [29]. In a cyclic test that involves only tensile strains, stress relaxation results in the development of compressive stresses at the end of the unloading cycle, which can occur without plastic strains. This behaviour is described in Figure 2.4. As with ratcheting, the stress relaxation in epoxy resins can be a result of both elastic and plastic behaviour, which must be isolated in order to quantify its effect of fatigue failure.

Significant hysteresis is observed during the cyclic loading of epoxy resins at high stresses and/or strains. From Figure 2.1a, it can be seen that the unloading branches form increasingly larger hysteresis loops, the concavity of which changes from concave at smaller strains to convex at larger



(a) Development of ratcheting strain and instantaneous elastic modulus during cyclic testing [24].

(b) Relaxation of ratcheting strain at zero stress after cyclic stress-controlled deformation [32].

Figure 2.3: Strain rate dependency behaviour of epoxy resin.

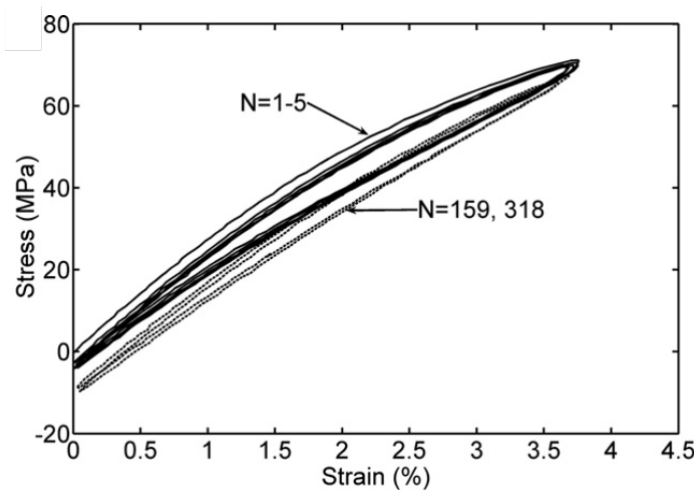


Figure 2.4: Evolution of stress-strain loops during cyclic loading highlighting stress relaxation [29].

strains [32]. The size of the hysteresis loop is related to the total amount of dissipation that is caused by the viscous and plastic mechanical processes. Therefore, correctly quantifying this behaviour is critical for models in which dissipation is linked to damage [23, 24] or multiphysical processes [32].

The combination of ratcheting and a relatively low elastic modulus means that polymers can often experience relatively large elastic deformations. As a result, non-linearities in the elastic behaviour can become apparent in the material response as the strain level increases [3]. This non-linear behaviour typically originates above a certain stress level after which the stress-strain curves begin to deviate from linearity. Figure 2.5 shows the compliance of an epoxy adhesive as a function of the stress level, for different loading rates. This figure highlights the softening of the epoxy above a certain stress threshold, which is also dependent on the loading rate.

2.1.2. Hygrothermal Ageing Behaviour

Fatigue failure at relatively low stress levels has been linked to water absorption and large variations in temperature [5]. This is often referred to as hygrothermal ageing and can affect the glass fibres, the epoxy matrix and also the fibre-matrix interface in multiple ways. The behaviour of the epoxy

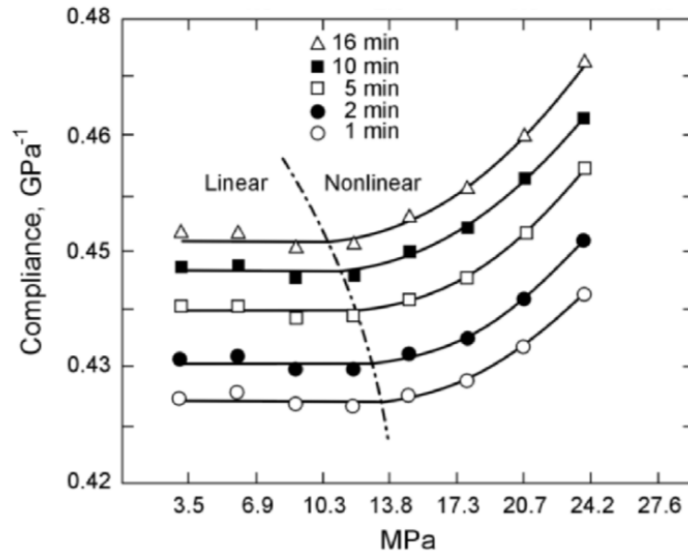
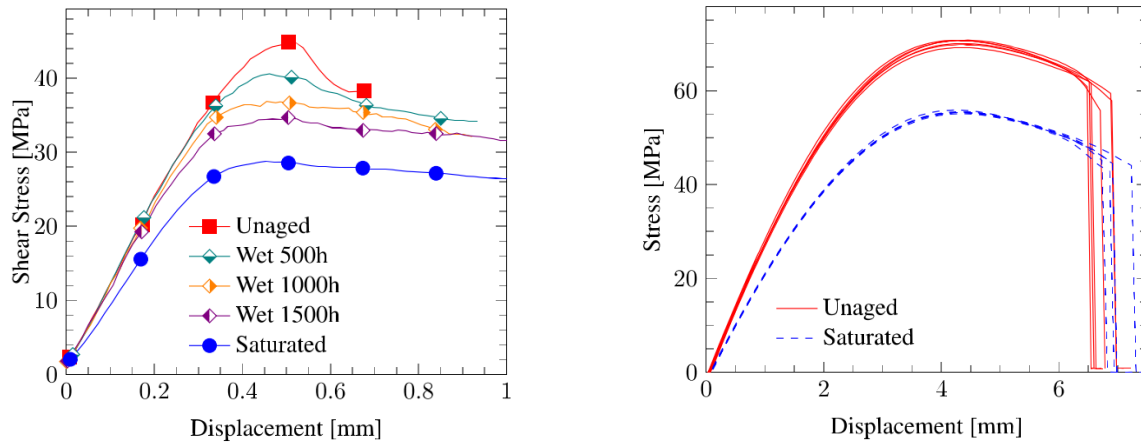


Figure 2.5: Creep compliance of an epoxy adhesive at different loading rates [3].

polymer matrix in particular, is a result of a diversity of chemical and structural effects, presenting an array of complex challenges when attempting to understand the degradation behaviour [13]. For example, an increase in the temperature of the composite tends to soften and weaken its mechanical response [26], while an increase in the moisture content typically plasticises the epoxy matrix, reducing the observed modulus and strength [13].

Rocha, et al. [22] performed a number of experiments on specimens consisting of a glass/epoxy composite and a neat epoxy resin, in order to investigate the degradation processes caused by the ingress of water and variation in temperature. When investigating the effect of moisture ingress, saturated specimens showed a significant decrease in mechanical strength. The composite specimens exhibited a 36% loss in shear strength and its fatigue life was reduced by three orders of magnitude. The neat epoxy resin specimens experienced a less pronounced deterioration, with a 17% reduction in tensile modulus, bending modulus, and strength (see Figures 2.6a and 2.6b). Both the composite and neat epoxy specimens were also completely redried after saturation and were retested. The redried composite specimens did not fully recover their shear strength and stiffness. In contrast, the redried neat epoxy resin specimens experienced a full recovery of both their stiffness and bending strength, however they experienced a reduction in their failure strain.

It was proposed by Rocha et al. [22] that saturation of composite glass/epoxy specimens results in the occurrence of significant differential swelling stresses caused by differences in material behaviour within the composite. Repeated cycles of water absorption and desorption can induce fatigue damage in laminated composites, greatly reducing the service life of a wind turbine blade [5]. Further, it was also concluded by Rocha et al. that the moisture induced degradation of the epoxy matrix further contributed to observed reductions in mechanical and fatigue strengths. This degradation is the result of the absorbed water acting as a plasticiser, softening the epoxy matrix, which, in most cases, is a reversible process after drying [13]. Further, the absorption of moisture acts to reduce the observed *glass transition temperature* [13], which is the point at which a state change occurs within a material, resulting in a significant change in its mechanical behaviour [25]. This behaviour was also found in the tests on the epoxy resin by Rocha et al., in which the glass transition temperature was significantly influenced by the moisture level of the specimen. Rocha et al. determined the glass transition temperature of the Momentive RIMR 135/EPIKURE RIMH 1366 epoxy resin to be 90.3°C for dry specimens and 70.0°C for saturated specimens.



(a) Static ILSS test on glass/epoxy composite specimens with varying saturations [22].

(b) Static ILSS test on unaged and saturated neat epoxy resin specimens [22].

Figure 2.6: Degradation of shear strength with moisture saturation.

The effect of moisture content on the glass transition temperature depends strongly on the epoxy resin system used. In the study by Choi et al. [5], it was found that the glass transition temperature linearly decreased with increasing moisture content. However, in the experiments performed by Chen et al. [4], a square root relationship between the degree of glass transition and the moisture content was adopted.

The thermal testing by Rocha et al. [22] showed that there was a significant change in the mechanical response of the neat epoxy resin once the temperature of the specimen approached the glass transition temperature. Figure 2.7 presents the storage modulus¹ of a neat epoxy resin specimen as a function of the temperature of the specimen. It is clear that, at elevated temperatures, the epoxy resin loses a significant portion of its stiffness. Further, Yu et al. note that the yield strength of polymers is typically degraded by a similar amount [32].

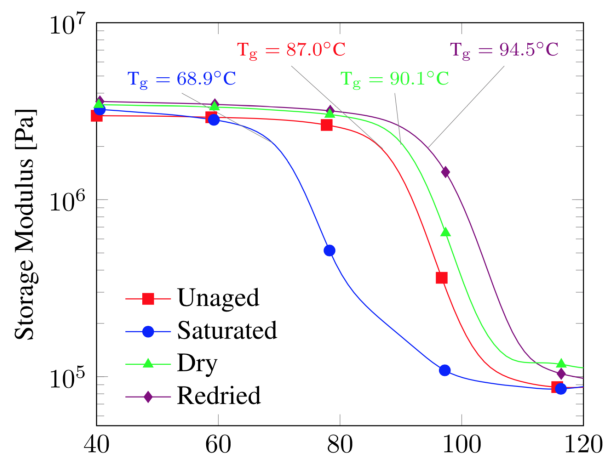


Figure 2.7: DMA results for neat epoxy resin samples showing the dependence of the glass transition on the moisture concentration and the dependence of the stiffness on the temperature [22].

¹The storage modulus is analogous to the elastic modulus, see Section 2.6.1.

2.1.3. Transport Behaviour

The heat conduction behaviour of epoxy resins is assumed by most authors [8, 32] to be isotropic and to follow Fourier's law of heat conduction. Humidity dependent heat transfer was observed in experiments by Chen et al. [4], in which the thermal conductivity was found to be a linear function of the moisture content. However, the significance of the effect was found to be quite weak in the work by Yu et al. [32], in which a 5% increase in the conductivity was modelled from the dry state to the saturated state. The coupling of heat conduction with mechanical behaviour is also present because viscous elastic and plastic deformations result in internal energy dissipation [25, 32]. These dissipations can be interpreted as an internal heat source within the material. Chen et al. [4] observed this phenomenon by measuring the temperature of epoxy resin specimens subjected to increasing strain rates, observing that a large enough strain rate can induce glass transition. This observed behaviour significantly accelerates the hygrothermal ageing process, see Figure 2.8.

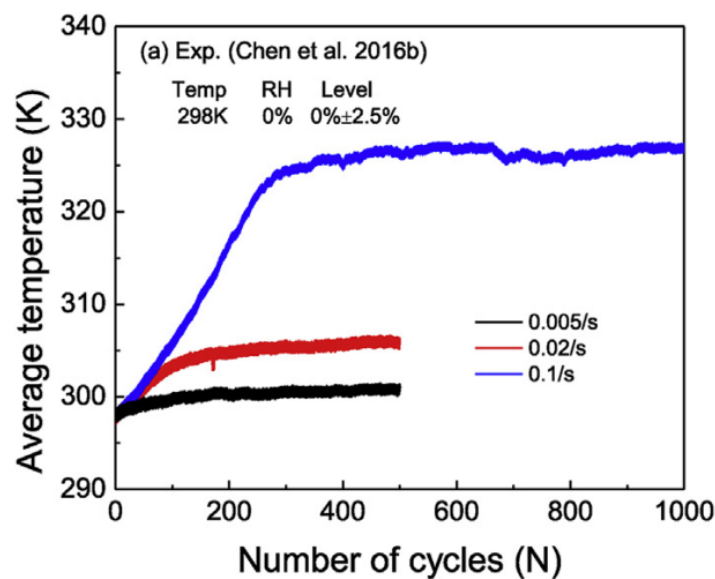


Figure 2.8: Temperature of epoxy resin specimens during cyclic strain-controlled testing [32]. Note that the glass transition temperature for the test epoxy was 318 K.

In studying the moisture diffusion behaviour of the Momentive RIMR 135/EPIKURE RIMH 1366 epoxy resin system, Rocha et al. [22] found the saturation moisture content to be approximately 3.94%. It was concluded that the diffusion behaviour of the epoxy could be accurately represented by Fick's first and second laws of diffusion. This model has been adopted by others authors for similar epoxy resin systems [13]. It was noted, however, that for the current epoxy resin system, part of the water could not be removed through redrying. This indicates that a proportion of the water molecules form chemical bonds with the polymer network. This behaviour is consistent with a Langmuir type non-Fickian diffusion model, also commonly used for modelling the moisture diffusion behaviour within epoxy resin specimens [5, 32]. In this model, the total moisture content is decomposed into a component consisting of free water molecules and a component related to water molecules that are chemically bonded to the polymer network. This diffusion behaviour is consistent with epoxy resins that show different rates of moisture uptake at different temperatures, such as in the epoxy studied by Choi et al. [5]. However, the moisture diffusion behaviour at elevated temperatures has not been studied for the current epoxy resin system, and, as such the extent to which the epoxy resin studied in this thesis is non-Fickian has not been ascertained.

2.2. Modelling the Mechanical Behaviour of Epoxy

This section introduces the various modelling components that are used to numerically describe the behaviour of an epoxy resin used in a glass/epoxy composite material. An epoxy resin is a type of polymer and, as such, exhibits a viscoelastic and viscoplastic response [17, 25]. Both viscoelasticity and viscoplasticity are crucial elements when quantifying the hygrothermal fatigue behaviour of a glass/epoxy composite [23]. Further to this, once a particular stress level has been reached, a continuum damage approach can be used to model the initiation and propagation of micro-cracks within the epoxy matrix [17, 24]. Finally, degradation of the epoxy due to thermal and moisture effects can be captured through the incorporation of a glass transition model [32].

2.2.1. Deformation of Polymers

Polymers typically behave through a combination of two different molecular mechanisms: a distortion or stretching of the chemical bonds between the atoms, which is referred to as elastic solidity, and a larger-scale rearrangement of the molecular chains of the polymer, which relates to viscous fluidity [25]. These two types of deformation occur at very different time scales. The bond stretching occurs almost instantaneously, while the molecular rearrangement is a much slower process, the rate of which depends heavily on the temperature of the polymer. The mechanical behaviour of any polymer can be described by three main states that relate to these modes of deformation: a glassy state, which exists at lower temperatures and whose deformation consists only of instantaneous elastic solidity; a rubbery state, which exists at higher temperatures and whose deformation consists solely of slower viscous fluidity; and a leathery or mixed glassy-rubbery state, which exists close to the glass transition temperature and with a deformation that is a combination of elastic solidity and viscous fluidity. Refer to Figure 2.9 for a representation of the deformation rates of the three different material states.

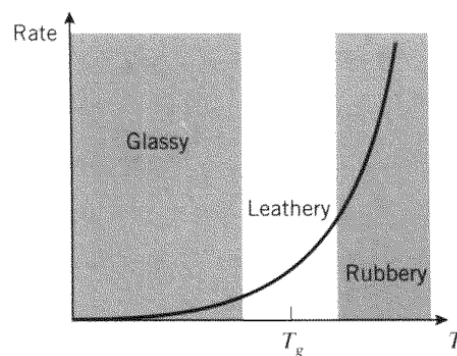


Figure 2.9: Temperature dependence on polymer deformation rate [25].

Epoxy resins used in glass/epoxy composites generally exist in a state relatively close to the glass transition temperature under typical service conditions. As a result of this mixed state, time effects can be significant [25] and modelling this time dependent behaviour is critical for the accurate description of the mechanical deformation of epoxy resins. The modelling approach that is adopted in this thesis uses viscous mechanical models to describe the elastic and plastic behaviour of epoxy resins and is described in detail in Sections 2.2.2 and 2.2.3.

An alternative approach that is gaining in popularity owing to increasing computational power, is the use of multiscale molecular dynamics modelling. In this approach, nano-scale models of the cross-linked polymer chains are constructed and a molecular dynamics simulation is used to obtain homogenised continuum mechanical properties [30]. The advantage of these molecular dynamics models over the more traditional viscous models is that the physical atomistic behaviour of the material is captured. As a result, model parameters with seemingly no physical interpreta-

tion, such as some of the parameters used in non-linear viscoelasticity models, are avoided. Another significant advantage is that these models have the ability to inherently capture temperature dependent behaviour under general stress states. For example, Vu-Bac et al. [30] obtained temperature dependent elastic moduli and yield surfaces from molecular dynamics simulations that were experimentally validated for temperatures below the glass transition. Further, the use of nanoscale simulations can allow for model calibration without the need for physical experiments. For example, material parameters used in viscous continuum models could be obtained numerically using a number of multiscale molecular dynamics simulations, significantly improving the speed and reducing the cost of model calibration.

Although the use of molecular dynamics simulations is outside the scope of this thesis, its application has the potential to build on the work presented in this thesis and is thus referenced in the discussion of the numerical results and the recommendations for future work.

2.2.2. Viscoelasticity

To build a viscoelastic model for epoxy resins, first a simple model is considered. One of the most basic viscoelastic models is the Maxwell element, which consists of a spring and dashpot in series, see Figure 2.10.



Figure 2.10: Maxwell element.

After decomposing the strain rate into an elastic and viscous component, and substituting the relevant constitutive relations, a single order differential equation is obtained in terms of the stress [7]:

$$\dot{\epsilon} = \frac{\dot{\sigma}}{E} + \frac{\sigma}{\eta} \quad (2.1)$$

where E is the stiffness of the spring and η is the viscosity of the dashpot. Given an initial strain ϵ_0 , the resulting stress behaves according to an exponential decay function:

$$\sigma(t) = E\epsilon_0 \exp\left(\frac{-t}{\lambda}\right) \quad (2.2)$$

where $\lambda = \frac{\eta}{E}$ is defined as the relaxation time. This very simple model captures some of features that were described in Section 2.1.1, most notably strain-rate dependency and stress relaxation, and, to a lesser degree, ratcheting and hysteresis. To build upon this model, it should be noted that the physical behaviour of a polymer consists of many relaxation times. This is because each molecular chain has a different length within a polymer. As a result, each molecular chain also has its own relaxation time, with shorter chains relaxing faster than longer ones [25]. Numerically, this behaviour can be well represented by a finite number of Maxwell elements in a parallel arrangement, each with their own stiffness E_i and relaxation time λ_i [7]. Often, the first element in this chain has an infinitely large relaxation time, corresponding to a spring which represents the long term stiffness of the material, E_∞ , see Figure 2.11.

While Equation 2.2 relates to a single imposed initial strain, a generic numerical model must consider an arbitrary strain history. Therefore, an integration of all the previous strain states must be performed to determine the stress at any given time. De Borst et al. [7] explain that this is computationally undesirable because all previous strain increments need to be stored and operated on

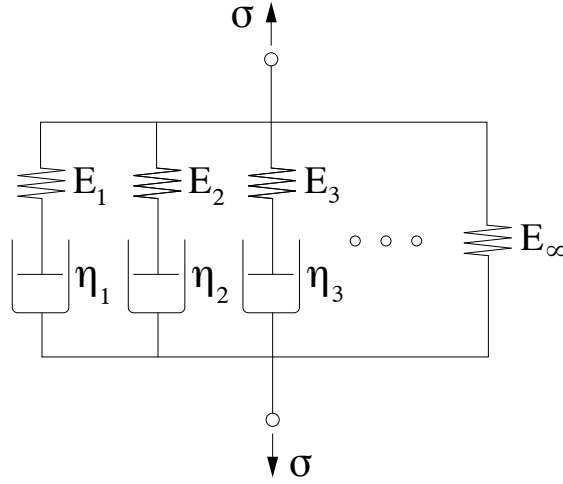


Figure 2.11: Maxwell chain rheological model.

in order to determine the new stress increment. One possible method to avoid this computation involves manipulating the integral such that only a finite number of state variables from the previous time step need to be stored [7]. This manipulation results in the following expression for the stress increment $\Delta\sigma$ of a Maxwell chain model:

$$\Delta\sigma = \mathbf{D}_\infty \Delta\epsilon^e + \sum_{i=1}^N \left[1 - \exp\left(-\frac{-\Delta t}{\lambda_i}\right) \right] \left[\frac{\lambda_i}{\Delta t} \mathbf{D}_i \Delta\epsilon^e - \sigma_i(t - \Delta t) \right] \quad (2.3)$$

where \mathbf{D}_∞ and \mathbf{D}_i are the long term and viscoelastic stiffnesses, $\Delta\epsilon^e$ is the elastic strain increment and $\sigma_i(t - \Delta t)$ contains the historical stresses from the previous time step. In Equation 2.3 it can be seen that the incremental stress consists of an elastic component and a sum of exponentially decaying viscoelastic components.

In their development of a constitutive model for polymers, Yu et al. [32] present a strain based non-linear viscoelastic model that is based on the model proposed by Xia et al. [31]. In this model, the viscoelastic strain is decomposed into a volumetric and deviatoric component. To highlight the non-linearity, the expression for the volumetric strain ϵ_v^{ve} is given in Equation 2.4 below:

$$\epsilon_v^{ve} = \frac{1}{3} \sum_{i=1}^N \int_0^t \left[1 - \exp\left(-\frac{t-\tau}{\lambda_i}\right) \right] \frac{d[gC_i(1-2\nu_i)\text{tr}(\sigma)]}{d\tau} d\tau \quad (2.4)$$

where C_i and ν_i are the compliance and the Poisson's ratio of the material relating to the i^{th} relaxation time λ_i , $\text{tr}(\sigma)$ is the trace of the stress vector and g is a function of the material state which introduces non-linearity into the viscoelastic model. In the model proposed by Yu et al. [32], g takes the following form:

$$g = 1 + d_{ve} \langle \xi \mathcal{R}(f(\sigma, \zeta, \epsilon_{eq}^p)) + (1 - \xi) f(\sigma, \zeta, \epsilon_{eq}^p) - 1 \rangle^{m_{ve}} \quad (2.5)$$

In the above equation the degree of non-linearity is prescribed by the function f , which relates to the onset of non-linear viscoelasticity and is a function of the stress level, the state of the material and the amount of plastic strain. The parameters d_{ve} and m_{ve} are material constants controlling the non-linear softening of the material. The other two parameters of importance are ξ , which changes the shape of the hysteresis loop as a result of a state transition or excessive plastic straining, and $\mathcal{R}(f)$, which is a memory function relating to permanent changes in the hysteresis loop.

2.2.3. Viscoplasticity

Apart from the motivation to include viscous and time-dependent effects provided in Section 2.2.1, the nature of plasticity further justifies the use of a viscoplasticity model for modelling the yielding behaviour of epoxy resins. The failure of a material often results in large strain rates that are the result of the onset of damage or frictional effects [7]. These large strain rates activate an internal viscous mechanism for carrying increasing loads. This phenomenon is frequently observed in engineering materials, whereby the strength of a material is proportional to the rate at which it is loaded. The main distinction between inviscid plasticity and viscoplasticity is that, in the latter model, the stress state is permitted to escape the yield surface. This piercing of the yield surface is time dependent and if the external loading remains constant, the stresses eventually relax until they reach the yield surface.

A simple elastic-viscoplastic model consists of an elastic spring in series with a Coulomb friction element and a dashpot [7], see Figure 2.12. In this model, plastic straining in the Coulomb element begins once the yield stress has been reached and any stresses that develop above the yield stress are resisted by the dashpot element.

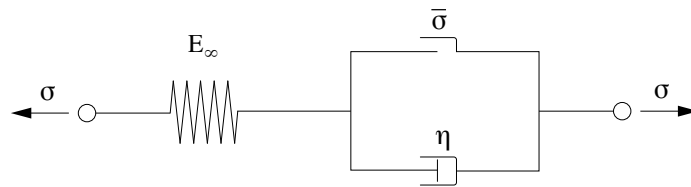


Figure 2.12: Viscoplastic rheological model.

Similar to Equation 2.1, a single order differential equation can be obtained to describe the behaviour of the simple elastic-viscoplastic model:

$$\dot{\sigma} + \frac{1}{\lambda} \sigma = E \dot{\varepsilon} + \frac{1}{\lambda} \bar{\sigma} \quad (2.6)$$

where $\lambda = \frac{\eta}{E}$ is the viscoplastic relaxation time and $\bar{\sigma}$ is the yield stress. Similar viscoelasticity, this simple model captures some of the time dependent behaviour that has been observed for polymers, such as rate-dependent yielding and the accumulation of plastic strains.

Rocha et al. [24] use a Perzyna-type formulation in their viscoplastic model for epoxy resin. Similar to traditional inviscid plasticity, the plastic strain rate in a Perzyna model is written as a function of the variation of the plastic multiplier and the plastic flow direction [7]. The departure from inviscid plasticity into time dependent behaviour occurs in the evolution of the plastic multiplier, which becomes a function of the time increment. The subsequent relaxation of the Kuhn-Tucker conditions on the yield function allows stresses to develop outside the yield surface.

2.2.4. Continuum Damage Mechanics

While viscoelastic and viscoplastic models can capture most of the complex mechanical behaviour associated with epoxy resins, neither model is able to describe the onset of failure that is evident in Figure 2.1a. A continuum damage model can capture behaviour relating to the onset of failure by relating the degradation of the elastic stiffness of damaging elements to a finite number of scalar or tensor-valued internal variables (Lemaitre and Chaboche 1990). An elementary damage model can be derived from a system of parallel elastic-brittle bars, shown in Figure 2.13. Defining d as the fraction of broken bars, which is a function of the strain, a total stress-strain relation is derived considering equilibrium of the system:

$$F = (1 - d)EA_0\varepsilon \quad (2.7)$$

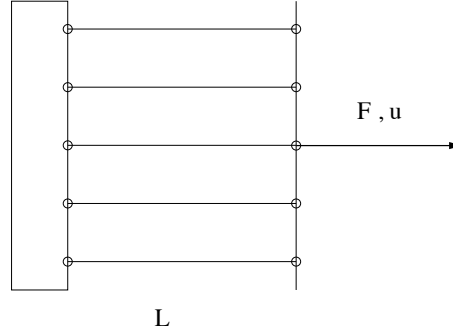


Figure 2.13: Elementary damage model.

where A_0 is the initial total cross-sectional area of the bars. This elementary damage model can be extended to an isotropic continuum through the definition of an effective stress $\tilde{\sigma}$:

$$\boldsymbol{\sigma} = (1 - d)\tilde{\boldsymbol{\sigma}} \quad (2.8)$$

where the constitutive relationship is now defined in terms of the effective stress:

$$\tilde{\boldsymbol{\sigma}} = \mathbf{D}\boldsymbol{\varepsilon} \quad (2.9)$$

The elementary bar model in Figure 2.13 can be expanded such that the bar now consists of m continuum damage elements in series, each with a linear softening behaviour. If one of these elements has a marginally lower tensile strength, the damage will be localised within this one element. De Borst et al. [7] explain that the slope of the response in the post peak regime is given by:

$$\frac{\dot{\varepsilon}}{\dot{\sigma}} = \frac{1}{E} - \frac{n}{mE} \quad (2.10)$$

where n is the ratio between the ultimate strain and the strain at damage initiation. However, an issue associated with this model and the effective stress model is that the formulation suffers from severe mesh dependency in the post peak regime. In the case of the simple bar model, global snapback occurs when $m = n$. One approach that remedies this mesh dependency issue is a fracture energy based approach in conjunction with a crack band model. A fracture energy approach considers the area under the stress-displacement curve for a continuum damage element to be a material constant related to the fracture energy of the material, G^* [7]. The crack band model regularises the dissipated energy over a defined bandwidth and, in combination with the fracture energy based approach, results in a mesh independent reformulation of Equation 2.10:

$$\frac{\dot{\varepsilon}}{\dot{\sigma}} = \frac{1}{E} - \frac{2G^*}{L\sigma_d^2} \quad (2.11)$$

where L is the length of the bar and σ_d is the stress at the onset of damage. This equation can be used to derive an expression for the minimum fracture energy that prevents global snapback, ensuring $-\dot{\varepsilon} / \dot{\sigma} \geq 0$:

$$G_{\min}^* \geq \frac{L\sigma_d^2}{2E} \quad (2.12)$$

In the definition of the damaged constitutive relationship in Equation 2.9, it is possible to either keep a constant Poisson's ratio or apply degradation to the Poisson's ratio. The damage model used by Rocha et al. [24] does not degrade the Poisson's ratio because of its loss of explicitness in viscoelasticity models. However, a spurious hardening response has been observed in damage formulations where the Poisson's ratio is not degraded. This is because constraint is provided to softening

elements by elastically unloading elements [2]. To counter this issue, Melro et al. [17] implement a compliance matrix in which both the elastic stiffness and the Poisson's ratio are degraded by the same amount:

$$\mathbf{C} = \begin{bmatrix} \frac{1}{E(1-d)} & -\frac{\nu}{E} & -\frac{\nu}{E} & 0 & 0 & 0 \\ -\frac{\nu}{E} & \frac{1}{E(1-d)} & -\frac{\nu}{E} & 0 & 0 & 0 \\ -\frac{\nu}{E} & -\frac{\nu}{E} & \frac{1}{E(1-d)} & 0 & 0 & 0 \\ 0 & 0 & 0 & \frac{1}{G(1-d)} & 0 & 0 \\ 0 & 0 & 0 & 0 & \frac{1}{G(1-d)} & 0 \\ 0 & 0 & 0 & 0 & 0 & \frac{1}{G(1-d)} \end{bmatrix} \quad (2.13)$$

where \mathbf{C} is the compliance matrix. By maintaining a constant ratio between the Poisson's ratio and the elastic stiffness, both parameters are proportionally degraded and the spurious hardening is prevented.

2.2.5. Glass Transition Behaviour

As outlined in Section 2.2.1, the mechanical behaviour of the epoxy resin depends heavily on its state. In Section 2.1.2, the temperature and moisture content are identified as the key parameters relating to state of the epoxy resin.

Yu et al. [32] propose that a single internal state variable relating to the degree of glass transition ζ can describe the material state of an epoxy resin. In their model, $\zeta = 0$ corresponds to a glassy state and $\zeta = 1$ corresponds to a rubbery state, with intermediate values representing the transition between these two states. In their work, Yu et al. only consider the transition from a glassy state to a rubbery one, even though the glass transitional process is bidirectional, ensuring that the process is energy dissipative and that $\dot{\zeta} \geq 0$.

Yu et al. define the glass transition surface, which is similar to a yield surface, as the difference between the thermodynamic driving force of ζ , π_{tr} , and a positive constant, π_c :

$$\Phi_{tr} = \pi_{tr} - \pi_c \quad (2.14)$$

In the above equation, π_{tr} is a function of both the temperature and moisture content of the epoxy resin. At a specific combination of temperature and moisture content, π_{tr} pierces the glass transition surface and the degree of glass transition ζ is accordingly updated to satisfy $\Phi_{tr} \leq 0$.

2.3. Modelling the Transport Behaviour of Epoxy

In order to better represent the hygrothermal ageing of glass/epoxy composites, thermal and moisture effects should be considered. In this section, numerical models describing these two transport phenomena are described.

2.3.1. Thermal Conduction

The most commonly used model to represent thermal behaviour is Fourier's law of heat conduction, which states that for a given direction, heat flux is proportional to the negative gradient of the temperature [6]:

$$\mathbf{q} = -\boldsymbol{\kappa} \nabla T \quad (2.15)$$

where \mathbf{q} is the heat flux vector, $\boldsymbol{\kappa}$ is the thermal conductivity matrix and ∇T is the temperature gradient vector. This relationship has been successfully applied to study thermal conduction in epoxy resins [8, 32]. In a general sense, the thermal conductivity matrix can be anisotropic and have a non-linear dependence on temperature. Further, it has also been observed that heat transfer

is dependent on the moisture level within the epoxy [4, 32]. Therefore, the thermal conductivity matrix should formally be expressed as $\boldsymbol{\kappa}(T, \omega)$.

The flow of heat resulting from heat flux generates a time rate of change of stored energy, which is related to the specific heat of the material c [6]:

$$\Delta Q = \rho c V \Delta T \quad (2.16)$$

where ΔQ is the change in internal energy, ρV is the mass of the element in question and ΔT is the change in temperature of the element.

In order to model the heat exchange between a specimen and its surrounding fluid, a convective relationship is established [6]. The heat transfer into a body across a fluid boundary is related to the heat transfer coefficient h . This coefficient is a function of the nature of the fluid and the dynamics of fluid motion past the surface, and is described by:

$$\mathbf{q} \cdot \mathbf{n} = -h(T - T_f) \quad (2.17)$$

where $\mathbf{q} \cdot \mathbf{n}$ is the flux vector normal to the fluid boundary, T is the temperature of the specimen at the boundary and T_f is the temperature of the fluid.

2.3.2. Moisture Diffusion

The diffusion of moisture within a material can be modelled with Fick's first law of diffusion, which is analogous to Fourier's law of heat conduction:

$$\mathbf{j} = -\mathbf{D}_\omega \nabla \omega \quad (2.18)$$

where \mathbf{j} is the water flux vector, \mathbf{D}_ω is the diffusivity matrix and $\nabla \omega$ is the concentration gradient vector. As is the case for thermal conduction, the diffusivity matrix can be anisotropic, non-linear and depend on the temperature of the epoxy resin. As a result, the diffusivity matrix should formally be expressed as $\mathbf{D}_\omega(T, \omega)$.

Fickian diffusion behaviour relates to the take up of water within the free space between the molecular chains [32] and was observed for the epoxy resin system studied in this thesis during experiments at room temperature [22]. However, it is possible that at elevated temperatures, the resin system may exhibit two phase behaviour, whereby water molecules also become bound to the molecular chains of the epoxy through chemical reaction. In such cases, a Langmuir type diffusion model can be used, which extends Fickian diffusion behaviour by decomposing the moisture content into the free moisture concentration and the bound moisture concentration [32]. A description of the evolution of bound water can be written as follows:

$$\dot{\omega}_b = \Lambda_f \omega_f - \Lambda_b \omega_b \quad (2.19)$$

where ω_b and ω_f are the bound and free moisture concentrations respectively, and Λ_b and Λ_f are the chemical moduli related to bound and free moisture concentrations respectively. These chemical moduli control the evolution of the bound moisture.

2.4. Multiphysics Modelling

Multiphysics modelling involves simultaneously simulating multiple physical processes on the same domain in order to investigate the effect of complex physical interactions. In its most generic form, coupling between the physical models occurs through either the bulk domain or an idealised interface [14]. The chosen solution technique for multiphysics modelling must consider the interactions between various the physical models relevant for the given problem. Two such techniques are the operator split approach or the assumption of strong coupling. In the operator split approach,

strong couplings between components are ignored. Each physical problem is solved separately and the analysis proceeds in an uncoupled, sequential manner. On the other hand, strong coupling approaches modify and combine each physical problem into a single formulation in an attempt to solve all physical fields in a single iterative method. However, the strong coupling approach often involves a significantly higher computational cost [14].

The operator split method has been successfully applied to the thermo-mechanical analysis of heterogeneous solids [20] and the diffusion-mechanical analysis of laminated composites [23]. In both applications, the transport problem was solved first, with the resulting field used as input for the solution of the mechanical problem. Özdemir et al. [20] note that the resulting numerical scheme is efficient but only conditionally stable. However, it is noted that if an incremental iterative scheme is already required for the mechanical analysis, the time step needed to capture the material non-linearities is often more taxing than that required for the stability of the multiphysics analysis.

2.5. Existing Numerical Frameworks

This thesis builds upon the numerical work by Rocha et al. [23, 24] with the aim of improving their epoxy resin model for describing the hygrothermal ageing of laminated composites. The constitutive model for polymers formulated by Yu et al. [32] is referenced as a starting point for the development of improvements to the framework by Rocha et al. This section briefly describes both formulations and assesses the suitability and applicability of each model.

2.5.1. Overview of the Yu Model

In their paper 'A hygro-thermo-mechanical coupled cyclic constitutive model for polymers with considering glass transition' [32], Yu et al. describe a thermodynamically consistent mathematical model founded in experimental observations. The mechanical model incorporates viscoelasticity and viscoplasticity and is coupled to equations describing Fourier heat conduction and non-Fickian diffusion. A criterion for the glass transition of a polymer is developed and coupled to the mechanical equations.

Yu et al. perform experiments on simple polymer specimens for calibration and verification of their model. It is reported that the constitutive model can reasonably predict the temperature, relative humidity, and rate dependent cyclic deformations of polymer specimens and can also model the deformation induced temperature gain observed in cyclic tests.

However, in their implementation of the coupled multi-field equations, Yu et al. simplify the domain and the model formulation so that the material is described by only one representative point, see Figure 2.14. As a consequence, the resulting temperature, moisture and stress fields are uniform and the application of the constitutive model is limited to prismatic one dimensional domains.

2.5.2. Overview of the Rocha Framework

The numerical framework developed by Rocha et al. [23, 24] employs both multiscale and multiphysics modelling in order to couple macroscale diffusion behaviour and mechanical stresses with the microscale behaviour of laminated composites. Figure 2.15 summarises the relationship between the various models in this numerical framework.

2.5.2.1. Macroscale Model

A coupled multiphysics model is implemented at the macroscale involving moisture diffusion and mechanical stress. The diffusion analysis uses a Fickian model to simulate the moisture concentration field within the domain. The mechanical model uses a small strain assumption, with the material stiffness inferred from the behaviour of a micromodel at every integration point. Swelling strains and hygroscopic degradation of the mechanical properties are dependent upon the moisture concentration level obtained in the diffusion analysis. The diffusion analysis is not effected by

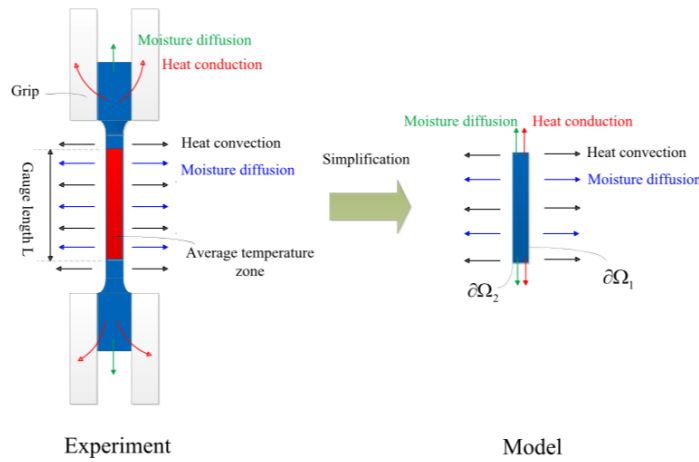


Figure 2.14: Domain simplification used in the implementation by Yu et al. [32].

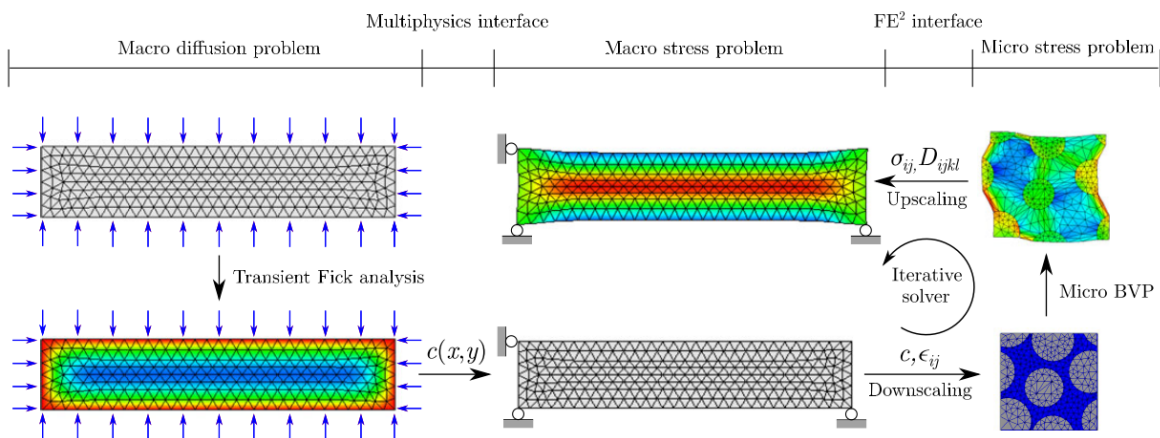


Figure 2.15: Schematic representation of the multiphysics/multiscale model for hygrothermal ageing [23].

the stress state of the material and, as a result, the operator split approach is utilised. In this multiphysics model, the macroscale diffusion problem is solved first, followed by the multiscale stress problem.

2.5.2.2. Microscale Model

The microscale model considers a representative volume element (RVE) consisting of unidirectional glass fibres embedded in an epoxy resin matrix. Interface elements are employed around each glass fibre to capture fibre-matrix debonding. The glass fibres are modelled as a linear-elastic material and failure of the fibres is not considered. The interface elements between the glass fibres and the epoxy resin matrix incorporate a cohesive zone damage model, in which the onset of damage is accompanied by jumps in the displacement field.

Most relevant to this thesis, however, is that Rocha et al. simulate the mechanical behaviour of the epoxy resin matrix with a viscoelastic-viscoplastic-damage (VE-VP-D) model that builds on the work of Melro et al. [17]. Figure 2.16 schematically describes the VE-VP-D model using rheological elements. The elastic response consists of a stiffness that represents the long term response of the material E_∞ and a parallel chain of n Maxwell elements that model the viscoelastic response of the material. These two elements correspond to a Maxwell chain model highlighted in Section 2.2.2. The viscoplastic component combines a dashpot element in parallel with a Coulomb friction

element, as described in Section 2.2.3, and allows stresses greater than the yield stress to develop. Damage is incorporated into the rheological model by defining an effective stress $\tilde{\sigma}$ and is further described in Section 3.1.

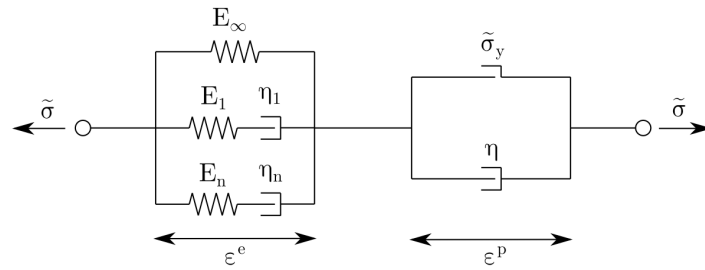


Figure 2.16: Schematic representation of the VE-VP-D model for epoxy resins [24].

Moisture dependent degradation is incorporated into the epoxy resin and the interface models by applying a single degradation factor d_ω to the relevant material properties:

$$d_\omega = \frac{d_\omega^\infty}{\omega_\infty} \omega \quad (2.20)$$

where ω_∞ is the moisture concentration at saturation and d_ω^∞ is the experimentally obtained material degradation factor at saturation. For example, an increase in moisture concentration results in the degradation of the elastic stiffness and tensile strength in the following manner:

$$E^\omega = (1 - d_\omega)E \quad (2.21a)$$

$$\sigma_t^\omega = (1 - d_\omega)\sigma_t \quad (2.21b)$$

2.5.2.3. Assessment of the Epoxy Model

The model formulated by Rocha et al. reasonably predicts both strain-rate and moisture concentration dependent behaviour for monotonic tests [24]. A significant drawback of the model is that it does not account for the temperature dependence of the mechanical properties highlighted in Figure 2.7. As a consequence, the significant phenomenon of glass transition is not captured by the numerical framework. In addition to this, the viscous mechanical models do not successfully describe the behaviour of the epoxy resin at relatively large strains. Figure 2.17 presents a comparison of an experimental loading-unloading-reloading test against the behaviour as predicted by the calibrated numerical model.

The only way for the linear VE-VP model to capture the non-linearity that is present above stresses of approximately 50 MPa in Figure 2.17a is through the activation of plasticity. As a result, softening of the response above this stress in Figure 2.17b is accompanied with accumulated plastic strain. However, this accumulation of strain is not present in the experimental response. Further, once the stress in Figure 2.17a is above approximately 70 MPa, significant plastic straining occurs. This means that, in the region between 50 and 70 MPa, the softening of the response is not related to plasticity. Thus, the linear viscoelastic model is not able to capture the non-linear elastic behaviour exhibited by the epoxy resin.

It was noted by Rocha et al. that the damage formulation used in the epoxy model had not been subject to mesh dependency tests when the damage model was combined with viscoelasticity and viscoplasticity. Further, many authors [7, 11] have noted that viscous models can play a regularising role when combined with damage models. As a result, issues relating to the mesh dependency of the damage model used in the epoxy model formulation are investigated further in Chapter 3.

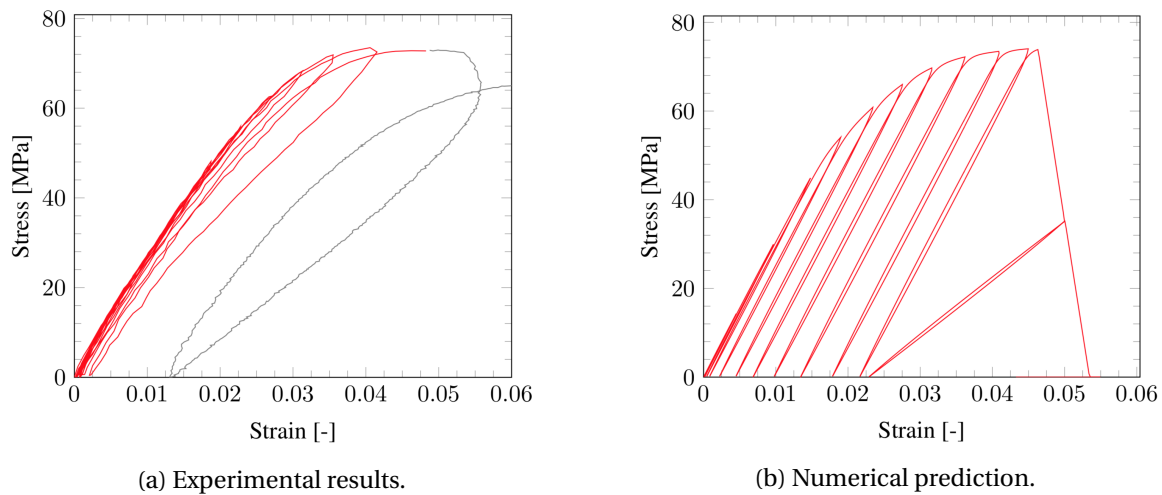


Figure 2.17: Comparison of experimental results and numerical simulation for a loading-unloading-reloading test [24].

2.6. Experimental Procedures

Two types of experiments were performed in this thesis, namely a Dynamic Mechanical Analysis (DMA) and a creep test. This section briefly describes the theoretical background relating to each test.

2.6.1. Dynamic Mechanical Analysis

DMA is an experimental technique that is used to measure the behaviour of a material primarily when subject to variations in stress, temperature and frequency [19, 21]. In a DMA test, a sinusoidal deformation is applied to a small specimen and the resulting load and displacement is recorded. The magnitude of the displacement is related to the material stiffness, while the phase shift between the load and displacement signals relates to energy dissipation. Typically the test is performed at a number of different loading frequencies and with a constantly varying temperature meaning that the dependence on these parameters can be investigated.

From the raw load displacement data, the DMA post-processing tool calculates the terms to related material stiffness and damping. The most frequently interpreted parameters from a DMA test are the storage modulus E' , the loss modulus E'' and the loss factor $\tan \delta$. The storage modulus is defined as the ratio between the in-phase stress to the strain [25] and represents the elastic portion of the material response. On the other hand, the loss modulus is defined as the ratio between the out-of-phase stress to the strain [25] and represents the viscous portion of the material response. The loss factor is the ratio between the loss and storage moduli, providing a measure for the amount of dampening in the material. The storage and loss moduli can also be expressed as a function of the loading frequency ω_1 and the linear viscoelastic parameters. The following equations summarise each of the DMA parameters:

$$E' = E_\infty + \sum_i^N \frac{E_i \omega_1^2}{\lambda_i^{-2} + \omega_1^2} \quad (2.22a)$$

$$E'' = \sum_i^N \frac{E_i \omega_1}{\lambda_i^{-2} + \omega_1^2} \quad (2.22b)$$

$$\tan \delta = \frac{E''}{E'} \quad (2.22c)$$

where E_∞ is the long term elastic modulus, E_i are the viscoelastic stiffnesses and λ_i are the corresponding relaxation times. It is clear from the above expressions that the storage modulus is related to the elastic stiffness due to the inclusion of the E_∞ term, while the loss modulus depends only on viscous effects.

As a result, the DMA test can be useful for identifying temperature related changes in elastic stiffness, from which the glass transition temperature can be inferred. Further, if performed at multiple frequencies, it is possible to use the results to calibrate a linear viscoelasticity model through the utilisation of Equations 2.22a and 2.22b.

2.6.2. Creep Test

A creep test involves recording the time dependent strain resulting from a constant applied stress [25]. As the elastic response of epoxy resins consists of viscoelastic stresses, the creep test is used to allow these viscoelastic stresses to relax over a significant duration of time in order to isolate the long term elastic modulus of the epoxy resin. For a three point bending test, the elastic modulus can be determined by assuming that the sample behaves in a linear manner. According to Euler-Bernoulli beam theory, the deflection of the sample is directly proportional to the applied load and elastic modulus. This deflection can be calculated from the following expression:

$$u = \frac{FL^3}{48EI} \quad (2.23)$$

where u is the bending deflection at the point of load application (mid-span), F is the magnitude of the force, L is the free bending length and I is the second moment of inertia about the axis of bending. Further, to ensure the material response remains linear, the maximum fibre stress should remain a relatively safe distance below the yield stress and the deformation should be limited, such that second order geometrical effects do not become significant. From Euler-Bernoulli beam theory, the maximum fibre stress can be calculated by:

$$\sigma = \frac{M}{W} \quad (2.24)$$

where M is the bending moment resulting from the applied load and W is the elastic section modulus related to the cross-section of the specimen. As a result, a creep test can be used to calibrate the long term elastic moduli of an epoxy resin specimen at multiple temperatures.

2.7. Conclusions

The important findings from this literature review can be summarised as follows. The mechanical behaviour of epoxy resins is highly time dependent and exhibits the following features: strain rate dependency, ratcheting, stress relaxation, hysteresis and non-linear elasticity. An increase in the temperature and moisture concentration of an epoxy resin results in a degradation of its stiffness and strength. Further, an increase in the moisture concentration acts to reduce the glass transition temperature of the epoxy resin. The moisture content of an epoxy resin has an insignificant effect on thermal conduction behaviour however, the temperature of an epoxy resin can have a significant impact on diffusivity.

The mechanical behaviour of epoxy resins can be modelled through a combination of viscoelastic, viscoplastic and damage models. An epoxy resin can be described by three material states: a glassy state at lower temperatures, a rubbery state at higher temperatures and a mixed glassy-rubbery state during the process of glass transition. Further, the thermal conduction behaviour of an epoxy resin can be modelled using Fourier's law of heat conduction. The diffusion behaviour can be modelled using Fick's law of diffusion, however, this may not be valid at elevated temperatures. An uncoupled multiphysics framework can be used to combine the aforementioned physical models in order to describe the complex hygrothermal behaviour of epoxy resin.

The constitutive model developed by Yu et al. [32] successfully combines glass transition behaviour with mechanical behaviour for polymer materials. However, the implementation of the framework contains simplifications that restrict its applicability. The numerical framework developed by Rocha et al. [23, 24] captures many of the mechanical aspects exhibited by epoxy resins. However, thermal dependency and non-linear viscoelasticity is not included in the formulation.

Finally, the DMA and creep test can be performed to investigate the temperature dependent mechanical behaviour of epoxy resin and can also be used for model calibration.

3

Regularisation of the Damage Model

In this section, a numerical study has been performed on a simple problem to investigate the mesh dependency of the damage model used by Rocha et al. [24] and to examine the regularising effects provided by the viscous components of the model.

3.1. Overview of the Damage Model

The damage model employed by Rocha et al. [24] is a linearly softening continuum damage model, in which stress is a function of a single damage variable d :

$$\boldsymbol{\sigma} = (1 - d)\tilde{\boldsymbol{\sigma}} \quad (3.1)$$

where $\tilde{\boldsymbol{\sigma}}$ is the effective stress. The fracture surface is pressure dependent and shrinks as the material dissipates energy. This allows the damage model to capture quasi-static damage initiation and also low-cycle fatigue failure, which initiates at a lower stress level. The fracture surface is described by:

$$f_d(\tilde{\boldsymbol{\sigma}}, r) = \frac{3\tilde{J}_2}{X_c(\Xi)X_t(\Xi)} + \frac{\tilde{I}_1(X_c(\Xi) - X_t(\Xi))}{X_c(\Xi)X_t(\Xi)} - r \quad (3.2)$$

where the fracture strengths X_c and X_t are functions of the material dissipation Ξ and r is an internal variable relating to the size of the fracture surface.

The linear softening law employs a characteristic length, taken from Bažant's crack model (Bažant et al., 1983) in an attempt to regularise the effect that mesh refinement has on damage evolution:

$$d = \begin{cases} \frac{\tilde{\sigma}_f(\tilde{\sigma}_{\text{eq}} - \tilde{\sigma}_d)}{\tilde{\sigma}_{\text{eq}}(\tilde{\sigma}_f - \tilde{\sigma}_d)} & \tilde{\sigma}_{\text{eq}} \leq \tilde{\sigma}_f \\ 1 & \tilde{\sigma}_{\text{eq}} > \tilde{\sigma}_f \end{cases} \quad (3.3)$$

where $\tilde{\sigma}_d = X_t$ is the uniaxial tensile strength, $\tilde{\sigma}_{\text{eq}}$ is an equivalent stress measure that is derived from a uniaxial stress state and $\tilde{\sigma}_f$ is the regularised effective stress at complete failure given by:

$$\tilde{\sigma}_f = \frac{2G^*E}{l_e X_t} \quad (3.4)$$

where G^* is related to the material fracture energy and l_e is the finite element characteristic length according to Bažant's crack band model. While there is no direct coupling between plasticity and damage evolution in the damage formulation, plasticity is still permitted to evolve after the initiation of damage.

It should also be noted that the Poisson's ratio does not enter this formulation and therefore remains undamaged in this model. This is in contrast to the formulation by Melro et al. [17], in which both the elastic stiffness and the Poisson's ratio are degraded by the same amount, see Section 2.2.4. The motivation behind not including the Poisson's ratio in the VE-VP-D model is that the relationship between the bulk and shear moduli loses explicitness when viscoelasticity models are used [16, 24].

3.2. Mesh Dependency Study

3.2.1. Overview of the Analysis

In order to study the mesh dependency of the damage model, a number of numerical tests were conducted on the VE-VP-D model. It was hypothesised that the viscous models might introduce regularising effects. This hypothesis challenges the need for additional regularising models, such as Bažant's crack band model. The numerical study was conducted on three-dimensional continuum elements. Two separate geometries were modelled and a tensile force was applied through displacement control, see Figure 3.1.

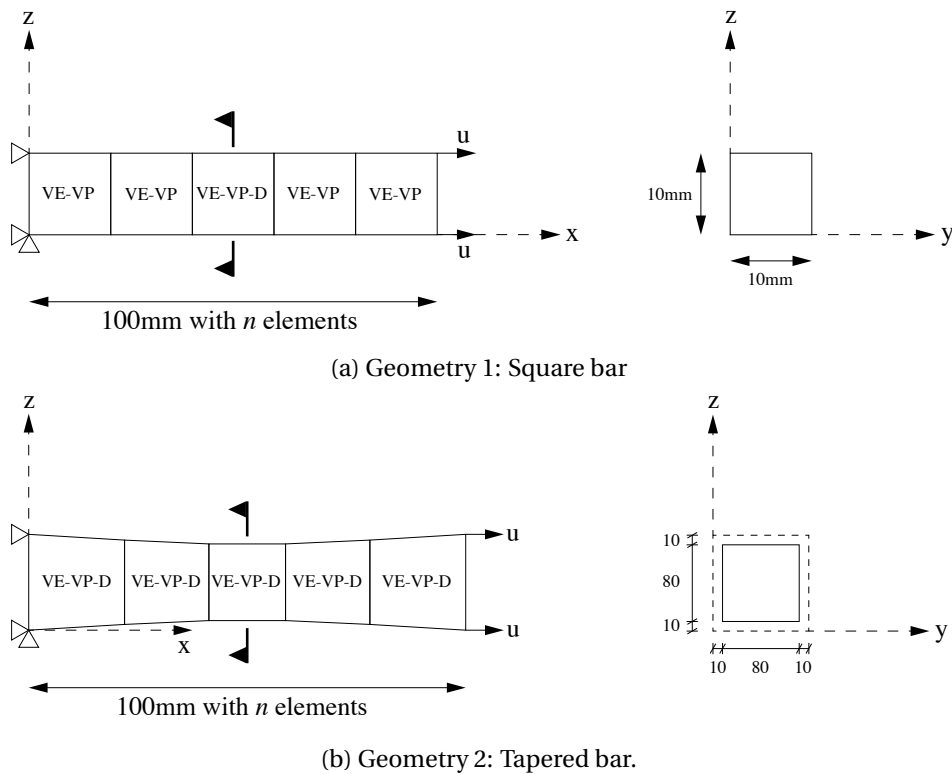


Figure 3.1: Response of the square geometry with the original damage model.

The transverse geometry of the bar was modelled with a single element. Mesh refinement involved the subdivision of the bar in the longitudinal direction only. In the first geometry, a square bar was studied in which only the central element incorporated the VE-VP-D model. The remaining elements were assigned the VE-VP model, thus enforcing damage localisation within a single element. In the second geometry, a tapered square bar was modelled with the VE-VP-D model assigned to all elements. This enforced damage initiation in the central element. However, the localisation of damage in this second geometry was not limited to a single element.

The material properties chosen for the analysis are summarised in Table 3.1 below and represent typical properties for an epoxy resin.

Model	Material Properties
	$E_\infty = 2900 \text{ MPa}; \nu_\infty = 0.35$
Viscoelasticity	$K_i = [472 \text{ MPa}, 242 \text{ MPa}, 111 \text{ MPa}]; \lambda_{i,k} = [0.007 \text{ s}, 0.126 \text{ s}, 0.216 \text{ s}]$ $G_i = [158 \text{ MPa}, 80 \text{ MPa}, 37 \text{ MPa}]; \lambda_{i,g} = [0.021 \text{ s}, 0.378 \text{ s}, 0.648 \text{ s}]$
Viscoplasticity	$\sigma_t = -14.859 \exp(-\varepsilon_{\text{eq}}^p/0.0012) - 34.1296 \exp(-\varepsilon_{\text{eq}}^p/0.0057) + 71.3997 \text{ MPa}$ $\sigma_c = -24.1071 \exp(-\varepsilon_{\text{eq}}^p/0.0097) - 10.4262 \exp(-\varepsilon_{\text{eq}}^p/0.0016) + 89.2022 \text{ MPa}$ $\nu_p = 0.5; \eta_p = 205 \times 10^3 \text{ MPa} \cdot \text{s}; m_p = 1.5$
Damage	$X_t = 100 - 0.5 \exp(\varepsilon_{\text{eq}}^p/0.003) \text{ MPa}$ $X_c = 120 - 0.5 \exp(\varepsilon_{\text{eq}}^p/0.003) \text{ MPa}$ $G^* = 300 \text{ N/mm}$

Table 3.1: Material properties used in the mesh dependency analysis.

Note that the value of the fracture energy G^* was chosen such that global snapback behaviour was avoided, while still resulting in a relatively brittle response. The minimum fracture energy for a bar in tension can be calculated from Equation 2.12:

$$G_{\min}^* = \frac{100 \text{ mm} \times (100 \text{ MPa})^2}{2 \times 2900 \text{ MPa}} = 172.4 \text{ N/mm} \quad (3.5)$$

which is smaller than the chosen value of $G^* = 300 \text{ N/mm}$. For each numerical analysis, the behaviour of the bar in tension was studied with seven different levels of mesh refinement. The number of Hex-8 elements subdividing the longitudinal domain was chosen to be 1, 3, 5, 11, 21, 51 and 101 elements.

In order to validate the numerical results, the analytical load and displacement at damage initiation, and the displacement at failure are evaluated in Box 3.2.1.

Box 3.2.1: Verification of the Numerical Damage Results

The force at the onset of damage for the square geometry $F_{d,s}$ can be determined from the fracture strength:

$$F_{d,s} = \sigma_d A = 100 \text{ MPa} \times 100 \text{ mm}^2 = 10 \times 10^3 \text{ N} \quad (3.6)$$

The force at the onset of damage for the tapered geometry $F_{d,t}$ can similarly be determined from the fracture strength:

$$F_{d,t} = \sigma_d A = 100 \text{ MPa} \times 64 \text{ mm}^2 = 6.4 \times 10^3 \text{ N} \quad (3.7)$$

The displacement at damage initiation for the square geometry $u_{d,s}$ follows from the elastic modulus:

$$u_{d,s} = \frac{\sigma_d L}{E} = \frac{100 \text{ MPa} \times 100 \text{ mm}}{2900 \text{ MPa}} = 3.45 \text{ mm} \quad (3.8)$$

The displacement at failure for the square geometry $u_{f,s}$ can be determined by integrating the stress-displacement curve and equating it with the fracture energy of the material. Assuming a bilinear response:

$$G^* = \int \sigma(t) du \approx \frac{\sigma_d u_{f,s}}{2} \quad (3.9)$$

$$\therefore u_{f,s} = \frac{2G^*}{\sigma_d} = \frac{2 \times 300 \text{ N/mm}}{100 \text{ MPa}} = 6 \text{ mm} \quad (3.10)$$

The displacement at failure for the tapered geometry $u_{f,t}$ is identical to that of the square geometry because the fracture energy and the fracture strength are unchanged.

$$\therefore u_{f,t} = 6 \text{ mm} \quad (3.11)$$

3.2.2. Study 1: Original Damage Model

The first numerical study utilised the damage model described in Section 3.1 with both viscous models and the crack band model activated. The mesh dependency results for the square geometry with the original damage model are summarised in Figure 3.2.

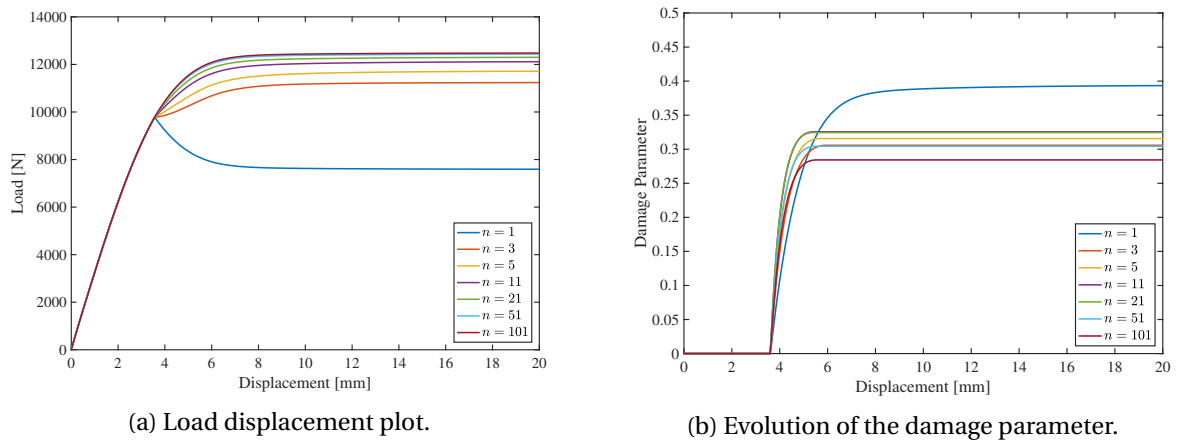


Figure 3.2: Response of the square geometry with the original damage model.

Both Figures 3.2a and 3.2b indicate that damage initiation occurred at the same displacement of 3.60 mm and at a load of just under 10 kN. This result coincides closely with the analytical predictions presented in Box 3.2.1. However, Figure 3.2a shows that the original damage model exhibited a mesh dependent response. This is because, as more elements were added to the model, the maximum load resisted by the geometry increased. Further, there was a convergence towards a plateau of 12 kN when more than 21 elements were used to discretise the geometry. Figure 3.2b highlights that the damage parameter plateaued at a value between 0.25 and 0.40, depending on the number of elements. The deformation after this plateau largely resulted in plastic strains within the damaged and adjacent elements. As a result, viscoplasticity in the original damage model dominated the behaviour after damage initiation.

The intention of the damage model described in Section 3.1 is to impose linear softening of the material after the damage initiates. It is apparent from Figure 3.2 that this behaviour is not achieved, even for the simple case of a square bar loaded in tension. In order to attempt to rectify this discrepancy between the intent of the damage formulation and the observed response, it was proposed that the evolution of plasticity be prevented after the initiation of damage. This separation of the models is, in essence, a practical consideration, restricting the viscoplastic model to describe plasticity before damage and allowing the damage model to capture all behaviour after damage initiation.

3.2.3. Study 2: No Plasticity After Damage

The second numerical study modified the original damage model by disabling viscoplasticity at all integration points where damage had been initiated. This modification was introduced to prevent plasticity from dominating the response of the model after damage initiation. The results from the numerical analysis for the square geometry are summarised in Figure 3.3, while the results for the tapered geometry are summarised in Figure 3.4.

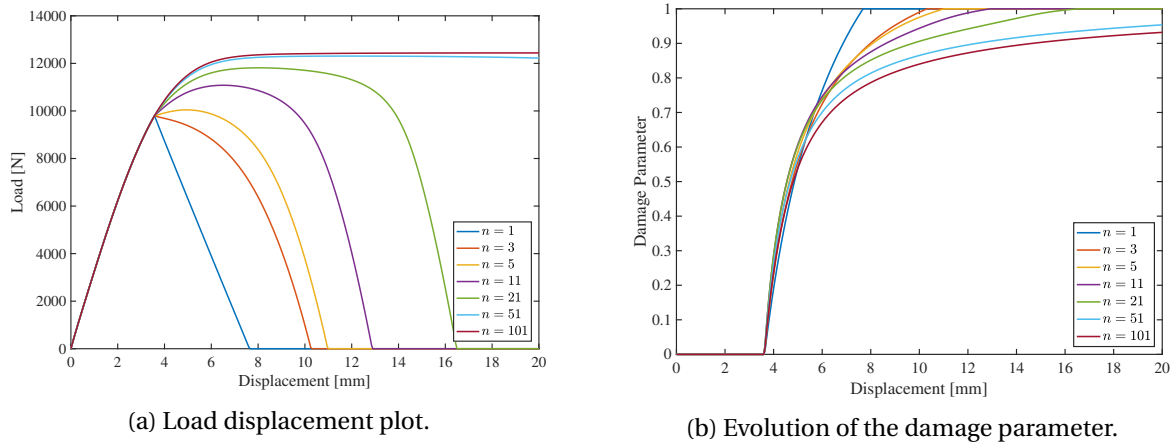


Figure 3.3: Response of the square geometry with the modified damage model.

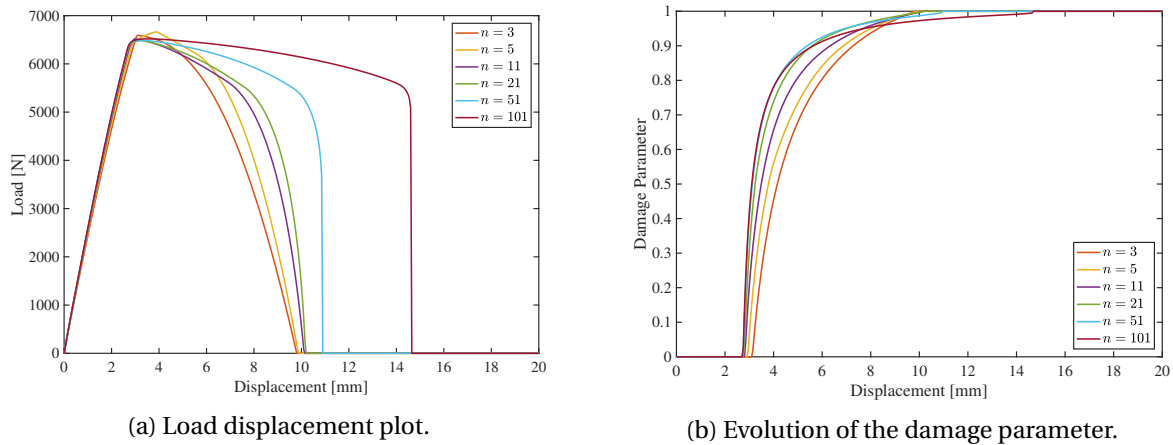


Figure 3.4: Response of the tapered geometry with the modified damage model.

Both Figures 3.3 and 3.4 show that preventing plasticity after damage initiation allowed damage to fully develop in the bar specimens with all test cases experiencing fracture (note that for $n = 51$ and $n = 101$ in Figure 3.3, fracture occurred at a displacement greater than 20 mm and is therefore not visible in the figure). The load-displacement results still show a significant mesh dependency. For the square geometry, increasing the number of elements resulted in a hardening of the response after damage initiation, leading to an increase in the peak load for $n > 3$ elements and a significant increase in the fracture strain for all mesh subdivisions. Conversely, the peak load obtained for the tapered geometry, approximately 6.5 kN, was relatively mesh independent and matched the load derived in Box 3.2.1. However, after damage initiation, the tapered geometry also suffered from mesh dependency, with a greater number of elements resulting in a larger fracture strain.

An explanation for this mesh dependent behaviour can be drawn from examining the deformation of the damaging elements. During the localisation of damage, the elements adjacent to the

damaging elements experience unloading. These unloading elements undergo less lateral contraction than the damaging elements would if they were to stay in a uniaxial stress state. This is because the Poisson's ratio remains constant in the current damage model formulation. Thus, the damaging elements are constrained in the lateral direction by the unloading elements, resulting in the development of a triaxial tensile stress state in the damaging elements. This behaviour is summarised by Figure 3.5, which shows the tensile stresses developing in the lateral directions. Figure 3.6 presents these transverse stresses in the central element for both the square and tapered geometry analyses.

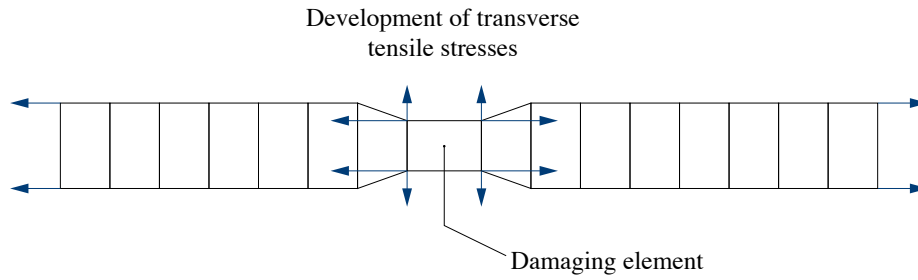


Figure 3.5: Constraint from the adjacent unloading elements causes transverse tensile stresses to develop in the damaging elements.

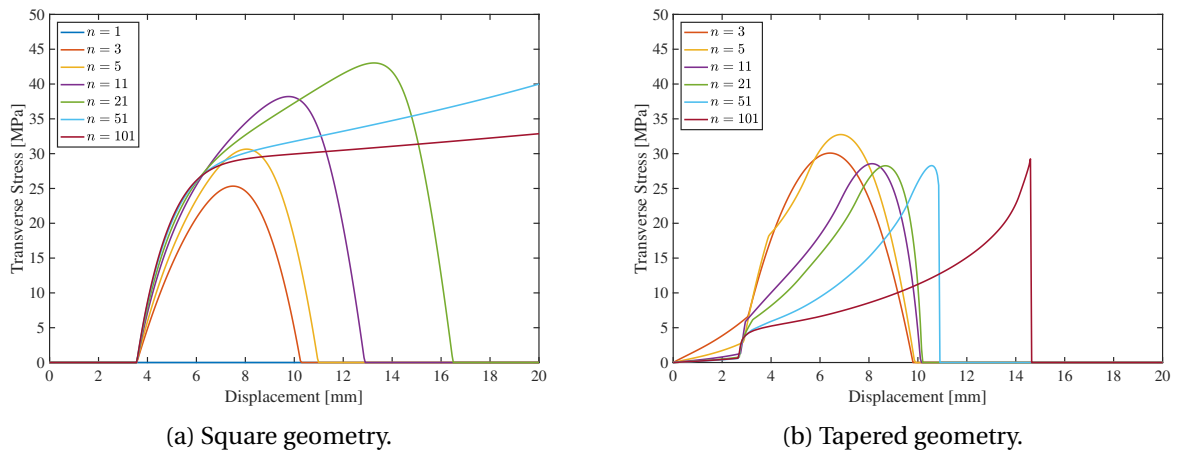


Figure 3.6: Transverse stresses in the damaged element for modified damage model.

It is apparent from Figure 3.6 that significant transverse tensile stresses develop after damage initiation. In this current damage formulation, the definition of the equivalent stress in Equation 3.2 is a function of the effective deviatoric stress invariant \tilde{J}_2 and is derived assuming a uniaxial stress state. As a result, the development of transverse tensile stress, in conjunction with the imposed longitudinal tensile stress, acts to hinder the evolution of the damage parameter. This is because a triaxial stress state significantly reduces the value of \tilde{J}_2 . It is clear from Figure 3.5 that given a non-zero and constant Poisson's ratio, the transverse stresses in the square geometry become a function of the mesh size because the aspect ratio of the damaged element has a direct effect on the equilibrating transverse stresses. As a result, the inclusion of a damaging Poisson's ratio in the damage model formulation is necessary to prevent the observed spurious hardening induced by the development of transverse tensile stresses.

3.2.4. Study 3: Zero Poisson's Ratio

In the last numerical study, the material properties were modified such that the viscoelastic and viscoplastic response did not induce any lateral contraction. This was enforced by multiplying the viscoelastic shear stiffnesses in Table 3.1 by a factor of 1.5 such that, in combination with the viscoelastic bulk stiffnesses, a zero Poisson's ratio was obtained¹. To ensure a zero Poisson's ratio for viscoelasticity, the shear relaxation times were set to be equal to the bulk relaxation times. On top of this, both ν_∞ and ν_p were set to zero.

To study the regularising effect of the crack band model and the viscous models, both models were initially switched off and the resulting load displacement diagram was obtained as a control. Each model was successively reactivated and the resulting load displacement diagrams are presented in Figure 3.7 for the square geometry and Figure 3.8 for the tapered geometry.

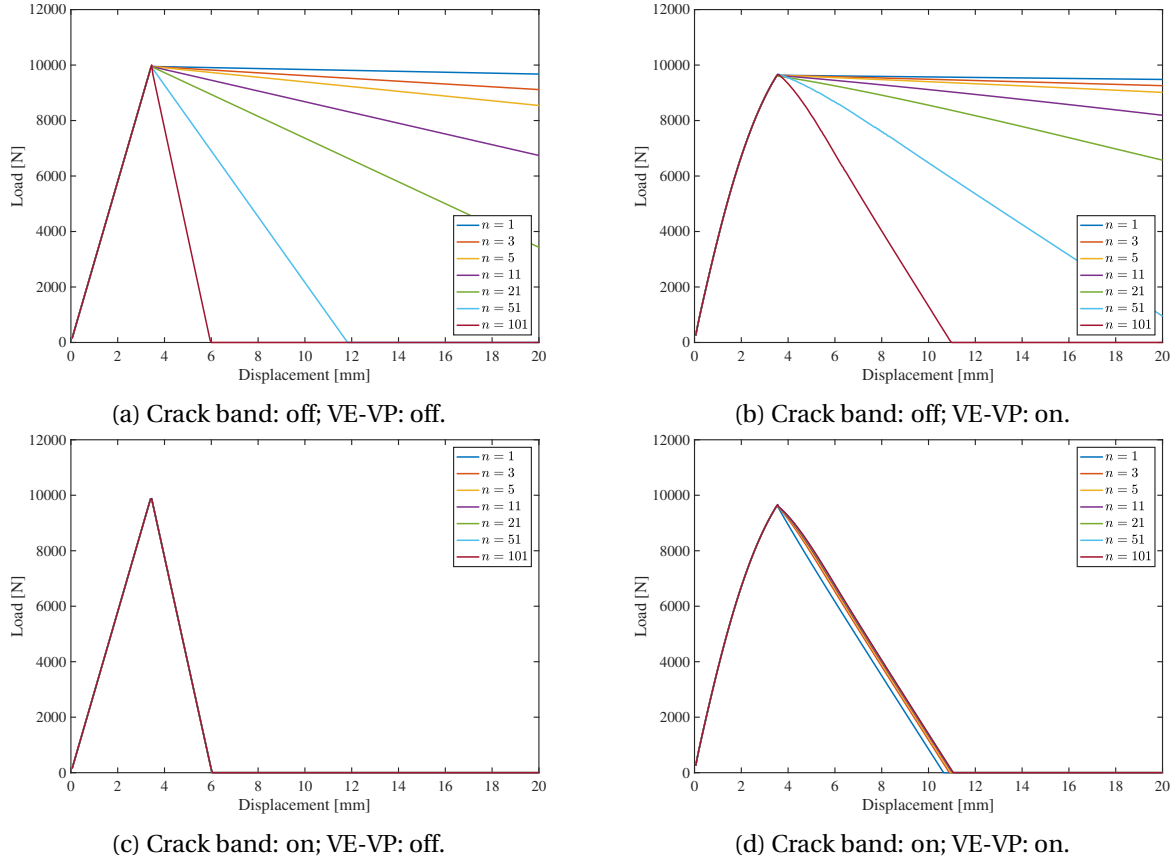


Figure 3.7: Load displacement response of the square geometry with the modified damage model and $\nu = 0$.

Figures 3.7c and 3.8c indicate that, for the geometries studied, the crack band model adequately regularises the damage model with a zero Poisson's ratio because a mesh independent response was obtained. The slight variations in stiffness in Figure 3.8c can be attributed to the discretisation of the tapered bar, which for a larger number of subdivisions, results in a larger effective cross-sectional area, see Figure 3.1b. Further, by comparing Figures 3.7b and 3.8b to 3.7c and 3.8c, it is apparent that, in the absence of the crack band model, the viscous models are not effective at regularising the damage model.

The mesh independent results presented in Figures 3.7 and 3.8 largely correspond with the analytical results computed in Box 3.2.1. The main difference is apparent in a comparison of Figures 3.7c and 3.8c with Figures 3.7d and 3.8d, which reveals an increased fracture displacement in the

¹It holds that $\nu = \frac{3K - 2G}{2(3K + G)}$, therefore if $G = \frac{3}{2}K$, then $\nu = 0$.

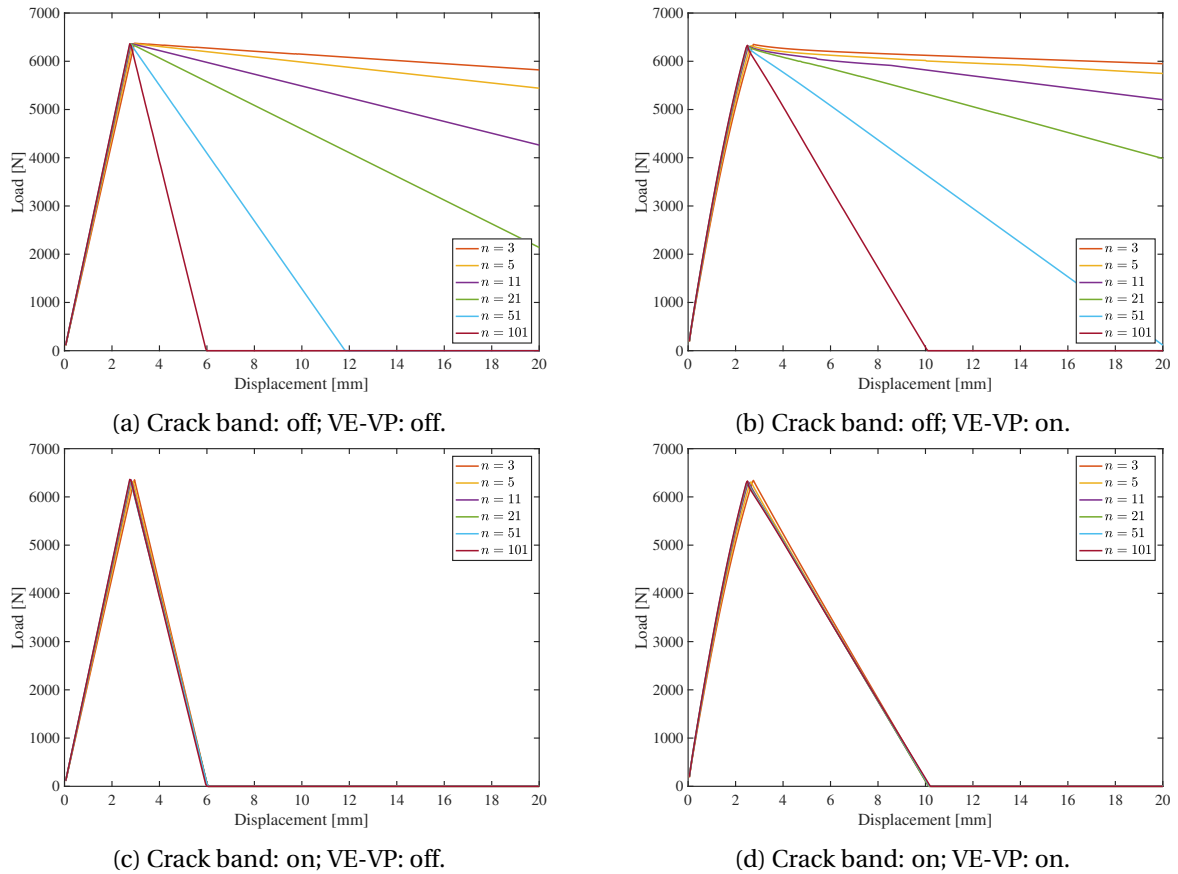


Figure 3.8: Load displacement response of the tapered geometry with the modified damage model and $\nu = 0$.

models containing viscous effects. Figure 3.9 summarises the longitudinal strains in the undamaged elements for the models with and without viscoplasticity. From this figure, it is clear that there are no residual strains in the undamaged elements when the VE-VP model is switched off and, as a result, the final displacement is effected only by the strains developed in the damaged elements. However, when the VE-VP model is active, each undamaged element has a component of viscoelastic strain, which eventually decays, and a component of unrecoverable plastic strain. As a result, these extra viscous and plastic strains cause the fracture displacement to be larger when the VE-VP model is active than when compared to the analytical prediction numerical inviscid results.

3.3. Conclusions and Recommendations

Three numerical studies were conducted on the existing VE-VP-D model to investigate the mesh dependency of the damage formulation. A modified model was adopted, in which the development of plasticity was ceased after the initiation of damage. Materials with a non-zero Poisson's ratio suffered from spurious mesh dependent hardening in the current damage formulation, which was a consequence the development of a triaxial tensile stress state. Conversely, materials with a zero valued Poisson's ratio yielded mesh independent results for both a square and tapered geometry, as long as the crack band model was used. The viscous models were found to have negligible regularising effects.

In order to rectify the mesh dependent hardening observed in the second study, it is recommended that the degradation of the Poisson's ratio be implemented in the damage formulation. Further, a reformulation of the definition of the equivalent stress could be required if the degraded

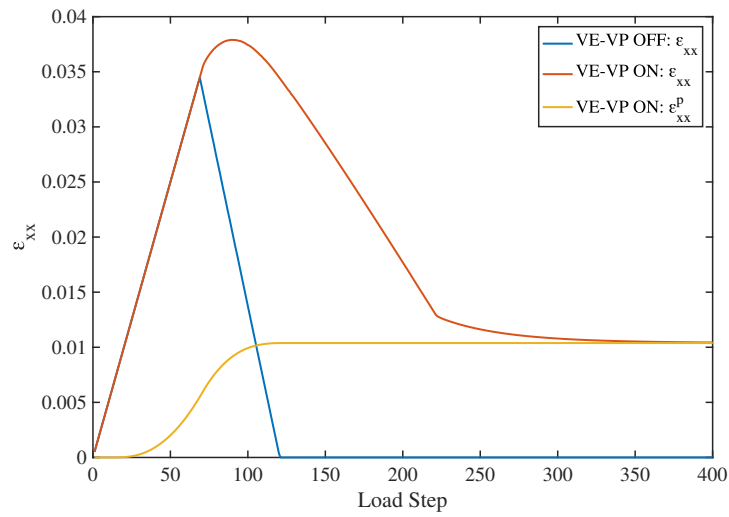


Figure 3.9: Longitudinal strains in the undamaged elements for models with VE-VP off and VE-VP on. Square geometry with $n = 101$.

Poisson's ratio does not yield mesh independent results alone. It is also recommended that further mesh sensitivity studies, such as mesh bias and shear tests, be conducted to ascertain the overall performance of the damage model with respect mesh dependency.

4

Experiments

This section describes the experiments that were undertaken in this thesis and presents the results. Two types of investigations were performed on the Momentive RIMR 135/EPIKURE RIMH 1366 epoxy resin system in order to investigate its mechanical behaviour at different temperatures. The first test comprised of a Dynamic Mechanical Analysis (DMA) test, while the second experiment involved subjecting the epoxy resin to a creep test.

4.1. Dynamic Mechanical Analysis

4.1.1. Experimental Procedure

In this thesis, a DMA test was performed at one loading frequency to investigate the temperature dependent stiffness and glass transition temperature of the Momentive RIMR 135/EPIKURE RIMH 1366 epoxy resin. This test supplements the experimental results performed by Rocha et al. [22] on the same epoxy resin system, in which a DMA test was performed on unaged, saturated, dry and redried epoxy resin samples.

The NETZSCH DMA 242 machine was used to perform the DMA test on a rectangular bar specimen prepared in accordance with ISO 178 for a three point bending test. Table 4.1 presents the dimensions of the specimen used in this test.

Free Bending Length	Average Width	Average Depth
50 mm	10.86 mm	2.82 mm

Table 4.1: Dimensions of the epoxy resin specimen used in the DMA test.

Figure 4.1 summarises the experimental apparatus used by the NETZSCH machine to perform the DMA test. Figure 4.2a is a photograph of an epoxy resin sample in the testing apparatus and Figure 4.2b is a composite image of an epoxy resin sample used in the experiments. In the NETZSCH machine, a furnace controls the temperature of the specimen and in this test the temperature of the specimen is varied from 23°C to 130°C with a temperature ramp of 2°C/min. The DMA machine loads the sample in a mixed force/displacement control depending on the current stiffness of the specimen and uses the corresponding force and displacement to compute the storage modulus E' , loss modulus E'' and the loss factor $\tan \delta$. A loading frequency of 1 Hz was used in this experiment

4.1.2. Experimental Results

The NETZSCH analysis software was used to post-process the raw load displacement data to obtain the material parameters relevant to the DMA test. Figure 4.3 presents a graph of the storage

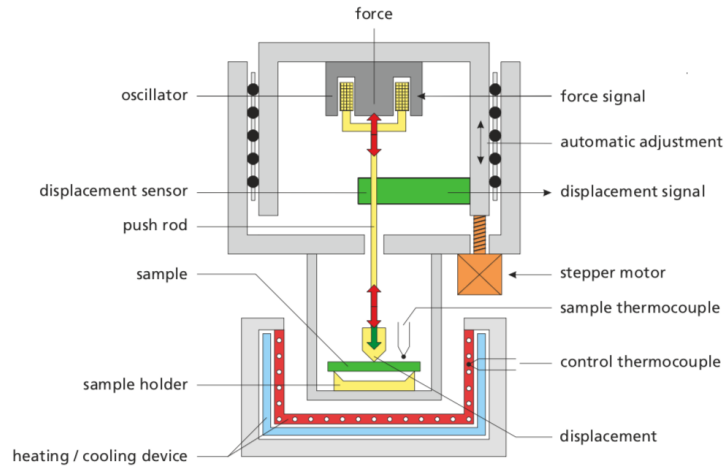
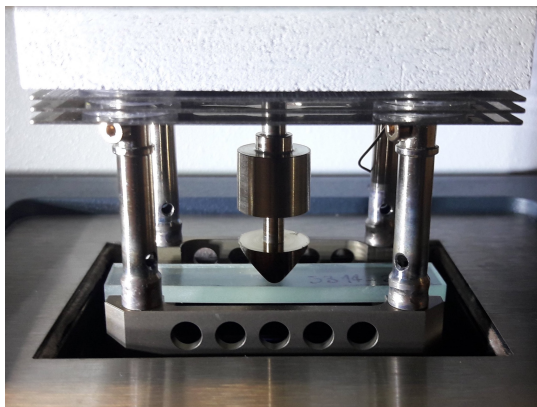
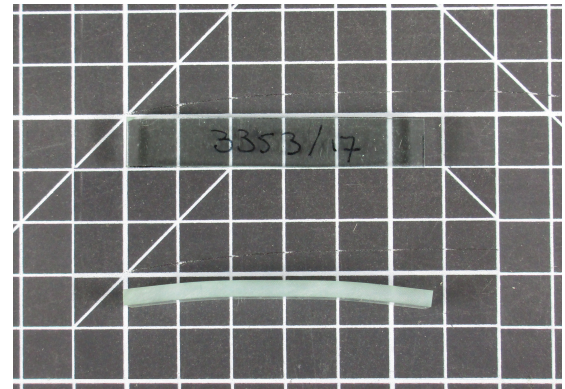


Figure 4.1: Operating principle of the NETZSCH DMA 242 machine [19].



(a) NETZSCH DMA Machine.



(b) Composite photograph of an epoxy resin sample after being subjected to load at an elevated temperature.

Figure 4.2: Photographs of the experimental setup and specimen.

modulus, loss modulus and loss factor as a function of the temperature for the three specimens.

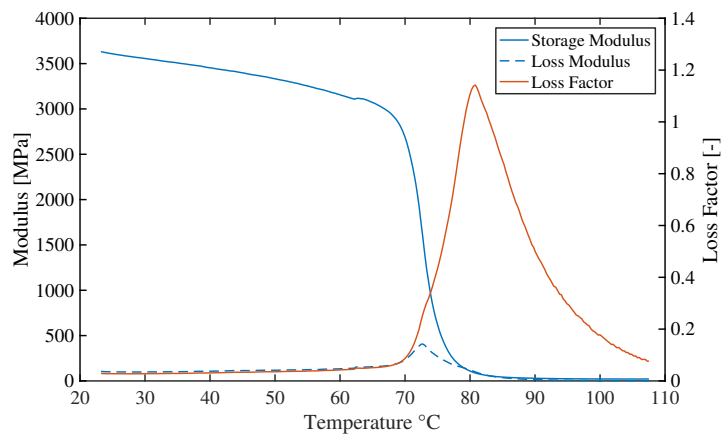


Figure 4.3: Plot of the DMA parameters as a function of the temperature for each epoxy resin specimen.

As the storage modulus in Figure 4.3 is related to the elastic modulus, detailed in Section 2.6.1, a qualitative analysis of the temperature dependence of the storage modulus provides an insight into the thermal variation of the material behaviour of an epoxy resin. At temperatures lower than 65°C, the epoxy resin was in a glassy state and had a relatively high stiffness. Figure 4.3 indicates that the temperature dependence of the elastic modulus in the glassy material state may be approximated by a linear relation. At temperatures higher than 85°C, the epoxy resin was in a rubbery state and had a relatively low stiffness. The stiffness in the rubbery regime was more stable than in the glassy regime and, therefore, can be approximated to be constant.

While there are multiple methods that can be used to characterise the glass transition temperature, the method used by Yu et al. [32] was adopted for this thesis. Yu et al. take the glass transition temperature to be the temperature that is centrally located within the glass transition region. Figure 4.3 shows that this point also approximately coincides with the inflection point on the storage modulus curve and the peak of the loss modulus curve, conveniently corresponding with alternative glass transition determination methods.

From the DMA tests performed on the Momentive RIMR 135/EPIKURE RIMH 1366 epoxy resin samples the glass transition temperature was determined to be $T_g = 72.7^\circ\text{C}$.

4.2. Creep Test

Initially, a stress relaxation test was performed, in which an imposed displacement was applied to the epoxy resin specimen and the relaxing resultant load recorded. However, at elevated temperatures, the epoxy resin lost a significant amount of stiffness and the load relaxed to within the measurement resolution of the load cell, rendering the results unreliable. To counteract this issue, the imposed displacement was increased in the hope that the relaxed load would be high enough to record. However, the required increase in displacement resulted in significant deformation of the epoxy resin sample, with deformations that were in the order of twice the cross-sectional thickness, see Figure 4.4. The raw data from these invalid tests are presented in Appendix D.



Figure 4.4: Photograph of the a highly deformed epoxy resin specimen after a stress relaxation test.

Deformations of this magnitude result in geometric, and most likely material, non-linearities, meaning that the interpretation of the results would be highly complex and invalid in the case of material non-linearities. As a result, an experiment examining the creep behaviour of the epoxy resin was chosen as the most suitable method for determining long term properties. The advantage of the creep test over the relaxation test is that the load can be minimised to reduce deflections but also be kept high enough to ensure measurement accuracy.

4.2.1. Experimental Procedure

Creep tests were performed at three different temperatures to determine the long term elastic stiffness in the glassy, rubbery and mixed states. The creep tests were also undertaken using the NET-

ZSCH DMA 242 machine, with rectangular bar specimens prepared in accordance with ISO 178 for a three point bending test. The free bending length used in the creep test was 50 mm, with the cross-section of the epoxy resin bars approximately 10 mm wide by 3 mm thick. The exact dimensions of the specimens were recorded with a digital micrometre and are presented in Appendix D. The apparatus used in this experiment is identical to that used in the DMA test, see Figures 4.1 and 4.2.

The creep tests were performed at temperatures determined from Figure 4.3 to be clearly in the desired state regimes and were chosen to be 25°C, 75°C and 100°C for the glassy, mixed and rubbery regimes respectively. A temperature ramp of 2°C/min was used to preheat the specimens to the target temperature and an equilibration time of 10 minutes allowed the specimens to reach a thermal equilibrium before commencing the creep test. A constant load was then applied to the specimen and the resulting creep deflection was recorded at a sampling rate of 0.25 Hz. The creep tests were performed for a duration of more than an hour, after which a majority of the short term viscoelastic stresses had relaxed. Table 4.2 presents the applied load and test duration for each tested temperature.

	Test 1	Test 2	Test 3
Temperature	25°C	75°C	100°C
Applied load	2 N	0.5 N	0.2 N
Test Duration	1 hr	2 hrs	2 hrs

Table 4.2: Temperature, applied load and test duration for the creep tests.

4.2.2. Experimental Results

Figure 4.5 presents the elastic stiffness results for the creep tests at the three different temperatures. The raw load displacement data from the creep tests can be found in Appendix D. The elastic stiffness E was calculated from Euler-Bernoulli beam theory as per Section 2.6.2. Equation 2.23 can be rearranged to isolate the elastic stiffness, given the geometry of the specimen, the force and the displacement:

$$E = \frac{FL^3}{48uI} \quad (4.1)$$

Further, to ensure elastic deformation, the maximum fibre stress can be calculated from the applied load and the geometry of the section as per Equation 2.24. From Rocha et al. [24] the yield stress of the tested epoxy resin in a glassy state was determined to be $\sigma_t^{\text{gla}} = 64.8$ MPa. Although the yield stress of the epoxy resin in the rubbery state was unknown at the time of testing, a reference value was taken from the calibration undertaken by Yu et al., in which $\sigma_t^{\text{rub}} = 9$ MPa.

In Figure 4.5, the initial stiffness for the temperatures of 25°C and 75°C was relatively high, after which significant decay of the elastic modulus occurred over the duration of the test. The test at 100°C showed a faster relaxation than the test at 75°C, however significantly less initial stiffness than both the 25°C and 75°C tests. This response highlights the highly time dependent mechanical behaviour of the epoxy resin, further adding support for the use of viscous material models. Overall, the relaxation times of the epoxy resin when in a glassy state were faster than in the mixed and rubbery states. Further, the relative degree of viscoelastic stiffness decreased as the temperature increased. Therefore, by modifying both the viscoelastic stiffnesses and relaxation times, the observed state dependent material response can be captured with a degrading viscoelasticity model.

By the end of the creep tests, the variation in the elastic modulus was relatively small when compared to the initial viscoelastic stiffnesses. Although it appeared that the specimens would continue

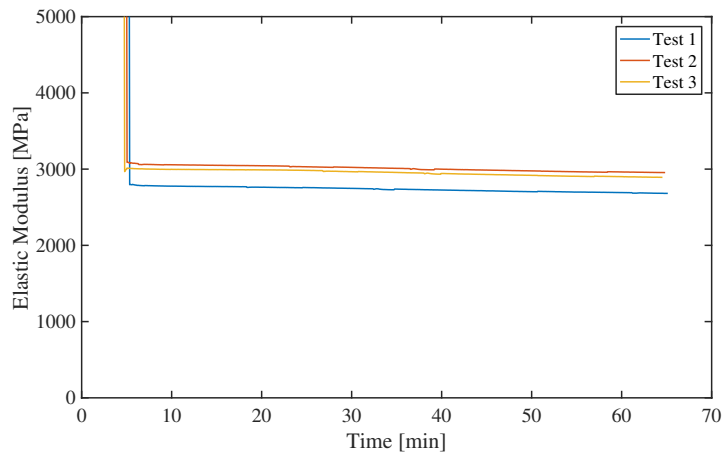
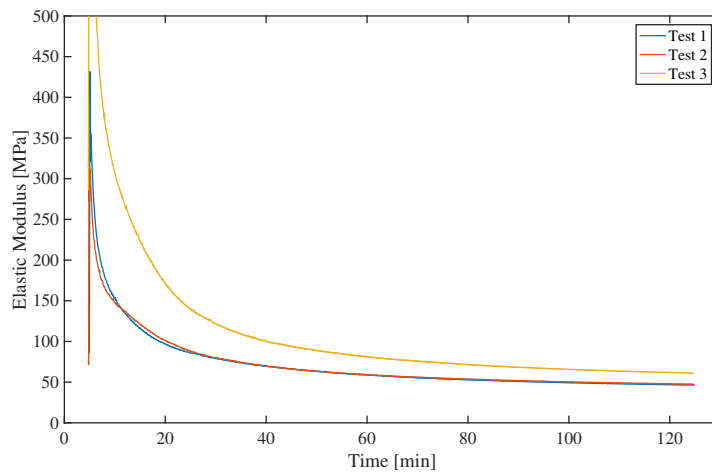
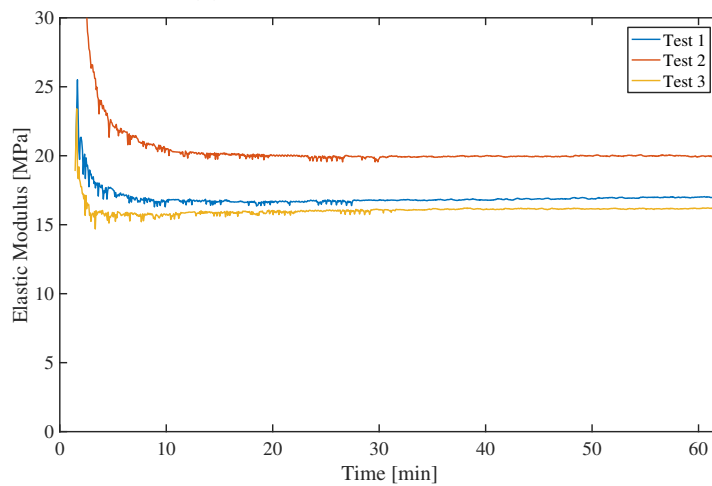
(a) Elastic stiffness for $T = 25^{\circ}\text{C}$.(b) Elastic stiffness for $T = 75^{\circ}\text{C}$.(c) Elastic stiffness for $T = 100^{\circ}\text{C}$.

Figure 4.5: Calculated elastic stiffness results from the creep test as a function of test time.

to experience minor creep deflections if the load was held for an extended period of time, it is sufficient to encapsulate these small viscoelastic stiffnesses in the long term elastic modulus. From a modelling perspective, the long term elastic modulus corresponds to a viscoelastic stiffness with an infinite relaxation time. Thus, if the significant viscoelastic behaviour of the material occurs at

relatively quick relaxation time and the primary loads of interest occur at correspondingly high frequencies, as is the case for most epoxy applications, the long term elastic modulus can be redefined to include these small viscoelastic stresses with significantly large relaxation times. One drawback of this approach is that it would not be possible to model long term creep behaviour because longer duration experiments would need to be carried out to completely isolate the long term stiffness.

The final data points for the creep tests were used to calculate the average long term elastic modulus of the epoxy resin. Table 4.3 presents the long term elastic modulus for each tested temperature and the corresponding analytical maximum fibre stress for each experiment. The calculated elastic moduli are consistent with the trends observed in the DMA test, refer Figure 4.3. Further, the maximum fibre stresses were significantly below the yield strengths in the glassy and rubbery regimes and, thus, it can be assumed that the response of the epoxy resin was elastic for each creep test.

Temperature	25°C	75°C	100°C
Long term elastic modulus E_{∞}	2843 MPa	51.51 MPa	17.73 MPa
Maximum fibre stress σ	1.88 MPa	0.47 MPa	0.19 MPa

Table 4.3: Long term elastic modulus and maximum fibre stress.

5

Methods

In this section, the numerical framework for modelling an epoxy resin is formulated in the context of the finite element method. The material model has been implemented in C++ using the Jive programming toolkit [9] in conjunction with an existing finite element framework developed by Rocha et al. [24]. As a result, the numerical framework is concerned only with developing the constitutive laws for an epoxy resin and their implementation in a finite element procedure. A full description of the constitutive model implemented in Jive can be found in Appendix B.

5.1. Overview of the Framework

The multiphysics numerical framework incorporates three physical models that represent heat conduction, moisture diffusion and continuum mechanics respectively. The three models are arranged in a one-way coupling utilising the operator split method, in which the heat model is solved first, then followed by the diffusion model and finally the mechanics model, see Figure 5.1. The order of the coupling is consistent with the assumptions made in the formulation of each model.

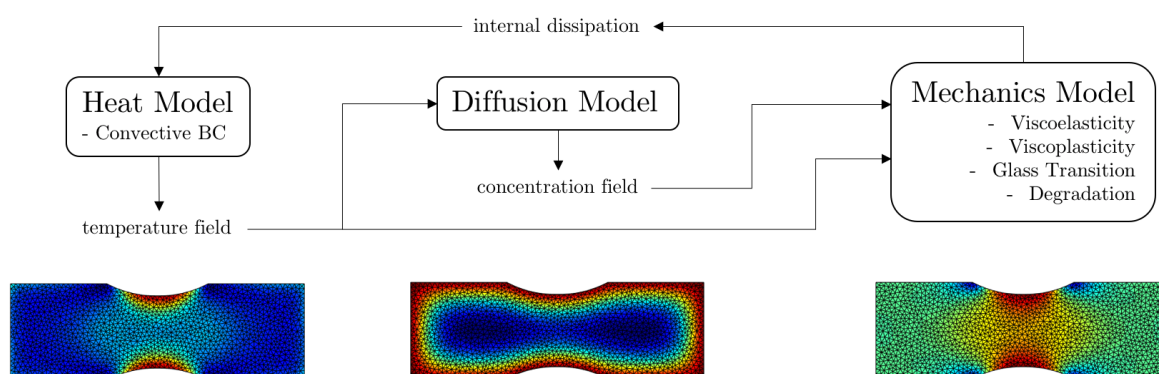


Figure 5.1: Overview of the multiphysics numerical framework.

The transport models describing heat conduction and moisture diffusion are based on the classical Equations described in Section 2.3 and are not modified in this thesis. The finite element implementation of the heat and diffusion models is briefly described in Sections 5.2 and 5.3 respectively. The formulation of the mechanics model is described in Section 5.4 and addresses the second and third research questions proposed in Section 1.2. Finally, the details of the multiphysics framework, in which the three material models are unified, are given in Section 5.5.

5.2. Formulation of the Heat Model

In this section, the finite element formulation for the heat model is derived from the constitutive relationship described in Section 2.3.1. In this model a linear heat conductivity matrix that is independent of the current temperature, the moisture content and the stress state is adopted. Although humidity dependent heat transfer was observed by some authors, the dependence was found to be relatively weak and is therefore assumed to be independent in this thesis.

This heat formulation allows for transient behaviour, in which a convective boundary condition is established and internal heat generation is considered.

Strong Formulation

The formulation begins with Fourier's law of heat conduction from Equation 2.15:

$$\mathbf{q} = -\boldsymbol{\kappa}\nabla T \quad (5.1)$$

where \mathbf{q} is the heat flux vector, $\boldsymbol{\kappa}$ is the heat conductivity matrix and ∇T is the temperature gradient. Considering the differential volume element depicted in Figure 5.2, the conservation of heat energy can be written as:

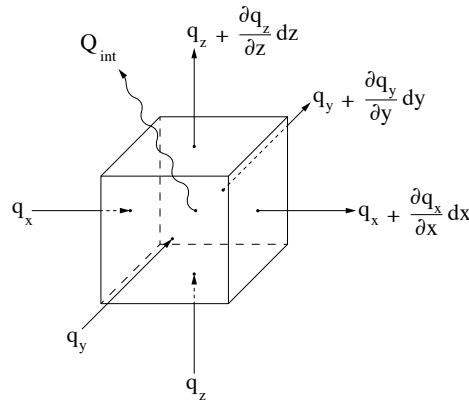


Figure 5.2: Heat fluxes acting on a differential element.

$$(Q_{\text{int}} - \nabla \cdot \mathbf{q}) dx dy dz = \Delta Q \quad (5.2)$$

where Q_{int} is the internal heat generation from internal dissipative processes, such as viscous deformations. The net inflow of heat ΔQ is related to a change in temperature through Equation 2.16, which is rewritten for the differential element as:

$$\Delta Q = \rho c \dot{T} dx dy dz \quad (5.3)$$

where ρ is the density, c is the specific heat and \dot{T} is the temperature time derivative. Combining equations 5.1, 5.2 and 5.3 results in the strong formulation of the heat model:

$$\nabla \cdot (\boldsymbol{\kappa}\nabla T) + Q_{\text{int}} = \rho c \dot{T} \quad (5.4)$$

Boundary Conditions

Three types of boundary conditions are incorporated into the formulation of the heat model, namely the Dirichlet, Neumann and Robin boundary conditions. The specifics of each boundary condition acting on surface Γ are elaborated below.

Dirichlet Boundary Condition:

A fixed temperature T_i is prescribed on the boundary Γ_T of the domain:

$$T|_{\Gamma_T} = T_i \quad (5.5)$$

Neumann Boundary Condition:

A heat flux q_i , defined as positive when acting into the body, is prescribed on the boundary of the domain Γ_q :

$$-\mathbf{q} \cdot \mathbf{n}|_{\Gamma_q} = q_i \quad (5.6)$$

where \mathbf{n} is an outward facing normal vector.

Robin Boundary Condition:

A thermal interaction between the domain and its surrounding fluid is specified by a Robin boundary condition. In this case, the heat flux is related to the temperature differential between the temperature T on the boundary Γ_h , and the ambient temperature of the fluid T_f . The heat flux across the boundary is related to this differential through the coefficient of heat transfer, h :

$$-\mathbf{q} \cdot \mathbf{n}|_{\Gamma_h} = h(T_f - T) \quad (5.7)$$

This boundary condition is the most relevant in the multiphysics framework because it allows the modelling of the heat transfer between a specimen and its surrounding fluid, such as air or water.

Weak Formulation

To develop the weak form, the strong form is multiplied by a scalar weight function $w \in \mathcal{V}$ and is integrated over the domain Ω :

$$\int_{\Omega} w \nabla \cdot (\boldsymbol{\kappa} \nabla T) \, d\Omega + \int_{\Omega} w Q_{\text{int}} \, d\Omega = \int_{\Omega} w \rho c \dot{T} \, d\Omega \quad \forall w \in \mathcal{V} \quad (5.8)$$

Integrating the first term in the above equation by parts yields:

$$\int_{\Omega} w \nabla \cdot (\boldsymbol{\kappa} \nabla T) \, d\Omega = \int_{\Gamma} -w \mathbf{q} \cdot \mathbf{n} \, d\Gamma - \int_{\Omega} \nabla w \cdot (\boldsymbol{\kappa} \nabla T) \, d\Omega \quad (5.9)$$

where \mathbf{q} represents the boundary fluxes from the Neumann and Robin boundary conditions. This is because the boundary Γ consists of $\Gamma \equiv \Gamma_T \cup \Gamma_q \cup \Gamma_h$. Substituting the above equation into Equation 5.8 yields:

$$-\int_{\Omega} \nabla w \cdot (\boldsymbol{\kappa} \nabla T) \, d\Omega - \int_{\Gamma_q} w \mathbf{q} \cdot \mathbf{n} \, d\Gamma - \int_{\Gamma_h} w \mathbf{q} \cdot \mathbf{n} \, d\Gamma + \int_{\Omega} w Q_{\text{int}} \, d\Omega = \int_{\Omega} w \rho c \dot{T} \, d\Omega \quad \forall w \in \mathcal{V} \quad (5.10)$$

Applying the boundary conditions, $-\mathbf{q} \cdot \mathbf{n} = q_i$ over Γ_q and $-\mathbf{q} \cdot \mathbf{n} = h(T_f - T)$ over Γ_h , results in the weak formulation of the heat model:

$$\int_{\Omega} \nabla w \cdot (\boldsymbol{\kappa} \nabla T) \, d\Omega + \int_{\Gamma_h} w h T \, d\Gamma + \int_{\Omega} w \rho c \dot{T} \, d\Omega = \int_{\Gamma_h} w h T_f \, d\Gamma + \int_{\Gamma_q} w q_i \, d\Gamma + \int_{\Omega} w Q_{\text{int}} \, d\Omega \quad \forall w \in \mathcal{V} \quad (5.11)$$

Finite Element Formulation

The computational domain is discretised with finite elements that are defined by shape functions \mathbf{N} and their derivatives \mathbf{B} , resulting in the following expressions:

$$\begin{aligned} T &= \mathbf{N}T_e & w &= \mathbf{N}w_e \\ \nabla T &= \mathbf{B}T_e & \nabla w &= \mathbf{B}w_e \end{aligned} \quad (5.12)$$

where the subscript e denotes element level nodal values. The shape functions are inserted into the weak form for a single element. The weak form is considered valid for all $w \in \mathcal{V}$. The resulting finite element formulation for the heat model involves the assembly of the element level matrices and vectors:

$$\mathbb{A}_e \left\{ (\mathbf{k}_{h,e} + \mathbf{h}_{h,e}) T_e + \mathbf{c}_{h,e} \dot{T}_e = \mathbf{r}_h + \mathbf{r}_q + \mathbf{r}_Q \right\} \quad (5.13)$$

where \mathbb{A} is the assembly operator and the element matrices and vectors are as follows:

$$\begin{aligned} \mathbf{k}_{h,e} &= \int_{\Omega_e} \mathbf{B}^T \boldsymbol{\kappa} \mathbf{B} d\Omega & \mathbf{r}_h &= \int_{\Gamma_{h,e}} \mathbf{N}^T h T_f d\Gamma \\ \mathbf{h}_{h,e} &= \int_{\Gamma_{h,e}} \mathbf{N}^T h \mathbf{N} d\Gamma & \mathbf{r}_q &= \int_{\Gamma_{q,e}} \mathbf{N}^T q_i d\Gamma \\ \mathbf{c}_{h,e} &= \int_{\Omega_e} \mathbf{N}^T \rho c \mathbf{N} d\Omega & \mathbf{r}_Q &= \int_{\Omega_e} \mathbf{N}^T Q_{\text{int}} d\Omega \end{aligned} \quad (5.14)$$

5.3. Formulation of the Diffusion Model

In this section, the finite element formulation for the heat model is derived from the constitutive relationship described in Section 2.3.2. Both heat conduction and moisture diffusion are transport problems and thus have similar governing equations. As a result, a majority of the formulation presented in the previous section is also valid for the formulation of the diffusion model and thus only the differences in the two formulations are highlighted in this section.

In this model, a linear diffusivity matrix that is independent of the stress state is adopted. This diffusion formulation allows for transient behaviour and a diffusivity matrix that is temperature dependent.

The governing constitutive law for diffusion is Fick's first law of diffusion as outlined in Equation 2.18:

$$\mathbf{j} = -\mathbf{D}_\omega(T) \nabla \omega \quad (5.15)$$

where \mathbf{j} is the moisture flux vector, $\mathbf{D}_\omega(T)$ is the temperature dependent diffusivity matrix and $\nabla \omega$ is the moisture concentration gradient. Considering the differential volume element depicted in Figure 5.3, the conservation of mass can be written as:

$$-\nabla \cdot \mathbf{j} = \Delta \omega \quad (5.16)$$

Combining equations 5.15 and 5.16 results in the strong formulation of the diffusion model:

$$\nabla \cdot (\mathbf{D}_\omega(T) \nabla \omega) = \dot{\omega} \quad (5.17)$$

In contrast with the heat conduction model, only the Dirichlet and Neumann boundary conditions are considered as the wetting process is modelled by setting the boundary concentrations to be equal to the saturated moisture content. As a result, the weak formulation can be derived in a similar manner to the previous section:

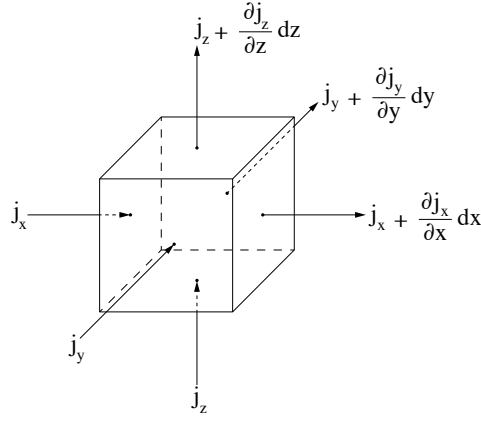


Figure 5.3: Moisture fluxes acting on a differential element.

$$\int_{\Omega} \nabla w \cdot (\mathbf{D}_{\omega}(T) \nabla \omega) d\Omega + \int_{\Omega} w \dot{\omega} d\Omega = \int_{\Gamma_j} w j_i d\Gamma \quad \forall w \in \mathcal{V} \quad (5.18)$$

The same shape functions are used to describe the weight function w and the moisture content ω . The resulting finite element formulation for the diffusion model involves the assembly of the element level matrices and vectors:

$$\mathbb{A}_e \left\{ \mathbf{k}_{\omega,e} \omega_e + \mathbf{c}_{\omega,e} \dot{\omega}_e = \mathbf{r}_j \right\} \quad (5.19)$$

where \mathbb{A} is the assembly operator and the element matrices and vectors are as follows:

$$\mathbf{k}_{\omega,e} = \int_{\Omega_e} \mathbf{B}^T \mathbf{D}_{\omega}(T) \mathbf{B} d\Omega \quad \mathbf{c}_{\omega,e} = \int_{\Omega_e} \mathbf{N}^T \mathbf{N} d\Omega \quad \mathbf{r}_j = \int_{\Gamma_{j,e}} \mathbf{N}^T j_i d\Gamma \quad (5.20)$$

5.4. Formulation of the Mechanics Model

The formulation of the mechanics model begins with the governing equation of equilibrium:

$$\nabla \cdot \boldsymbol{\sigma} + \mathbf{b} = 0 \quad (5.21)$$

where $\boldsymbol{\sigma}$ is the stress tensor in Voigt notation and \mathbf{b} is the vector of body forces. In this thesis, the small strain relationship is used:

$$\boldsymbol{\varepsilon} = \frac{1}{2} ((\nabla \mathbf{u})^T + \nabla \mathbf{u}) \quad (5.22)$$

where $\boldsymbol{\varepsilon}$ is the strain tensor in Voigt notation and \mathbf{u} is the displacement vector. A constitutive relationship between the stress and strain tensors is established and takes the following form:

$$\boldsymbol{\sigma} = \mathbf{D} \boldsymbol{\varepsilon} \quad (5.23)$$

where \mathbf{D} is the mechanical constitutive matrix. In a similar manner to the previous formulations, the governing equation is multiplied by a weight function and the Dirichlet and Neumann boundary conditions are applied to arrive at the weak formulation:

$$\int_{\Omega} \nabla w \cdot (\mathbf{D} \boldsymbol{\varepsilon}) d\Omega = \int_{\Omega} w \cdot \mathbf{b} + \int_{\Gamma_t} w \cdot \mathbf{t}_h d\Gamma = 0 \quad \forall w \in \mathcal{V} \quad (5.24)$$

where \mathbf{t}_h is the external traction vector acting on the boundary Γ_t . The same shape functions are used to describe the weight function w and displacement vector \mathbf{u} . The resulting finite element formulation for the mechanics model involves the assembly of the element level matrices and vectors:

$$\mathbb{A}_e \{ \mathbf{k}_{m,e} \mathbf{u}_e = \mathbf{f}_b + \mathbf{f}_t \} \quad (5.25)$$

where \mathbb{A} is the assembly operator and the element matrices and vectors are as follows:

$$\mathbf{k}_{m,e} = \int_{\Omega_e} \mathbf{B}^T \mathbf{D} \mathbf{B} d\Omega \quad \mathbf{f}_b = \int_{\Omega_e} \mathbf{N}^T \mathbf{b} d\Omega \quad \mathbf{f}_t = \int_{\Gamma_{t,e}} \mathbf{N}^T \mathbf{t}_h d\Gamma \quad (5.26)$$

5.4.1. Overview of the Mechanical Constitutive Models

The mechanical model of the epoxy resin attempts to capture the various behaviours described in Section 2.1 through the incorporation of the following material models:

- (a) *Glass Transition Model*: Describes the state of the material as a function of the temperature and moisture concentration of the epoxy. The state of the epoxy resin can be glassy, rubbery or a combination of the two.
- (b) *Degradation Model*: Describes how the various material properties change with the state of the epoxy.
- (c) *Viscoelasticity Model*: Describes the time dependent elastic behaviour.
- (d) *Viscoplasticity Model*: Describes the time dependent plastic behaviour.

In this thesis, two constitutive models are considered, with each model relating to a specific research question outlined in Section 1.2. With reference to the individual material models described above, the ingredients of each constitutive model are described below:

Constitutive Model 1: Glass Transition Model + Degradation Model + Linear Viscoelasticity Model + Viscoplasticity Model

Constitutive Model 2: Glass Transition Model + Degradation Model + Non-Linear Viscoelasticity Model + Viscoplasticity Model

In Constitutive Model 1 the mechanical behaviour of the epoxy resin accounts for both moisture and thermal effects, thus addressing the second research question. Constitutive Model 2 extends the formulation of Constitutive Model 1 by introducing a non-linear viscoelasticity material model in order to address the third research question relating to the behaviour of the epoxy resin at large strains.

The specifics of each material model are described in Sections 5.4.2 to 5.4.5. Section 5.4.6 describes the formulation and implementation of the computational algorithm required to couple non-linear viscoelasticity and viscoplasticity in the same constitutive model.

5.4.2. Glass Transition Model

The glass transition model used in the thesis is based on the work by Yu et al. [32], in which a glass transition surface Φ_{tr} that is a function of both the temperature and moisture content of the epoxy resin is defined. The degree of glass transition is characterised by the scalar parameter ζ and describes the state of the epoxy resin. Following on from the molecular behaviour of the material, an epoxy resin can be conceived to exist in three different material states:

- (i) Glassy state, where $\zeta = 0$.
- (ii) Mixed glassy-rubbery state, where $0 < \zeta < 1$.
- (iii) Rubbery state, where $\zeta = 1$.

As a result, the glass transition surface describes the transition of an epoxy resin from a glassy state to a rubbery state and has similar properties to a yield surface used in classical plasticity. This allows the Kuhn-Tucker conditions to be imposed for glass transition:

$$\begin{aligned}\dot{\zeta} &\geq 0 \\ \Phi_{\text{tr}} &\leq 0 \\ \dot{\zeta}\Phi_{\text{tr}} &= 0\end{aligned}\tag{5.27}$$

Yu et al. propose the following expression for the glass transition surface Φ_{tr} :

$$\Phi_{\text{tr}} = \pi_{\text{tr}} - \pi_c\tag{5.28}$$

where π_c is a derived constant and π_{tr} is the thermodynamic driving force of $\dot{\zeta}$ and is defined as:

$$\pi_{\text{tr}} = \phi_T(T - T_0) + \phi_\omega\sqrt{\omega} - H\zeta\tag{5.29}$$

where ϕ_T and ϕ_ω are material parameters relating to the relative driving forces of temperature and moisture change on the degree of glass transition, and H describes the temperature range in which glass transition occurs. Equation 5.29 implies that the rate of glass transition is linearly related to the material temperature and dependent on the square root of the moisture content, the latter of which is implied from the experimental results of Chen et al. [4].

The expression of Equation 5.29 also allows the π_c term to be derived. With the definition of glass transition occurring at $T = T_g$, $\zeta = 0.5$ and $\omega = 0$, the application of the Kuhn-Tucker conditions results in:

$$\pi_c = \phi_T(T_g - T_0) - \frac{H}{2}\tag{5.30}$$

Combining Equations 5.28, 5.29 and 5.30 with the Kuhn-Tucker conditions for glass transition, allows the degree of glass transition at any point in time to be explicitly expressed as a function of the temperature and moisture content of the epoxy resin, as well as the degree of glass transition at the previous time step:

$$\zeta(t + \Delta t) = \begin{cases} 0 & \text{if } \zeta^* \leq 0 \text{ and } \dot{\zeta} < 0 \\ \zeta(t) & \text{if } \dot{\zeta} < 0 \\ \zeta^* & \text{if } \dot{\zeta} \geq 0 \\ 1 & \text{if } \zeta^* \geq 1 \end{cases}\tag{5.31}$$

where:

$$\zeta^* = \frac{\phi_T(T - T_g) + \phi_\omega\sqrt{\omega} + \frac{H}{2}}{H}\tag{5.32}$$

Figure 5.4 presents the glass transition diagram, which shows the relationship between the temperature and moisture concentration of an epoxy resin, and its material state, characterised by the degree of glass transition ζ . The parameters chosen for this representation are as follows: $\phi_T = 1$ MPa, $\phi_\omega = 500$ MPa, $H = 20$ MPa and $T_g = 363.3$ K.

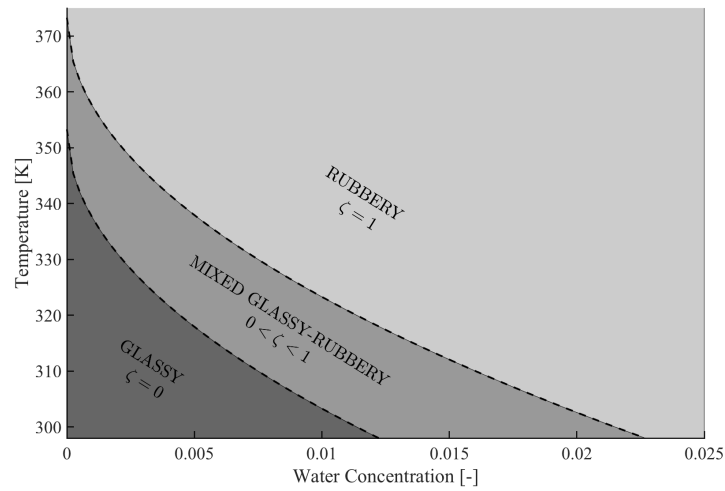


Figure 5.4: Glass transition diagram for an epoxy resin based on the glass transition surface used in this thesis.

5.4.3. Degradation Model

The purpose of the degradation model is to relate the current state of the epoxy resin to its current material properties. Following on from the work on Yu et al. [32], the relevant material properties of the epoxy resin are assumed to be constant in the glassy and rubbery states, and are linearly interpolated based on the degree of glass transition ζ in the mixed state. This is highlighted in Figure 5.5 which is consistent with the experimental behaviour observed in Figure 4.3.

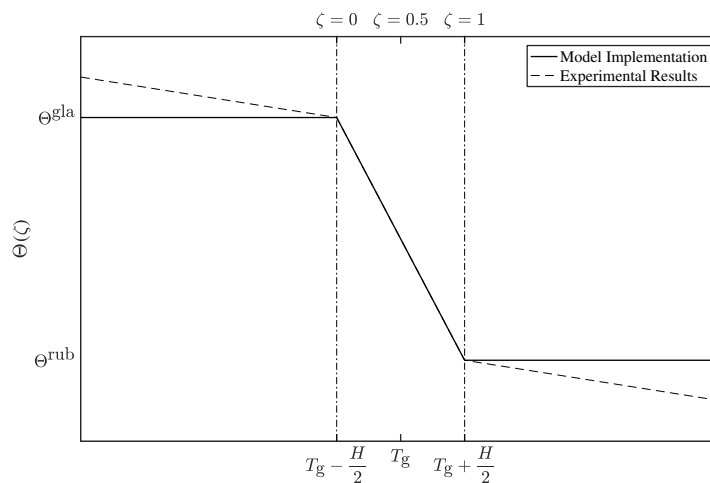


Figure 5.5: Basis of the degradation model used in this thesis. Temperatures and corresponding degrees of glass transition relate to a dry state.

As a result, the state dependent material properties are described by the single scalar valued state parameter ζ and the degradation relationship can be generalised as follows:

$$\Theta(\zeta) = (1 - \zeta)\Theta^{\text{gla}} + \zeta\Theta^{\text{rub}} \quad (5.33)$$

where $\Theta(\zeta)$, a function of the degree of glass transition ζ , is the value of an arbitrary material property for the current state of the epoxy resin, Θ^{gla} is the value of the material property in the glassy state and Θ^{rub} is the value of the material property in the rubbery state. While this method simplifies the material behaviour by imposing a constant property when the epoxy resin is in a glassy or rubbery state and a linearly interpolated property for the mixed state, this assumption has been found to give reasonably accurate results [32].

A departure from the model proposed by Yu et al. is that, in this thesis, a stiffness based approach to the degradation model was adopted. This is in contrast to the compliance based methods used by Yu et al. This approach was adopted because it is simpler to implement and more consistent with a strain driven finite element implementation, in which a stiffness is used to derive stresses from strains. For example, in the work by Yu et al., the expression for the long term elastic modulus can be established from the compliance relation as:

$$E_{\infty}(\zeta) = \left((1 - \zeta) \frac{1}{E_{\infty}^{\text{gl}a}} + \zeta \frac{1}{E_{\infty}^{\text{rub}}} \right)^{-1} \quad (5.34)$$

However in this thesis, the current elastic modulus is defined as:

$$E_{\infty}(\zeta) = (1 - \zeta) E_{\infty}^{\text{gl}a} + \zeta E_{\infty}^{\text{rub}} \quad (5.35)$$

Not all material properties require degradation. In the proceeding material models, the degradation relationship of individual parameters will be defined with reference to the linear interpolation model described in Equation 5.33.

5.4.4. Viscoelasticity Model

5.4.4.1. Linear Viscoelasticity

The linear viscoelasticity model used in this thesis is based on the model used by Rocha et al. [24], extending it to incorporate material degradation in line with Section 5.4.3. As outlined in Section 2.2.2, the updated viscoelastic stress consists of a long term elastic component and the summation of exponentially decaying volumetric and deviatoric viscoelastic components:

$$\boldsymbol{\sigma}^e(\zeta, t) = \mathbf{D}_{\infty}(\zeta) \boldsymbol{\epsilon}^e(t) + \sum_{i=1}^N p_i^{\text{ve}}(\zeta, t) \delta_{ij} + \sum_{i=1}^N \mathbf{S}_i^{\text{ve}}(\zeta, t) \quad (5.36)$$

where $\mathbf{D}_{\infty}(t)$ is the long term elastic stiffness matrix, $\boldsymbol{\epsilon}^e$ is the elastic strain and the volumetric and deviatoric viscoelastic stress contributions, p_i^{ve} and \mathbf{S}_i^{ve} respectively, are given by:

$$p_i^{\text{ve}}(\zeta, t) = \exp\left(-\frac{\Delta t}{\lambda_{i,k}}\right) p_i^{\text{ve}}(t - \Delta t) + K_i(\zeta) \left[1 - \exp\left(-\frac{\Delta t}{\lambda_{i,k}}\right) \right] \frac{\lambda_{i,k}}{\Delta t} \Delta \epsilon_v^e \quad (5.37a)$$

$$\mathbf{S}_i^{\text{ve}}(\zeta, t) = \exp\left(-\frac{\Delta t}{\lambda_{i,g}}\right) \mathbf{S}_i^{\text{ve}}(t - \Delta t) + 2G_i(\zeta) \left[1 - \exp\left(-\frac{\Delta t}{\lambda_{i,g}}\right) \right] \frac{\lambda_{i,g}}{\Delta t} \Delta \boldsymbol{\epsilon}_d^e \quad (5.37b)$$

where $\lambda_{i,k}$ and $\lambda_{i,g}$ are the bulk and shear relaxation times for the i^{th} Prony elements, $K_i(\zeta)$ and $G_i(\zeta)$ are the bulk and shear stiffnesses of the i^{th} Prony elements, and $\Delta \epsilon_v^e$ and $\Delta \boldsymbol{\epsilon}_d^e$ are the volumetric and deviatoric components of the elastic strain increment.

In this linear viscoelastic material model, all stiffness quantities have been extended to be material state dependent. In Equation 5.36, $\mathbf{D}_{\infty}(\zeta)$ is constructed from the long term elastic modulus $E_{\infty}(\zeta)$ and the long term Poisson's ratio $\nu_{\infty}(\zeta)$, which are both material state dependent. In Equations 5.37a and 5.37b, both the bulk and shear moduli have also been made a function of the state of the material. Box 5.4.1 summarises the degradation relationships for these four parameters.

Box 5.4.1: Degradation of Linear Viscoelasticity Parameters

The degradation of the long term elastic modulus and the Poisson's ratio take the same form as Equation 5.33:

$$E_{\infty}(\zeta) = (1 - \zeta)E_{\infty}^{\text{gla}} + \zeta E_{\infty}^{\text{rub}} \quad (5.38a)$$

$$\nu_{\infty}(\zeta) = (1 - \zeta)\nu_{\infty}^{\text{gla}} + \zeta \nu_{\infty}^{\text{rub}} \quad (5.38b)$$

The degradation of the viscoelastic bulk and shear moduli have been formulated to remain consistent with the degradation of long term elastic modulus and the Poisson's ratio. First the equivalent degraded elastic modulus and the Poisson's ratio for each Prony element are computed given the glassy and rubbery bulk and shear moduli^a, that is K_i^{gla} and G_i^{gla} , and K_i^{rub} and G_i^{rub} respectively:

$$E_i^{\text{ve}}(\zeta) = (1 - \zeta) \frac{9K_i^{\text{gla}}G_i^{\text{gla}}}{3K_i^{\text{gla}} + G_i^{\text{gla}}} + \zeta \frac{9K_i^{\text{rub}}G_i^{\text{rub}}}{3K_i^{\text{rub}} + G_i^{\text{rub}}} \quad (5.39a)$$

$$\nu_i^{\text{ve}}(\zeta) = (1 - \zeta) \frac{3K_i^{\text{gla}} - 2G_i^{\text{gla}}}{2(3K_i^{\text{gla}} + G_i^{\text{gla}})} + \zeta \frac{3K_i^{\text{rub}} - 2G_i^{\text{rub}}}{2(3K_i^{\text{rub}} + G_i^{\text{rub}})} \quad (5.39b)$$

From this, the state dependent bulk and shear moduli can be computed^b:

$$K_i(\zeta) = \frac{E_i^{\text{ve}}}{3(1 - 2\nu_i^{\text{ve}})} \quad (5.40a)$$

$$G_i(\zeta) = \frac{E_i^{\text{ve}}}{2(1 + \nu_i^{\text{ve}})} \quad (5.40b)$$

^aFor an isotropic linear elastic material: $E = \frac{9KG}{3K+G}$; $\nu = \frac{3K-2G}{2(3K+G)}$

^bFor an isotropic linear elastic material: $K = \frac{E}{3(1-2\nu)}$; $G = \frac{E}{2(1+\nu)}$

The total elastic stiffness consists of the summation of the long term elastic stiffness and the viscoelastic stiffness for the time increment:

$$\mathbf{D}^e(\zeta, \Delta t) = \mathbf{D}_{\infty}(\zeta) + \mathbf{D}^{\text{ve}}(\zeta, \Delta t) \quad (5.41)$$

The long term elastic stiffness for an isotropic material is given by the following expression:

$$\mathbf{D}_{\infty}(\zeta) = \frac{\nu_{\infty}(\zeta)E_{\infty}(\zeta)}{(1 + \nu_{\infty}(\zeta))(1 - 2\nu_{\infty}(\zeta))} \mathbf{I} \otimes \mathbf{I} + 2 \frac{E_{\infty}(\zeta)}{2(1 + \nu_{\infty}(\zeta))} \mathbf{I} \quad (5.42)$$

where \mathbf{I} is the second order identity tensor and \mathbf{I} is the fourth order identity tensor. Similarly, the viscoelastic stiffness for an isotropic material is given by:

$$\mathbf{D}^{\text{ve}}(\zeta, \Delta t) = \left(K_{\text{ve}}(\zeta, \Delta t) - \frac{2}{3}G_{\text{ve}}(\zeta, \Delta t) \right) \mathbf{I} \otimes \mathbf{I} + 2G_{\text{ve}}(\zeta, \Delta t) \mathbf{I} \quad (5.43)$$

where the bulk and shear viscoelastic stiffnesses are derived from Equations 5.37a and 5.37b:

$$K^{\text{ve}}(\zeta, \Delta t) = \frac{\partial p^{\text{ve}}}{\partial \Delta \epsilon_v^e} = \sum_{i=1}^N \left[1 - \exp\left(-\frac{\Delta t}{\lambda_{i,k}}\right) \right] \left(\frac{K_i(\zeta) \lambda_{i,k}}{\Delta t} \right) \quad (5.44a)$$

$$G^{\text{ve}}(\zeta, \Delta t) = \frac{\partial \mathbf{S}^{\text{ve}}}{\partial \Delta \epsilon_d^e} = \sum_{i=1}^N \left[1 - \exp\left(-\frac{\Delta t}{\lambda_{i,g}}\right) \right] \left(\frac{G_i(\zeta) \lambda_{i,g}}{\Delta t} \right) \quad (5.44b)$$

Finally, the energy dissipation¹ resulting from viscoelasticity can be determined:

$$\Xi^{\text{ve}}(\zeta, t) = \sum_{i=1}^N \frac{(p_i^{\text{ve}})^2}{2K_i(\zeta) \lambda_{i,k}} + \sum_{i=1}^N \frac{\mathbf{S}_i^{\text{ve}} \cdot \mathbf{S}_i^{\text{ve}}}{2G_i(\zeta) \lambda_{i,g}} \quad (5.45)$$

5.4.4.2. Non-Linear Viscoelasticity

The non-linear viscoelasticity model was introduced to capture the non-linear time dependent behaviour exhibited by the epoxy resin that did not result in plastic strains, see Section 2.1.1. In this thesis an approach similar to that of Yu et al. [32] was followed, in which the viscoelastic stiffness is modified by a scalar function g . Similar to the linear viscoelasticity model, the long term elastic stiffness $E_\infty(\zeta)$ and bulk and shear viscoelastic moduli, $K_i(\zeta)$ and $G_i(\zeta)$ respectively, are degraded. However, for simplicity and to aid integration, these material parameters are expressed as functions of time, for example $\mathbf{D}_\infty(\zeta) \equiv \mathbf{D}_\infty(t)$, $K_i(\zeta) \equiv K_i(t)$ and $G_i(\zeta) \equiv G_i(t)$

Stress Formulation: The non-linear viscoelasticity model begins with a similar decomposition of the elastic stress into a long term component and a viscoelastic component:

$$\boldsymbol{\sigma}^e(t) = \mathbf{D}_\infty(t) \boldsymbol{\epsilon}^e(t) + \boldsymbol{\sigma}^{\text{ve}}(t) \quad (5.46)$$

where the viscoelastic stress is further decomposed into volumetric and deviatoric components:

$$\boldsymbol{\sigma}^{\text{ve}}(t) = p^{\text{ve}}(t) + \mathbf{S}^{\text{ve}}(t) \quad (5.47)$$

In this thesis, the strain based formulation used by Yu et al. has been modified to a stress based model, which can be more easily integrated into the current finite element framework. The development of viscoelastic stresses in the above equation are therefore based on a chain of Maxwell elements and are defined as:

$$p^{\text{ve}}(t) = \sum_{i=1}^N \int_0^t \exp\left(-\frac{t-\tau}{\lambda_{i,k}}\right) \frac{d}{d\tau} \left[\frac{K_i(t) \epsilon_v^e(t)}{g(\boldsymbol{\sigma}, \zeta, \epsilon_{\text{eq}}^p)} \right] d\tau \quad (5.48a)$$

$$\mathbf{S}^{\text{ve}}(t) = \sum_{i=1}^N \int_0^t \exp\left(-\frac{t-\tau}{\lambda_{i,g}}\right) \frac{d}{d\tau} \left[\frac{2G_i(t) \epsilon_d^e(t)}{g(\boldsymbol{\sigma}, \zeta, \epsilon_{\text{eq}}^p)} \right] d\tau \quad (5.48b)$$

In the above set of equations, the non-linearity is introduced through the function $g(\boldsymbol{\sigma}, \zeta, \epsilon_{\text{eq}}^p)$, which acts to reduce the viscoelastic stiffnesses and is further elaborated below. The integrals in Equations 5.48a and 5.48b act over the entire loading history $0 < \tau < t$ and thus are computationally undesirable. However, through mathematical manipulation, the expression for the viscoelastic stress can be made more suitable for computational purposes by storing the viscoelastic stress history from the previous time step and only computing the viscoelastic stress increment for the current time step. This results in an expression for the viscoelastic stress that takes the following form:

¹The classical definition of mechanical energy dissipation is $\Xi = \boldsymbol{\sigma} \dot{\boldsymbol{\epsilon}}$

$$\begin{aligned}\boldsymbol{\sigma}^{\text{ve}}(t) &= \boldsymbol{\sigma}^{\text{ve}}(t - \Delta t) + \Delta \boldsymbol{\sigma}^{\text{ve}} \\ &= (\boldsymbol{p}^{\text{ve}}(t - \Delta t) + \mathbf{S}^{\text{ve}}(t - \Delta t)) + (\Delta \boldsymbol{p}^{\text{ve}} + \Delta \mathbf{S}^{\text{ve}})\end{aligned}\quad (5.49)$$

where the stresses at time $t - \Delta t$ are known and the incremental volumetric and deviatoric viscoelastic stresses are given by the following expressions:

$$\Delta \boldsymbol{p}^{\text{ve}} = \sum_{i=1}^N \left[1 - \exp\left(-\frac{\Delta t}{\lambda_{i,k}}\right) \right] \left(\frac{K_i(t) \lambda_{i,k} \Delta \boldsymbol{\varepsilon}_v^e}{g(\boldsymbol{\sigma}, \zeta, \boldsymbol{\varepsilon}_{\text{eq}}^p) \Delta t} - \boldsymbol{p}_i^{\text{ve}}(t - \Delta t) \right) \quad (5.50a)$$

$$\Delta \mathbf{S}^{\text{ve}} = \sum_{i=1}^N \left[1 - \exp\left(-\frac{\Delta t}{\lambda_{i,g}}\right) \right] \left(\frac{2G_i(t) \lambda_{i,g} \Delta \boldsymbol{\varepsilon}_d^e}{g(\boldsymbol{\sigma}, \zeta, \boldsymbol{\varepsilon}_{\text{eq}}^p) \Delta t} - \mathbf{S}_i^{\text{ve}}(t - \Delta t) \right) \quad (5.50b)$$

The full mathematical derivation of this manipulation can be found in Appendix A. As a result, the stress in Equation 5.46 is computed as the sum of the elastic stress, the viscoelastic stress at the previous time step and the viscoelastic stress increment:

$$\boldsymbol{\sigma}^e(t) = \mathbf{D}_{\infty}(t) \boldsymbol{\varepsilon}^e(t) + \boldsymbol{\sigma}^{\text{ve}}(t - \Delta t) + \Delta \boldsymbol{\sigma}^{\text{ve}} \quad (5.51)$$

Tangent Stiffness: Similar to the linear viscoelasticity derivation, the total elastic stiffness is the sum of the instantaneous elastic stiffness and the viscoelastic stiffness:

$$\mathbf{D}^e(t) = \mathbf{D}_{\infty}(t) + \mathbf{D}^{\text{ve}}(t) \quad (5.52)$$

The expression for $\mathbf{D}^{\text{ve}}(t)$ is similar to Equation 5.43. However, the bulk and shear moduli are adjusted to include the non-linearity function g :

$$K^{\text{ve}}(t) = \frac{\partial \Delta \boldsymbol{p}^{\text{ve}}}{\partial \Delta \boldsymbol{\varepsilon}_v^e} = \sum_{i=1}^N \left[1 - \exp\left(-\frac{\Delta t}{\lambda_{i,k}}\right) \right] \left(\frac{K_i(t) \lambda_{i,k}}{g(\boldsymbol{\sigma}, \zeta, \boldsymbol{\varepsilon}_{\text{eq}}^p) \Delta t} \right) \quad (5.53a)$$

$$G^{\text{ve}}(t) = \frac{\partial \Delta \mathbf{S}^{\text{ve}}}{\partial \Delta \boldsymbol{\varepsilon}_d^e} = \sum_{i=1}^N \left[1 - \exp\left(-\frac{\Delta t}{\lambda_{i,g}}\right) \right] \left(\frac{G_i(t) \lambda_{i,g}}{g(\boldsymbol{\sigma}, \zeta, \boldsymbol{\varepsilon}_{\text{eq}}^p) \Delta t} \right) \quad (5.53b)$$

Viscoelastic Dissipation: The non-linear viscoelastic dissipation can be expressed as:

$$\Xi^{\text{ve}}(t) = g(\boldsymbol{\sigma}, \zeta, \boldsymbol{\varepsilon}_{\text{eq}}^p) \left[\sum_{i=1}^N \frac{(p_i^{\text{ve}})^2}{2K_i(t) \lambda_{i,k}} + \sum_{i=1}^N \frac{\mathbf{S}_i^{\text{ve}} \cdot \mathbf{S}_i^{\text{ve}}}{2G_i(t) \lambda_{i,g}} \right] \quad (5.54)$$

Non-Linearity Function: The function $g(\boldsymbol{\sigma}, \zeta, \boldsymbol{\varepsilon}_{\text{eq}}^p)$ introduces non-linearity into the viscoelastic model and is primarily a function of the current stress level $\boldsymbol{\sigma}$. This function also captures the effect the material state has on the onset of nonlinearity and the effect accumulated plastic strains have on viscoelasticity. This non-linearity function is a modified version of the proposed function in the work by Yu et al. [32] and Xia et al. [31]. In this thesis it is defined as:

$$g(\boldsymbol{\sigma}, \zeta, \boldsymbol{\varepsilon}_{\text{eq}}^p) = 1 + d_{\text{ve}} \left\langle f_{\text{ve}}(\boldsymbol{\sigma}, \zeta, \boldsymbol{\varepsilon}_{\text{eq}}^p) - 1 \right\rangle^{m_{\text{ve}}} \quad (5.55)$$

where d_{ve} and m_{ve} are material parameters. In this formulation the memory surface $\mathcal{R}(f)$ and the weight function ξ have been omitted to aid implementation. Xia et al. [31] introduced the memory function and the weight function to allow the model to capture the changing concavity of the hysteresis loop due to changes in material state and accumulated viscoplastic deformations. Without

these parameters, the non-linear viscoelastic model is still able to represent stress and plastic strain related softening, however the ability to model cyclic induced concavity changes is sacrificed as a result of this simplification. The function $f_{ve}(\boldsymbol{\sigma}, \zeta, \varepsilon_{eq}^p)$ can be seen as the yield surface for non-linear viscoelasticity and is defined as:

$$f_{ve}(\boldsymbol{\sigma}, \zeta, \varepsilon_{eq}^p) = \frac{\bar{\sigma}}{\sigma_0(\zeta, \varepsilon_{eq}^p)} \quad (5.56)$$

where $\bar{\sigma} = \sqrt{3J_2}$ is the von Mises equivalent stress and $\sigma_0(\zeta, \varepsilon_{eq}^p)$ defines the stress at which non-linearity begins. In order to account for the state of the material and plastic strains, $\sigma_0(\zeta, \varepsilon_{eq}^p)$ is written as the product of two functions:

$$\sigma_0(\zeta, \varepsilon_{eq}^p) = \phi_1(\zeta)\phi_2(\varepsilon_{eq}^p) \quad (5.57)$$

where:

$$\phi_1(\zeta) = (1 - \zeta)\sigma_0^{gla} + \zeta\sigma_0^{rub} \quad (5.58a)$$

$$\phi_2(\varepsilon_{eq}^p) = 1 - c_2 \exp(-c_3 \varepsilon_{eq}^p) \quad (5.58b)$$

where σ_0^{gla} and σ_0^{rub} relate to the stress at the onset of non-linearity for the glassy and rubbery states respectively, and c_2 and c_3 are material parameters controlling the effect the equivalent plastic strain has on non-linear viscoelasticity.

From Equation 5.55 it is apparent that non-linear viscoelasticity is only activated when the value of $f_{ve} > 1$. When the von Mises stress is below the threshold set by σ_0 , the non-linear function evaluates to $g = 1$ and the linear viscoelasticity model, as described in Section 5.4.4.1, is retrieved.

Because g is a function of the current stress state, an iterative procedure is required to compute the stresses when non-linear viscoelasticity is present, that is when $g > 1$. This procedure is described in detail in Section 5.4.6.

5.4.5. Viscoplasticity

The viscoplasticity model used in this thesis is based on the model used by Rocha et al. [24], extending it to incorporate material degradation in line with Section 5.4.3. In this section, the viscoplasticity model will be briefly described and the degraded material properties highlighted. In Section 5.4.6, the viscoplastic model will be slightly modified so that it can be used in conjunction with a non-linear viscoelasticity model.

As is the case for the non-linear viscoelasticity model, an iterative scheme is also required to compute the stress state when in the viscoplastic regime. The viscoplastic model starts with a trial stress that assumes the strain increment is purely viscoelastic:

$$\boldsymbol{\sigma}^{tr}(\zeta, t) = \mathbf{D}_{\infty}(\zeta) (\boldsymbol{\varepsilon}(t) - \boldsymbol{\varepsilon}^p(t - \Delta t)) + \mathbf{D}^{ve}(\zeta, \Delta t) (\boldsymbol{\varepsilon}(t) - \boldsymbol{\varepsilon}^p(t - \Delta t) - \boldsymbol{\varepsilon}^e(t - \Delta t)) + \boldsymbol{\sigma}^{ve}(t - \Delta t) \quad (5.59)$$

The yield surface f_p is pressure dependent and incorporates hardening by defining yield stresses which are functions of the equivalent plastic strain ε_{eq}^p :

$$f_p(\boldsymbol{\sigma}, \zeta, \varepsilon_{eq}^p) = 6J_2 + 2I_1 (\sigma_c(\zeta, \varepsilon_{eq}^p) - \sigma_t(\zeta, \varepsilon_{eq}^p)) - 2\sigma_c(\zeta, \varepsilon_{eq}^p)\sigma_t(\zeta, \varepsilon_{eq}^p) \quad (5.60a)$$

$$\Delta\varepsilon_{eq}^p = \sqrt{\frac{1}{1 + 2\nu_p^2} \Delta\boldsymbol{\varepsilon}^p \cdot \Delta\boldsymbol{\varepsilon}^p} \quad (5.60b)$$

where σ_c and σ_t are the compressive and tensile yield strengths respectively and ν_p is the plastic Poisson's ratio. Based on the trial stress, the yield function is evaluated and if $f_p \leq 0$, no further plastic strain develops and the computed trial stress is correct. However, if f_p evaluates to a value greater than zero, a plastic strain increment occurs in the current time step and the stresses must be corrected to account for plasticity. In this case, due to the viscous nature of this plasticity model, the development of plastic strains is delayed and the Kuhn-Tucker conditions are relaxed, allowing the yield function to obtain positive values. Rocha et al. [24] use a Perzyna type formulation defining the evolution of the plastic multiplier as:

$$\Delta\gamma = \begin{cases} \frac{\Delta t}{\eta_p} \left(\frac{f_p}{\sigma_t^0 \sigma_c^0} \right)^{m_p} & f_p > 0 \\ 0 & f_p \leq 0 \end{cases} \quad (5.61)$$

where η_p and m_p are the viscoplastic modulus and exponent respectively, and σ_c^0 and σ_t^0 are the compressive and tensile yield strengths evaluated at zero equivalent plastic strain. The updated stress and variation of plastic strain are then related to the plastic multiplier increment:

$$\boldsymbol{\sigma} = \frac{I_1^{\text{tr}}}{3\zeta_p} \boldsymbol{\delta}_{ij} + \frac{\mathbf{S}^{\text{tr}}}{\zeta_s} \quad (5.62a)$$

$$\Delta\boldsymbol{\epsilon}^p = \Delta\gamma \left(3\mathbf{S} + \frac{2}{9}\alpha I_1 \boldsymbol{\delta}_{ij} \right) \quad (5.62b)$$

where the plastic correction factors ζ_p and ζ_s , and the plastic flow direction α are defined as:

$$\zeta_p(\zeta, t) = 1 + 2(K_\infty(\zeta) + K_{ve}(\zeta, t)) \alpha \Delta\gamma = 1 + 2\widehat{K}(\zeta, t) \alpha \Delta\gamma \quad (5.63a)$$

$$\zeta_s(\zeta, t) = 1 + 6(G_\infty(\zeta) + G_{ve}(\zeta, t)) \Delta\gamma = 1 + 6\widehat{G}(\zeta, t) \Delta\gamma \quad (5.63b)$$

$$\alpha = \frac{9}{2} \frac{1 - 2\nu_p}{1 + \nu_p} \quad (5.63c)$$

Rocha et al. [24] show that Equation 5.61 is a function of $\Delta\gamma$ only and thus can be solved iteratively using the Newton-Raphson method. The function to be solved is:

$$\Phi(\Delta\gamma) = \frac{\Delta\gamma \Delta t}{\eta_p} \left(\frac{f_p}{\sigma_t^0 \sigma_c^0} \right)^{m_p} - \Delta\gamma = 0 \quad (5.64)$$

For quadratic convergence of the Newton-Raphson method, the derivative of the above equation must be computed. The computation of this derivative is presented as derivative number four in Section 5.4.6.3.

Once the value for the plastic multiplier increment has been determined, all that remains is to compute to the consistent tangent stiffness matrix. The derivation of this matrix is given in Appendix A.

It is clear from experimental observations that the yield strength of an epoxy resin is highly dependent on the state of the material. As a result, this viscoplastic model incorporates material degradation by setting the yield strengths of the material to be a function of the degree of glass transition ζ . The degradation relationships are defined in Box 5.4.2.

Box 5.4.2: Degradation of Viscoplasticity Parameters

The tensile and compressive yield strengths are provided as functions of the equivalent plastic strain for both the glassy and rubbery state. The yield strengths used in the evaluation of the viscoplastic model are dependent on the state of the material and take the same form as the degradation model described by Equation 5.33:

$$\sigma_t(\zeta, \varepsilon_{eq}^p) = (1 - \zeta)\sigma_t^{gla}(\varepsilon_{eq}^p) + \zeta\sigma_t^{rub}(\varepsilon_{eq}^p) \quad (5.65a)$$

$$\sigma_c(\zeta, \varepsilon_{eq}^p) = (1 - \zeta)\sigma_c^{gla}(\varepsilon_{eq}^p) + \zeta\sigma_c^{rub}(\varepsilon_{eq}^p) \quad (5.65b)$$

The derivative of the yield strength with respect to the equivalent plastic strain is required in the computation of both the Jacobian of the iterative method and the consistent tangent stiffness matrix. The degraded derivative can be calculated from the above equations:

$$\frac{\partial \sigma_t(\zeta, \varepsilon_{eq}^p)}{\partial \varepsilon_{eq}^p} = (1 - \zeta) \frac{\partial \sigma_t^{gla}(\varepsilon_{eq}^p)}{\partial \varepsilon_{eq}^p} + \zeta \frac{\partial \sigma_t^{rub}(\varepsilon_{eq}^p)}{\partial \varepsilon_{eq}^p} \quad (5.66a)$$

$$\frac{\partial \sigma_c(\zeta, \varepsilon_{eq}^p)}{\partial \varepsilon_{eq}^p} = (1 - \zeta) \frac{\partial \sigma_c^{gla}(\varepsilon_{eq}^p)}{\partial \varepsilon_{eq}^p} + \zeta \frac{\partial \sigma_c^{rub}(\varepsilon_{eq}^p)}{\partial \varepsilon_{eq}^p} \quad (5.66b)$$

Once the plastic strain and the stress level have been determined, the total viscoplastic dissipation for the current time increment can be calculated by:

$$\Xi^{vp} = \boldsymbol{\sigma} \cdot \Delta \boldsymbol{\varepsilon}^p \quad (5.67)$$

5.4.6. Coupled Non-Linear Viscoelasticity and Viscoplasticity

Constitutive Model 2, as outlined in Section 5.4.1, incorporates both the non-linear viscoelasticity model and the plasticity model. Because both of these models are dependent on the current stress state and the degree of plastic strain, a return mapping that incorporates both of these models must be performed. In this section the formulation of the coupled return mapping algorithm is outlined and the implementation of the iterative algorithm is explained in further detail.

5.4.6.1. Overview of the Algorithm

To give an overview of the return mapping algorithm, the problem description and given variables are outlined. Before entering the return mapping algorithm the following parameters are given and remain constant:

- (a) $\boldsymbol{\varepsilon}(t)$ & $\Delta \boldsymbol{\varepsilon}$ - the total strain vector and total strain increment for the current time step.
- (b) $\boldsymbol{\varepsilon}^p(t - \Delta t)$ & $\varepsilon_{eq}^p(t - \Delta t)$ - the plastic strain vector and equivalent plastic strain for the previous time step.
- (c) $\mathbf{D}_\infty(t)$ - the long term stiffness matrix for the current time step.
- (d) $\Lambda \boldsymbol{\sigma}^{ve}(t - \Delta t)$ - the decayed viscoelastic stress vector from the previous time step, defined below.
- (e) $\zeta(t)$ - the degree of glass transition for the current time step.

The goal of the return mapping algorithm is to solve for the two unknown scalar parameters that define the influence of each viscous model on the stress state:

- (i) g - the degree of non-linear viscoelasticity, $g \geq 1$.
- (ii) $\Delta\gamma$ - the increment of the plastic multiplier, $\Delta\gamma \geq 0$.

Both of the unknown parameters in the return mapping algorithm can be cast into two functions that can be solved iteratively to determine the current values of g and $\Delta\gamma$. These functions are given below as a coupled set of equations:

$$\Gamma(g, \Delta\gamma) = 1 + d_{ve} (f_{ve}(\boldsymbol{\sigma}, \zeta, \varepsilon_{eq}^p) - 1)^{m_{ve}} - g = 0 \quad (5.68a)$$

$$\Phi(g, \Delta\gamma) = \frac{\Delta t}{\eta_p} \left(\frac{f_p(\boldsymbol{\sigma}, \varepsilon_{eq}^p)}{\sigma_t^0 \sigma_c^0} \right)^{m_p} - \Delta\gamma = 0 \quad (5.68b)$$

where $\boldsymbol{\sigma}$ and ε_{eq}^p are a function of both g and $\Delta\gamma$. Note that Equation 5.68b is identical to Equation 5.64. However, because f_p is a function of the current stress $\boldsymbol{\sigma}$, Φ is now also a function of g . The Newton-Raphson algorithm can be applied to the above functions to iteratively solve for the two unknown coupled variables at integration point level [7]:

$$\begin{bmatrix} g^{k+1} \\ \Delta\gamma^{k+1} \end{bmatrix} = \begin{bmatrix} g^k \\ \Delta\gamma^k \end{bmatrix} - \begin{bmatrix} \frac{\partial \Gamma}{\partial g} & \frac{\partial \Gamma}{\partial \Delta\gamma} \\ \frac{\partial \Phi}{\partial g} & \frac{\partial \Phi}{\partial \Delta\gamma} \end{bmatrix}^{-1} \begin{bmatrix} \Gamma(g^k, \Delta\gamma^k) \\ \Phi(g^k, \Delta\gamma^k) \end{bmatrix} \quad (5.69)$$

The determination of the Jacobian matrix (the 2 x 2 matrix in the above equation) is central to the Newton-Raphson scheme and in the context of this coupled return mapping algorithm, greatly improves convergence speed. Each term in this matrix is derived in Section 5.4.6.3.

5.4.6.2. Detailed Procedure of the Return Mapping Algorithm

In this section, the iterative method for the coupled return mapping algorithm is described in detail and, for clarity, is summarised in Box B.2.

An approach similar to the return mapping scheme used for viscoplasticity is used for this algorithm, in which a trial stress is computed and later corrected based on the amount of plastic strain. However, the introduction of a non-linear viscoelasticity model necessitates a key departure from the procedure used by Rocha et al. Because the viscoelastic stiffness is constantly changing due to variations in g , the trial stress must be recomputed at the beginning of each iteration within this return mapping algorithm. Furthermore, as g is a function of the current amount of plastic strain, the various strains must also be recomputed before each iteration.

In this model, there are three possible outcomes from the combination of non-linear viscoelasticity and viscoplasticity:

1. Linear viscoelasticity with no viscoplasticity, i.e. $g = 1$ and $\Delta\gamma = 0 \Rightarrow$ No return mapping algorithm required.
2. Non-linear viscoelasticity with no viscoplasticity, i.e. $g > 1$ and $\Delta\gamma = 0 \Rightarrow$ Solve single variable return mapping algorithm for g .
3. Non-linear viscoelasticity with viscoplasticity, i.e. $g > 1$ and $\Delta\gamma > 0 \Rightarrow$ Solve coupled return mapping algorithm for g and $\Delta\gamma$.

The fourth option of linear viscoelasticity with viscoplasticity is excluded based on the assumption that non-linear viscoelasticity occurs before the onset of plasticity. This assumption is consistent with the observed material behaviour detailed in Section 2.1.1, in which softening of the stress-strain response occurred before the development of plastic strains.

The algorithm begins with the assumption that there is no further plastic strain and that the stiffness of the non-linear viscoelasticity is unchanged, that is $g(t) = g(t - \Delta t)$ and $\Delta\gamma = 0$. Based on this assumption the degree of elastic and plastic strain can be computed. As the algorithm proceeds, the stresses are updated based on the changing strain state until convergence is achieved.

Strain Update: At the beginning of the algorithm and at the end of each iteration, the elastic and plastic strain vectors are updated based on the amount of plasticity developed in the current iteration. The strains are updated as follows:

$$\Delta\boldsymbol{\varepsilon}^P = \Delta\gamma \left(3\mathbf{S} + \frac{2}{9}\alpha I_1 \delta_{ij} \right) \quad (5.70a)$$

$$\boldsymbol{\varepsilon}^P(t) = \boldsymbol{\varepsilon}^P(t - \Delta t) + \Delta\boldsymbol{\varepsilon}^P \quad (5.70b)$$

$$\Delta\boldsymbol{\varepsilon}_{\text{eq}}^P = \sqrt{\frac{1}{1 + 2\nu_p^2} \Delta\boldsymbol{\varepsilon}^P \cdot \Delta\boldsymbol{\varepsilon}^P} \quad (5.70c)$$

$$\boldsymbol{\varepsilon}_{\text{eq}}^P(t) = \boldsymbol{\varepsilon}_{\text{eq}}^P(t - \Delta t) + \Delta\boldsymbol{\varepsilon}_{\text{eq}}^P \quad (5.70d)$$

$$\boldsymbol{\varepsilon}^e(t) = \boldsymbol{\varepsilon}(t) - \boldsymbol{\varepsilon}^P(t) \quad (5.70e)$$

$$\Delta\boldsymbol{\varepsilon}^e = \Delta\boldsymbol{\varepsilon} - \Delta\boldsymbol{\varepsilon}^P \quad (5.70f)$$

Trial Stress Update: Once the strains have been updated, the new trial stress can be computed. The trial stress consists of the long term elastic stress, the decayed viscoelastic stress from the previous time step and the new viscoelastic stress increment. From Equation 5.51, the trial stress can be written as:

$$\boldsymbol{\sigma}^{\text{tr}}(t) = \mathbf{D}_{\infty}(t)\boldsymbol{\varepsilon}^e(t) + \boldsymbol{\sigma}^{\text{ve}}(t - \Delta t) + \Delta\boldsymbol{\sigma}^{\text{ve}}$$

where the viscoelastic stress increments are given in Equations 5.50a and 5.50b as:

$$\Delta p^{\text{ve}} = \sum_{i=1}^N \left[1 - \exp\left(-\frac{\Delta t}{\lambda_{i,k}}\right) \right] \left(\frac{K_i(t)\lambda_{i,k}\Delta\boldsymbol{\varepsilon}_v^e}{g(\boldsymbol{\sigma}, \zeta, \boldsymbol{\varepsilon}_{\text{eq}}^P)\Delta t} - p_i^{\text{ve}}(t - \Delta t) \right)$$

$$\Delta \mathbf{S}^{\text{ve}} = \sum_{i=1}^N \left[1 - \exp\left(-\frac{\Delta t}{\lambda_{i,g}}\right) \right] \left(\frac{2G_i(t)\lambda_{i,g}\Delta\boldsymbol{\varepsilon}_d^e}{g(\boldsymbol{\sigma}, \zeta, \boldsymbol{\varepsilon}_{\text{eq}}^P)\Delta t} - \mathbf{S}_i^{\text{ve}}(t - \Delta t) \right)$$

The last terms in the above equations represent the exponential decaying of the viscoelastic stresses from the previous time step $t - \Delta t$. It is possible to rearrange the expression for the trial stress and redefine the viscoelastic stress increments such that this known decay of the previous viscoelastic stress is no longer part of the stress increment. The new trial stress is defined as:

$$\boldsymbol{\sigma}^{\text{tr}}(t) = \mathbf{D}_{\infty}(t)\boldsymbol{\varepsilon}^e(t) + \Lambda\boldsymbol{\sigma}^{\text{ve}}(t - \Delta t) + \Delta\boldsymbol{\sigma}^{\text{ve}} \quad (5.71)$$

where the decayed viscoelastic stress from the previous time step $\Lambda\boldsymbol{\sigma}^{\text{ve}}(t - \Delta t)$ is equal to:

$$\Lambda\boldsymbol{\sigma}^{\text{ve}}(t - \Delta t) = \sum_{i=1}^N \exp\left(-\frac{\Delta t}{\lambda_{i,k}}\right) p_i^{\text{ve}}(t - \Delta t)\delta_{ij} + \sum_{i=1}^N \exp\left(-\frac{\Delta t}{\lambda_{i,g}}\right) \mathbf{S}_i^{\text{ve}}(t - \Delta t) \quad (5.72)$$

and the viscoelastic stress update $\Delta\boldsymbol{\sigma}^{\text{ve}} = \Delta p^{\text{ve}} + \Delta\mathbf{S}^{\text{ve}}$ is redefined with:

$$\Delta p^{\text{ve}} = \sum_{i=1}^N \left[1 - \exp\left(-\frac{\Delta t}{\lambda_{i,k}}\right) \right] \frac{K_i(t)\lambda_{i,k}\Delta\boldsymbol{\varepsilon}_v^e}{g(\boldsymbol{\sigma}, \zeta, \boldsymbol{\varepsilon}_{\text{eq}}^p)\Delta t} \quad (5.73a)$$

$$\Delta\mathbf{S}^{\text{ve}} = \sum_{i=1}^N \left[1 - \exp\left(-\frac{\Delta t}{\lambda_{i,g}}\right) \right] \frac{2G_i(t)\lambda_{i,g}\Delta\boldsymbol{\varepsilon}_d^e}{g(\boldsymbol{\sigma}, \zeta, \boldsymbol{\varepsilon}_{\text{eq}}^p)\Delta t} \quad (5.73b)$$

As a result, for a given iteration, the trial stress becomes the sum of two constant elastic terms and a viscoelastic stress increment. Only the viscoelastic stress increment, a function of g , varies within the return mapping algorithm:

$$\boldsymbol{\sigma}^{\text{tr}}(g) = \mathbf{D}_{\infty}(t)\boldsymbol{\varepsilon}^e(t) + \Lambda\boldsymbol{\sigma}^{\text{ve}}(t - \Delta t) + \Delta\boldsymbol{\sigma}^{\text{ve}}(g) \quad (5.74)$$

From this trial stress, the first invariant of the trial stress $I_1^{\text{tr}}(g)$, the deviatoric trial stress vector $\mathbf{S}^{\text{tr}}(g)$ and the second invariant of the deviatoric trial stress vector $J_2^{\text{tr}}(g)$ can be computed.

Current Stress Update: Based on the current value of $\Delta\gamma$, the values for the trial stress correction factors ζ_p and ζ_s can be computed from Equations 5.63a and 5.63b respectively. Because these correction factors depend on the viscoelastic stiffness and the amount of plastic strain, they are functions of both g and $\Delta\gamma$. Using the previously computed trial stress, the current stress vector can be computed:

$$\boldsymbol{\sigma}(g, \Delta\gamma) = \frac{I_1^{\text{tr}}(g)}{3\zeta_p(g, \Delta\gamma)}\delta_{ij} + \frac{\mathbf{S}^{\text{tr}}(g)}{\zeta_s(g, \Delta\gamma)} \quad (5.75)$$

From this stress, the first invariant of the current stress $I_1(g, \Delta\gamma)$, the deviatoric stress vector $\mathbf{S}(g, \Delta\gamma)$ and the second invariant of the deviatoric stress vector $J_2(g, \Delta\gamma)$ can be computed.

g & $\Delta\gamma$ Update: To determine whether the iterative scheme has converged, Equations 5.68a and 5.68b are checked against prescribed tolerances. Convergence is satisfied if the following is true:

$$|\Gamma(t)| \leq \Gamma_{tol} \wedge |\Phi(t)| \leq \Phi_{tol} \quad (5.76)$$

If the above inequalities are not satisfied, both g and $\Delta\gamma$ are updated based on Equation 5.69 and the iterative process continues until the above equation is satisfied. Box B.2 in Appendix B presents the detailed pseudocode for the coupled non-linear viscoelastic and viscoplastic return mapping algorithm.

5.4.6.3. Calculation of the Jacobian Matrix:

In order to utilise the fast convergence of the Newton-Raphson method, the Jacobian matrix, which contains the partial derivatives of each function in Equation 5.69, must be determined.

First, the derivatives of the stress invariants I_1 and J_2 are determined with respect to both g and $\Delta\gamma$. Both I_1 and J_2 can be written as a function of their trial stress counterparts, I_1^{tr} and J_2^{tr} :

$$I_1(g, \Delta\gamma) = \frac{I_1^{\text{tr}}(g)}{\zeta_p(g, \Delta\gamma)} \quad (5.77a)$$

$$J_2(g, \Delta\gamma) = \frac{J_2^{\text{tr}}(g)}{\zeta_s(g, \Delta\gamma)^2} \quad (5.77b)$$

Taking the derivatives of the above equations gives:

$$\frac{\partial I_1(g, \Delta\gamma)}{\partial g} = \frac{1}{\zeta_p(g, \Delta\gamma)^2} \left(\frac{\partial I_1^{\text{tr}}(g)}{\partial g} \zeta_p(g, \Delta\gamma) - \frac{\partial \zeta_p(g, \Delta\gamma)}{\partial g} I_1^{\text{tr}}(g) \right) \quad (5.78a)$$

$$\frac{\partial I_1(g, \Delta\gamma)}{\partial \Delta\gamma} = -\frac{I_1^{\text{tr}}(g)}{\zeta_p(g, \Delta\gamma)^2} \frac{\partial \zeta_p(g, \Delta\gamma)}{\partial \Delta\gamma} \quad (5.78b)$$

$$\frac{\partial J_2(g, \Delta\gamma)}{\partial g} = \frac{1}{\zeta_s(g, \Delta\gamma)^4} \left(\frac{\partial J_2^{\text{tr}}(g)}{\partial g} \zeta_s(g, \Delta\gamma)^2 - 2 \frac{\partial \zeta_s(g, \Delta\gamma)}{\partial g} J_2^{\text{tr}}(g) \zeta_s(g, \Delta\gamma) \right) \quad (5.78c)$$

$$\frac{\partial J_2(g, \Delta\gamma)}{\partial \Delta\gamma} = -2 \frac{J_2^{\text{tr}}(g)}{\zeta_s(g, \Delta\gamma)^3} \frac{\partial \zeta_s(g, \Delta\gamma)}{\partial \Delta\gamma} \quad (5.78d)$$

The derivatives that remain in the above equations are determined in Appendix A. It should also be noted that the variation of the equivalent plastic strain is a function of both g and $\Delta\gamma$, necessitating its derivative to be taken with respect to both parameters. Rocha et al. [24] present the expression for the change in equivalent plastic strain as a function of the trial stresses:

$$\Delta \varepsilon_{\text{eq}}^p(g, \Delta\gamma) = \Delta\gamma \sqrt{\frac{\frac{18}{\zeta_s(g, \Delta\gamma)^2} J_2^{\text{tr}}(g) + \frac{4\alpha^2}{27\zeta_p(g, \Delta\gamma)^2} I_1^{\text{tr}}(g)^2}{1 + 2\nu_p^2}} = \Delta\gamma \sqrt{\frac{\widehat{A}(g, \Delta\gamma)}{1 + 2\nu_p^2}} \quad (5.79)$$

Therefore, its derivative with respect to both g and $\Delta\gamma$ can be determined:

$$\frac{\partial \Delta \varepsilon_{\text{eq}}^p(g, \Delta\gamma)}{\partial g} = \frac{\Delta\gamma}{2\sqrt{1 + 2\nu_p^2} \sqrt{\widehat{A}(g, \Delta\gamma)}} \frac{\partial \widehat{A}(g, \Delta\gamma)}{\partial g} \quad (5.80a)$$

$$\frac{\partial \Delta \varepsilon_{\text{eq}}^p(g, \Delta\gamma)}{\partial \Delta\gamma} = \sqrt{\frac{1}{1 + 2\nu_p^2}} \left[\sqrt{\widehat{A}(g, \Delta\gamma)} - \frac{\Delta\gamma}{2\sqrt{\widehat{A}(g, \Delta\gamma)}} \left(\frac{216\widehat{G}(g)J_2^{\text{tr}}(g)}{\zeta_s(g, \Delta\gamma)^3} + \frac{16\alpha^3\widehat{K}(g)I_1^{\text{tr}}(g)^2}{27\zeta_p(g, \Delta\gamma)^3} \right) \right] \quad (5.80b)$$

The full derivations of the above equations and the derivative of $\widehat{A}(g, \Delta\gamma)$ with respect to g can be found in Appendix A. The derivatives of each term in the Jacobian matrix are derived below.

Derivative 1 - $\frac{\partial \Gamma}{\partial g}$: Starting with Equation 5.68a, the derivative with respect to g is taken:

$$\frac{\partial \Gamma}{\partial g} = m_{\text{ve}} d_{\text{ve}} (f_{\text{ve}}(\boldsymbol{\sigma}, \zeta, \varepsilon_{\text{eq}}^p) - 1)^{m_{\text{ve}} - 1} \frac{\partial f_{\text{ve}}(g, \Delta\gamma)}{\partial g} - 1 \quad (5.81)$$

The derivative of f_{ve} with respect to g can be written as:

$$\frac{\partial f_{\text{ve}}(g, \Delta\gamma)}{\partial g} = \frac{\sqrt{3}}{\sigma_0(\varepsilon_{\text{eq}}^p)^2} \left(\frac{\partial(\sqrt{J_2}(g, \Delta\gamma))}{\partial g} \sigma_0(\varepsilon_{\text{eq}}^p) - \frac{\partial \sigma_0(\varepsilon_{\text{eq}}^p)}{\partial g} \sqrt{J_2}(g, \Delta\gamma) \right) \quad (5.82)$$

Using the chain rule, the derivative of the square root of J_2 with respect to g can be determined:

$$\frac{\partial(\sqrt{J_2}(g, \Delta\gamma))}{\partial g} = \frac{1}{2\sqrt{J_2}(g, \Delta\gamma)} \frac{\partial J_2(g, \Delta\gamma)}{\partial g} \quad (5.83)$$

where the derivative of J_2 with respect to g is given in Equation 5.78c. Now, the derivative of σ_0 with respect to g is elaborated:

$$\frac{\partial \sigma_0(\varepsilon_{\text{eq}}^{\text{p}})}{\partial g} = \frac{\partial \sigma_0(\varepsilon_{\text{eq}}^{\text{p}})}{\partial \varepsilon_{\text{eq}}^{\text{p}}} \frac{\partial \Delta \varepsilon_{\text{eq}}^{\text{p}}(g, \Delta \gamma)}{\partial g} \quad (5.84)$$

The first term in the above equation is equal to:

$$\frac{\partial \sigma_0(\varepsilon_{\text{eq}}^{\text{p}})}{\partial \varepsilon_{\text{eq}}^{\text{p}}} = \phi_1 c_2 c_3 \exp(-c_3 \varepsilon_{\text{eq}}^{\text{p}}) \quad (5.85)$$

and the second term has been previously derived in Equation 5.80a.

Derivative 2 - $\frac{\partial \Gamma}{\partial \Delta \gamma}$: Starting with Equation 5.68a, the derivative with respect to $\Delta \gamma$ is taken:

$$\frac{\partial \Gamma}{\partial \Delta \gamma} = m_{\text{ve}} d_{\text{ve}} (f(\boldsymbol{\sigma}, \zeta, \varepsilon_{\text{eq}}^{\text{p}}) - 1)^{m_{\text{ve}} - 1} \frac{\partial f_{\text{ve}}(g, \Delta \gamma)}{\partial \Delta \gamma} \quad (5.86)$$

The derivative of f_{ve} with respect to $\Delta \gamma$ can be written as:

$$\frac{\partial f_{\text{ve}}(g, \Delta \gamma)}{\partial \Delta \gamma} = \frac{\sqrt{3}}{\sigma_0(\varepsilon_{\text{eq}}^{\text{p}})^2} \left(\frac{\partial (\sqrt{J_2}(g, \Delta \gamma)})}{\partial \Delta \gamma} \sigma_0(\varepsilon_{\text{eq}}^{\text{p}}) - \frac{\partial \sigma_0(\varepsilon_{\text{eq}}^{\text{p}})}{\partial \Delta \gamma} \sqrt{J_2}(g, \Delta \gamma) \right) \quad (5.87)$$

Using the chain rule, the derivative of the square root of J_2 with respect to $\Delta \gamma$ can be determined:

$$\frac{\partial (\sqrt{J_2}(g, \Delta \gamma))}{\partial \Delta \gamma} = \frac{1}{2\sqrt{J_2}(g, \Delta \gamma)} \frac{\partial J_2(g, \Delta \gamma)}{\partial \Delta \gamma} \quad (5.88)$$

where the derivative of J_2 with respect to $\Delta \gamma$ is given in Equation 5.78d. Now, the derivative of σ_0 with respect to $\Delta \gamma$ is elaborated:

$$\frac{\partial \sigma_0(\varepsilon_{\text{eq}}^{\text{p}})}{\partial \Delta \gamma} = \frac{\partial \sigma_0(\varepsilon_{\text{eq}}^{\text{p}})}{\partial \varepsilon_{\text{eq}}^{\text{p}}} \frac{\partial \Delta \varepsilon_{\text{eq}}^{\text{p}}(g, \Delta \gamma)}{\partial \Delta \gamma} \quad (5.89)$$

The first term in the above equation is given in Equation 5.85 and the second term has been previously derived in Equation 5.80b.

Derivative 3 - $\frac{\partial \Phi}{\partial g}$: Starting with Equation 5.68b, the derivative with respect to g is taken:

$$\frac{\partial \Phi}{\partial g} = \frac{m_{\text{p}} \Delta t}{\eta_{\text{p}} \sigma_{\text{t}}^0 \sigma_{\text{c}}^0} \left(\frac{f_{\text{p}}(g, \Delta \gamma)}{\sigma_{\text{t}}^0 \sigma_{\text{c}}^0} \right)^{m_{\text{p}} - 1} \frac{\partial f_{\text{p}}(g, \Delta \gamma)}{\partial g} \quad (5.90)$$

The derivative of the yield function f_{p} with respect to g can be written as:

$$\frac{\partial f_{\text{p}}(g, \Delta \gamma)}{\partial g} = 6 \frac{\partial J_2(g, \Delta \gamma)}{\partial g} + 2 \frac{\partial I_1(g, \Delta \gamma)}{\partial g} (\sigma_{\text{c}}(\varepsilon_{\text{eq}}^{\text{p}}) - \sigma_{\text{t}}(\varepsilon_{\text{eq}}^{\text{p}})) + \frac{\partial f_{\text{p}}(g, \Delta \gamma)}{\partial \varepsilon_{\text{eq}}^{\text{p}}} \frac{\partial \Delta \varepsilon_{\text{eq}}^{\text{p}}(g, \Delta \gamma)}{\partial g} \quad (5.91)$$

In the above equation, the derivative of f_{p} with respect to $\varepsilon_{\text{eq}}^{\text{p}}$ is:

$$\frac{\partial f_{\text{p}}(g, \Delta \gamma)}{\partial \varepsilon_{\text{eq}}^{\text{p}}} = 2I_1(g, \Delta \gamma) (H_{\text{c}}(\varepsilon_{\text{eq}}^{\text{p}}) - H_{\text{t}}(\varepsilon_{\text{eq}}^{\text{p}})) - 2(\sigma_{\text{c}}(\varepsilon_{\text{eq}}^{\text{p}}) H_{\text{t}}(\varepsilon_{\text{eq}}^{\text{p}}) + \sigma_{\text{t}}(\varepsilon_{\text{eq}}^{\text{p}}) H_{\text{c}}(\varepsilon_{\text{eq}}^{\text{p}})) \quad (5.92)$$

where $H_{\text{c}}(\varepsilon_{\text{eq}}^{\text{p}})$ and $H_{\text{t}}(\varepsilon_{\text{eq}}^{\text{p}})$ are the derivatives of $\sigma_{\text{c}}(\varepsilon_{\text{eq}}^{\text{p}})$ and $\sigma_{\text{t}}(\varepsilon_{\text{eq}}^{\text{p}})$ with respect to $\varepsilon_{\text{eq}}^{\text{p}}$. These derivatives represents the compressive and tensile hardening moduli respectively. The last term in Equation 5.91 has been previously derived in Equation 5.80a.

Derivative 4 - $\frac{\partial \Phi}{\partial \Delta \gamma}$: Starting with Equation 5.68b, the derivative with respect to $\Delta \gamma$ is taken:

$$\frac{\partial \Phi}{\partial \Delta \gamma} = \frac{m_p \Delta t}{\eta_p \sigma_t^0 \sigma_c^0} \left(\frac{f_p(g, \Delta \gamma)}{\sigma_t^0 \sigma_c^0} \right)^{m_p - 1} \frac{\partial f_p(g, \Delta \gamma)}{\partial \Delta \gamma} - 1 \quad (5.93)$$

The derivative of the yield function f_p with respect to $\Delta \gamma$ can be written as:

$$\frac{\partial f_p(g, \Delta \gamma)}{\partial \Delta \gamma} = 6 \frac{\partial J_2(g, \Delta \gamma)}{\partial \Delta \gamma} + 2 \frac{\partial I_1(g, \Delta \gamma)}{\partial \Delta \gamma} (\sigma_c(\varepsilon_{eq}^p) - \sigma_t(\varepsilon_{eq}^p)) + \frac{\partial f_p(g, \Delta \gamma)}{\partial \varepsilon_{eq}^p} \frac{\partial \Delta \varepsilon_{eq}^p(g, \Delta \gamma)}{\partial \Delta \gamma} \quad (5.94)$$

where the derivative of f_p with respect to ε_{eq}^p is given in Equation 5.92 and the derivative of $\Delta \varepsilon_{eq}^p$ with respect to $\Delta \gamma$ has been previously derived in Equation 5.80b.

5.5. Multiphysics Framework

This section focuses on how the above models are brought together in the multiphysics framework. As discussed in Section 5.1, the physical models are solved in an uncoupled one-way manner, with the heat model solved first, followed by the diffusion model and then the mechanics model. For typical multiphysics analyses the transport timescales would be larger than required for the mechanics model. However, in this thesis the same time scale is used to solve all three models for simplicity of implementation.

As outlined in Figure 5.1, the dissipation field from the previous time step is used as a heat input for the current time step. Because solving the viscous mechanical models requires a relatively small time step when compared to the heat model, the effect of uncoupling the mechanical dissipation from the current time step is negligible. As a result, a strong coupling does not exist for this multiphysics problem, allowing the operator split method to be utilised.

In the proceeding sections the multiphysics aspects related to each physical model are described in detail.

5.5.1. Heat Model

Mechanical viscoelastic and viscoplastic dissipation from the previous time step is used to model internal heat generation. It is thus hypothesised that the mechanical energy generated by viscous effects is dissipated through heat energy alone. The viscoelastic and viscoplastic dissipations are computed in the mechanics model using Equations 5.45, 5.54 and 5.67. This dissipation is computed at each integration point and has a unit of $N / (m^2 \cdot s)$. This is equivalent to $J / (m^3 \cdot s)$, which is the required unit for Q_{int} in Equation 5.14. The right hand side vector for the heat model is then computed by evaluating the integral in Equation 5.14.

Finally, the temperature field is evaluated for the current time step by solving Equation 5.13 subject to the imposed boundary conditions.

5.5.2. Diffusion Model

The next step of the multiphysics coupling involves passing the computed temperature field to the diffusion model. This temperature field is used to evaluate the temperature dependent diffusivity matrix in Equation 5.20. The moisture field is then evaluated for the current time step by solving Equation 5.20, subject to the imposed boundary conditions.

5.5.3. Mechanics Model

The final step in the multiphysics solver involves passing the temperature and moisture fields to the mechanics model. These fields are used to compute glass transition, material degradation, thermal expansion and moisture swelling.

At every integration point in the mechanics model, the degree of glass transition ζ is calculated from Equation 5.31. The subsequent degradation factors are then applied to each material model as described in Section 5.4.

In order to account for the expansion of the epoxy resin due to changes in temperature and moisture content, expansion and swelling strains are subtracted from the total strain vector \mathcal{E} at the start of the time step. The mechanical strain $\boldsymbol{\varepsilon}$ used in the mechanics model is computed as:

$$\boldsymbol{\varepsilon} = \mathcal{E} - \boldsymbol{\varepsilon}_T - \boldsymbol{\varepsilon}_\omega \quad (5.95)$$

where $\boldsymbol{\varepsilon}_T$ and $\boldsymbol{\varepsilon}_\omega$ are the thermal expansion and moisture swelling strains respectively and are given by:

$$\boldsymbol{\varepsilon}_T = \alpha_T (T - T_{\text{init}}) \quad (5.96a)$$

$$\boldsymbol{\varepsilon}_\omega = \alpha_\omega \omega \quad (5.96b)$$

where α_T is the coefficient of thermal expansion, T_{init} is the initial temperature of the material and α_ω is the coefficient of moisture expansion.

6

Results

In this thesis numerical analyses were performed using a finite element implementation of the constitutive models, as described in Section 5. An overview of the implementation of the material models can be found in Appendix B. The numerical analyses were performed to validate the constitutive models and demonstrate the ability of the models to capture the multiphysical and time-dependent behaviour of epoxy resins.

6.1. Validation of the Transport Model

Two numerical studies were performed on the transport model in order to verify its implementation. Both analyses were performed with varying levels of mesh refinement and the results were compared to both a reference solution as well as a commercial finite element solver, Strand7. Both studies were taken from the Strand7 verification manual [27].

6.1.1. Steady State Analysis

In this steady state analysis a 2D heat transfer problem was modelled with both a fixed temperature and convective boundary conditions. Figure 6.1 describes the problem, in which a fixed temperature of 100°C was prescribed to edge AB and edge DA was insulated with zero heat flux. Both edges BC and CD were subjected to a convective boundary condition with an ambient fluid temperature equal to 0°C . The material properties and mesh details are given in Table 6.1. Note that by setting $\rho = c = 0$, a steady state scheme was obtained in the heat model as the \dot{T} term vanished. The reference solution, as provided by ‘*Selected FE Benchmarks in Structural and Thermal Analysis*’ (NAFEMS, 1987), is a steady state temperature of 18.3°C at point E.

Input	Properties
<i>Material Properties</i>	$\kappa = 52.0 \text{ J} / (\text{s} \cdot \text{m} \cdot \text{K}); h = 750.0 \text{ J} / (\text{s} \cdot \text{m}^2 \cdot \text{K})$ $\rho = c = 0.0; T_f = T_{\text{init}} = 0.0^{\circ}\text{C}$
<i>Mesh Density</i>	Coarse mesh: 0.2 m x 0.2 m Medium mesh: 0.1 m x 0.1 m Fine mesh: 0.025 m x 0.025 m

Table 6.1: Input for the steady state heat analysis.

Table 6.2 presents the temperature obtained at point E for varying mesh refinements and ele-

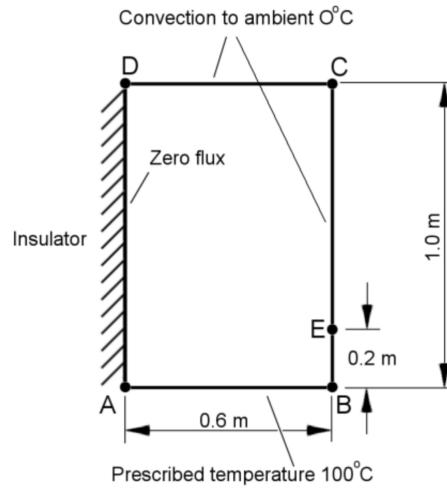


Figure 6.1: Problem description for the steady state heat analysis [27].

ment types from the heat model formulated in Section 5.2. The results from the Strand7 verification manual [27] are also provided and for each analysis a comparison is made to the solution given by NAFEMS. Figures 6.2 and 6.3 present plots of the steady state temperature field throughout the domain for each mesh refinement and element type.

Model	Heat Model Results	Strand7 Results
<i>QUAD4; Coarse Mesh</i>	-0.197°C (-101%)	8.500°C (-53.6%)
<i>QUAD4; Medium Mesh</i>	17.979°C (-1.75%)	17.950°C (-1.91%)
<i>QUAD8; Coarse Mesh</i>	19.171°C (4.76%)	17.895°C (-2.21%)
<i>QUAD8; Medium Mesh</i>	18.865°C (3.09%)	18.790°C (2.68%)
<i>QUAD8; Fine Mesh</i>	18.255°C (-0.25%)	N/A

Table 6.2: Comparison of the steady state heat model results with Strand7 and, in parenthesis, NAFEMS.

The implementation of the heat model used in this thesis produced steady state results that are comparable those of the benchmark and Strand7 results for all models except the coarse mesh with linear elements. For this exception, the Strand7 analysis also produced results that significantly deviate from the benchmark. The Strand7 verification manual [27] notes that linear elements cannot reproduce the required temperature gradient for coarse elements and therefore this result can be omitted. This is further highlighted in Figures 6.2 and 6.3, which show that mesh refinement in the bottom right of the domain is required in order to capture the temperature gradient, which varies in two directions.

For all other models, the heat model was within a 5% error margin of the benchmark results and for the fine mesh models was within a 0.5% margin of the Strand7 results. When the mesh was further refined, the heat model converged to the benchmark result and produced the expected smooth temperature gradient as shown in Figure 6.3. These results provided evidence that the implementation of the heat model for this thesis produces expected results and can be used with confidence for steady-state transport problems.

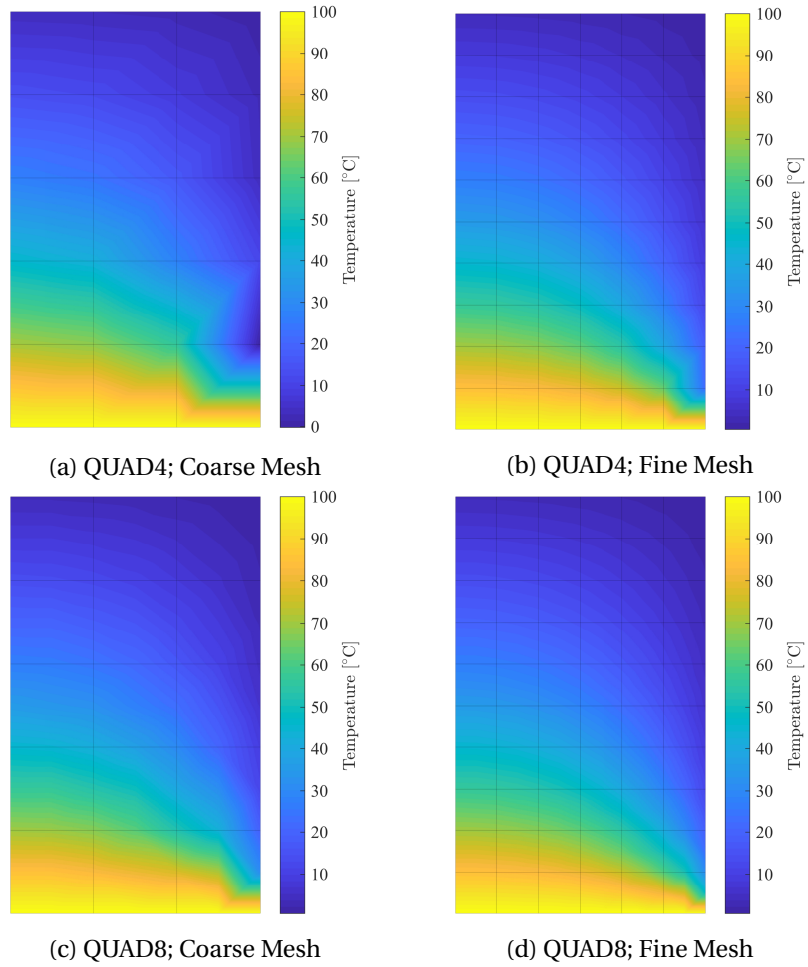


Figure 6.2: Steady state heat model results for varying mesh refinement and element type.

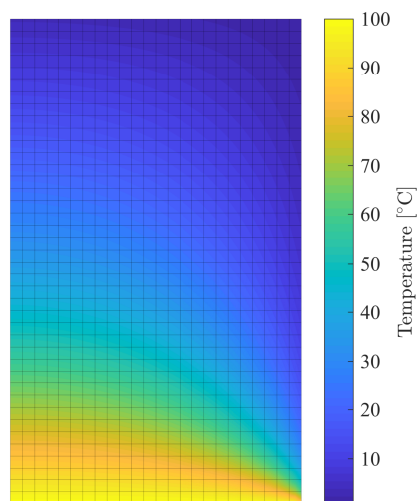


Figure 6.3: Heat model temperature field results for the super fine mesh refinement with QUAD8 elements.

6.1.2. Transient Analysis

In this transient analysis a 2D heat transfer problem was modelled that consisted of both fixed temperatures and a convective boundary condition. Figure 6.4 describes the problem, in which a temperature of 300°C was prescribed to the edges AC and BD, and edge AB was insulated with zero heat flux. Edge CD was subjected to a convective boundary condition with an ambient fluid temperature equal to 50°C . The initial temperature of the material was 300°C . The material properties, time steps and mesh density are given in Table 6.3. The reference solution, as provided by 'Heat Transfer' (Holman, 1989), is a temperature of 243.32°C at point E after 12 seconds.

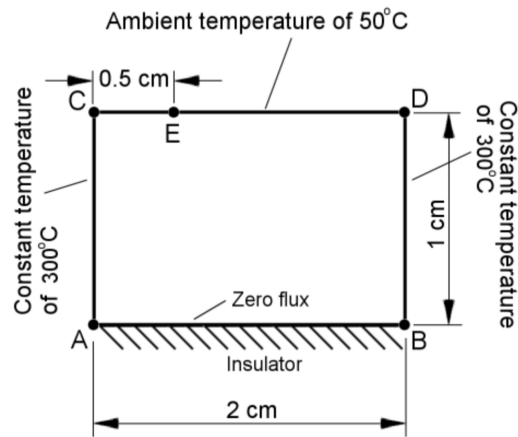


Figure 6.4: Problem description for the transient heat analysis.

Input	Properties
<i>Material Properties</i>	$\kappa = 3.0 \text{ J} / (\text{s} \cdot \text{m} \cdot \text{K})$; $h = 200.0 \text{ J} / (\text{s} \cdot \text{m}^2 \cdot \text{K})$ $\rho = 1600 \text{ kg} / \text{m}^3$; $c = 800 \text{ J} / (\text{kg} \cdot \text{K})$; $T_f = 50^{\circ}\text{C}$; $T_{\text{init}} = 300^{\circ}\text{C}$
<i>Time Steps</i>	$\Delta t = 2 \text{ s}$ $t_{\text{final}} = 12 \text{ s}$
<i>Mesh Density</i>	QUAD4 Mesh: $2.5 \times 10^{-3} \text{ m} \times 2.5 \times 10^{-3} \text{ m}$ QUAD8 Mesh: $5.0 \times 10^{-3} \text{ m} \times 5.0 \times 10^{-3} \text{ m}$

Table 6.3: Input for the transient heat analysis.

Table 6.4 presents the temperature obtained at point E for varying element types for the heat model formulated in Section 5.2. The results from the Strand7 verification manual [27] are also provided and comparison is made with reference to the solution given by Holman. Figure 6.5 presents a plot of the temperature field throughout the domain for each element type at $t = 12 \text{ s}$. Figure 6.6 presents a plot of the temperature field throughout the domain for a further refined mesh of $2.5 \times 10^{-4} \text{ m} \times 2.5 \times 10^{-4} \text{ m}$ at various time steps.

From Table 6.4 it is apparent the transient results from the heat model are almost identical to the results obtained from the Strand7 analysis. The results from all models are within a 2.5% error margin of the benchmark result. Figure 6.5b shows that the quadratic elements were able to capture the temperature gradient for this problem, even with a relatively coarse mesh. As a result, there is

Model	Heat Model Results	Strand7 Results
QUAD4	237.83°C (-2.26%)	238.21°C (-2.10%)
QUAD8	237.25°C (-2.49%)	237.31°C (-2.47%)
QUAD8; Refined Mesh	237.94°C (-2.30%)	N/A

Table 6.4: Comparison of the transient heat model results with Strand7 and, in parenthesis, Holman.

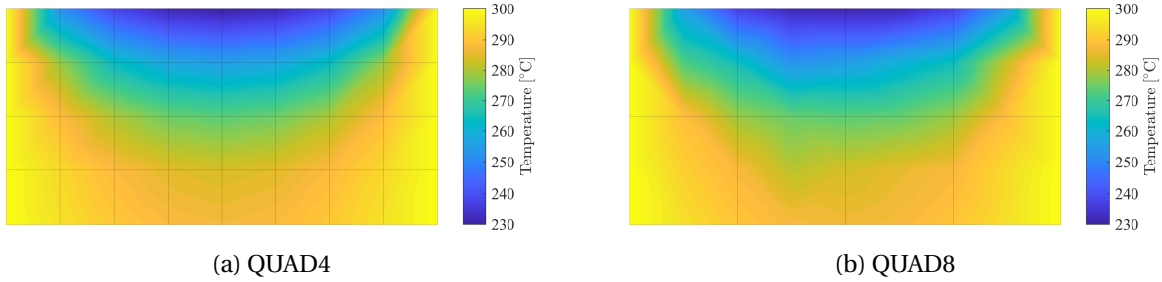


Figure 6.5: Transient heat model results at $t = 12$ s for varying element type.

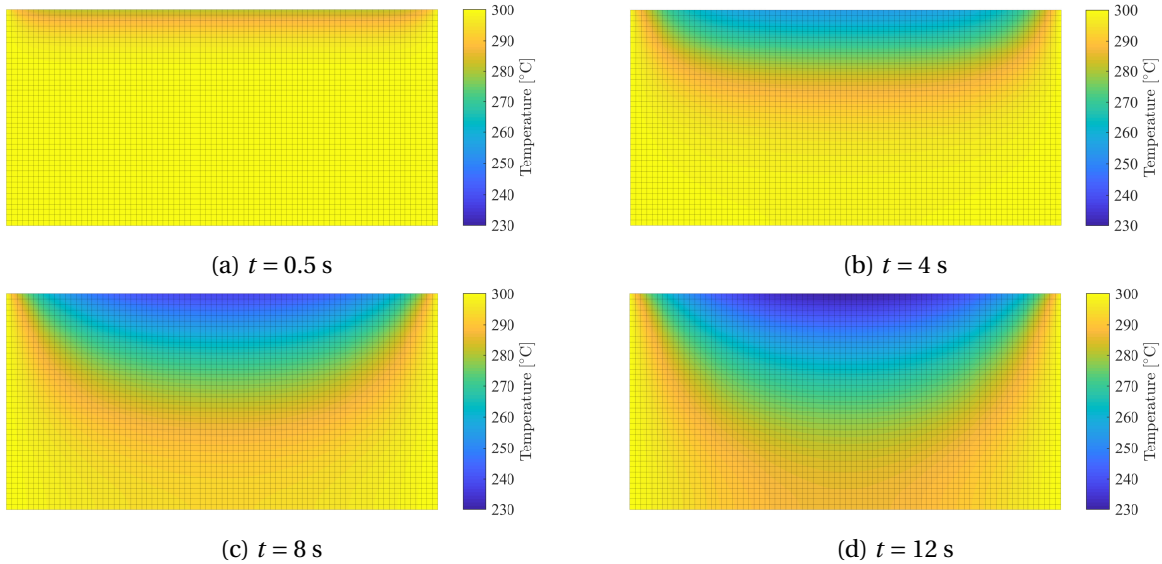


Figure 6.6: Transient heat model results for the refined mesh at different time steps.

no significant variation between the temperature fields when the mesh is refined by a factor of 2 and linear elements are used, which is the difference between the QUAD8 to the QUAD4 models. The time dependent heat conductivity, depicted from Figure 6.6a to Figure 6.6d, produced temperature fields that are consistent with the expected smooth gradient between the fixed sides and the cooling top edge.

When the mesh is further refined, the temperature at point E approaches the benchmark solution, although there is still a 2.3% difference between the results. This difference can be attributed to the use of a non-linear thermal analysis used in the benchmark solution, which acts to modify the constitutive relationship as the temperature field changes, and is not included in the formulation of the heat model in this thesis. As a result, the transient results produced by the heat model in the benchmark test can be used to justify the validity of the implementation of the model in this thesis.

6.2. Constitutive Model 1 - Mechanics Model

A series of benchmark numerical tests were performed on the first constitutive model described in Section 5.4.1 in order to validate the model and also to highlight the capabilities of the glass transition and degradation models. In each test the expected analytical results are derived and contrasted with the numerical results.

These numerical benchmark tests were performed on a one element model with the same geometry as the square bar used in the mesh dependency tests, described in Section 3.2.1. The material properties used in these benchmark tests are summarised in Table 6.5 below.

Model	Glassy Properties	Rubbery Properties
<i>Viscoelasticity</i>	$E_{\infty}^{\text{gla}} = 2900 \text{ MPa}; \nu_{\infty}^{\text{gla}} = 0.35$	$E_{\infty}^{\text{rub}} = 1000 \text{ MPa}; \nu_{\infty}^{\text{rub}} = 0.45$
	$K_i^{\text{gla}} = [500 \text{ MPa}, 250 \text{ MPa}, 100 \text{ MPa}]$	$K_i^{\text{rub}} = [250 \text{ MPa}, 125 \text{ MPa}, 50 \text{ MPa}]$
	$G_i^{\text{gla}} = [166.7 \text{ MPa}, 83.3 \text{ MPa}, 33.3 \text{ MPa}]$	$G_i^{\text{rub}} = [51.7 \text{ MPa}, 25.9 \text{ MPa}, 10.3 \text{ MPa}]$
	$\lambda_{i,k} = [0.01 \text{ s}, 0.1 \text{ s}, 0.25 \text{ s}]$	
	$\lambda_{i,g} = [0.02 \text{ s}, 0.5 \text{ s}, 0.75 \text{ s}]$	
<i>Viscoplasticity</i>	$\sigma_t^{\text{gla}} = 70 \text{ MPa}$	$\sigma_t^{\text{rub}} = 20 \text{ MPa}$
	$\sigma_c^{\text{gla}} = 90 \text{ MPa}$	$\sigma_c^{\text{rub}} = 30 \text{ MPa}$
	$\nu_p = 0.5; \eta_p = 205 \times 10^3 \text{ MPa} \cdot \text{s}; m_p = 1.5$	
<i>Glass Transition</i>	$T_g = 363.3 \text{ K}; H = 20 \text{ MPa}$	
	$\phi_T = 1 \text{ MPa}; \phi_{\omega} = 145 \text{ MPa}$	

Table 6.5: Material properties used in the mechanics model benchmark tests.

6.2.1. Monotonic Tension

Three monotonic tension simulations were performed on the first constitutive model. The first two tests were performed with only the linear viscoelasticity model activated (no viscoplasticity), while the third test incorporated both linear viscoelasticity and viscoplasticity.

6.2.1.1. Constant Strain Rate (VE):

A constant strain rate of $\dot{\epsilon}_{xx} = 0.1/\text{min}$ was used to load the specimen to a final strain of 10% in each test. The relatively low strain rate effectively removed any viscoelastic effects in these tests. Five tests were performed, in which the temperature and moisture concentration of the sample was varied. The temperature and moisture concentration for each test, as well as the corresponding degree of glass transition relating to these parameters are presented in Table 6.6.

	Test 1	Test 2	Test 3	Test 4	Test 5
Temperature T	298 K	358 K	358 K	358 K	380 K
Moisture Content ω	0.000	0.000	0.005	0.010	0.000
Degree of Glass Transition ζ	0.000	0.235	0.748	0.960	1.000

Table 6.6: Temperature, moisture concentration and resulting ζ used in each constant strain rate tension test.

The analytical results for this benchmark test are derived below in Box 6.2.1.

Box 6.2.1: Monotonic Tension - Constant Strain Rate (VE): Analytical Results

For each test described in Table 6.6 both the tensile force F_t required to impose a strain of 10%, and the transverse displacement given a longitudinal displacement of 10 mm are calculated.

First, the degraded elastic stiffness for each test can be calculated using the degree of glass transition in Table 6.6:

$$E_{\infty}(\zeta) = (1 - \zeta)E_{\infty}^{\text{gla}} + \zeta E_{\infty}^{\text{rub}} \quad (6.1)$$

The force, given a strain of 10%, can now be calculated:

$$F_t = \sigma A = E_{\infty}(\zeta)\varepsilon_{xx} A = E_{\infty}(\zeta) \times 0.1 \times 100 \text{ mm}^2 = 10E_{\infty}(\zeta) \quad (6.2)$$

In order to calculate the transverse displacement, the degraded Poisson's ratio must first be calculated. Similar to the elastic stiffness, the Poisson's ratio for each test can be calculated using the degree of glass transition in Table 6.6:

$$\nu_{\infty}(\zeta) = (1 - \zeta)\nu_{\infty}^{\text{gla}} + \zeta\nu_{\infty}^{\text{rub}} \quad (6.3)$$

The transverse displacement can then be calculated from the degraded Poisson's ratio, the longitudinal strain and the transverse width of the bar, $b = 10 \text{ mm}$:

$$u_y = -\nu_{\infty}(\zeta)\varepsilon_{xx}b = -\nu_{\infty}(\zeta) \times 0.1 \times 10 \text{ mm} = -\nu_{\infty}(\zeta) \quad (6.4)$$

Using the above equations, the analytical results for each test are summarised below in Table 6.7.

	Test 1	Test 2	Test 3	Test 4	Test 5
E_{∞}	2900 MPa	2454 MPa	1479 MPa	1076 MPa	1000 MPa
ν_{∞}	0.350	0.374	0.425	0.446	0.450
F_t	$29.00 \times 10^3 \text{ N}$	$24.54 \times 10^3 \text{ N}$	$14.79 \times 10^3 \text{ N}$	$10.76 \times 10^3 \text{ N}$	$10.00 \times 10^3 \text{ N}$
u_y	-0.350 mm	-0.374 mm	-0.425 mm	-0.446 mm	-0.450 mm

Table 6.7: Analytical results for the constant strain rate tension test.

Figure 6.7 presents the numerical results obtained for the constant strain rate monotonic tension tests. Figure 6.7a presents a load displacement plot for each test and Figure 6.7b presents the transverse displacement as a function of the longitudinal displacement for each test.

It is clear from Figure 6.7 that the numerical results exactly match the analytical results for long term mechanical degradation behaviour. Further, both the analytical results and the numerical results present behaviour that is consistent with the intent of the degradation model. Figure 6.7a shows that the state transition of the epoxy resin from glassy to rubbery is accompanied by a reduction in the elastic modulus. Further, Figure 6.7b shows that this transition is also accompanied by an increase in the Poisson's ratio. As a result, the model formulation used in this thesis can effectively relate long term mechanical behaviour with the state of the epoxy resin.

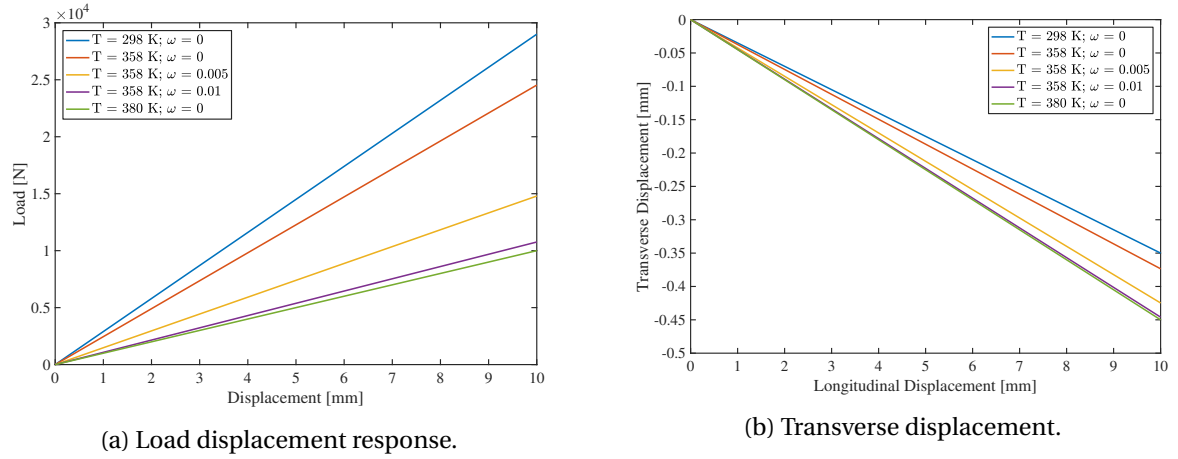


Figure 6.7: Numerical results for the constant strain rate tension tests.

6.2.1.2. Varying Strain Rates (VE):

Numerical monotonic tension tests were performed at two different temperatures and three different strain rates, with a final strain of $\varepsilon_{xx} = 10\%$. A total of six numerical tests were studied and the temperature and strain rate for each test is given in Table 6.8.

	Test 1	Test 2	Test 3	Test 4	Test 5	Test 6
Temperature	298 K	298 K	298 K	380 K	380 K	380 K
Strain Rate	$10^0/\text{min}$	$10^3/\text{min}$	$10^6/\text{min}$	$10^0/\text{min}$	$10^3/\text{min}$	$10^6/\text{min}$

Table 6.8: Temperature and strain rate used in each varying strain rate tension test. Note that a temperature of 298 K corresponds to $\zeta = 0$ and a temperature of 380 K corresponds to $\zeta = 1$.

The analytical results for this benchmark test are derived below in Box 6.2.2.

Box 6.2.2: Monotonic Tension - Varying Strain Rate (VE): Analytical Results

For the tests with $\dot{\varepsilon} = 1/\text{min}$, the results from the previous test can be used as this strain rate also results in negligible viscoelastic stresses. For the tests with $\dot{\varepsilon} = 1 \times 10^6/\text{min}$, there is negligible relaxation of the viscoelastic stresses and thus the viscoelastic stiffness components can be added to the long term stiffness. The total stiffness for the glassy and rubbery tests is therefore:

$$E^{\text{gla}} = E_{\infty}^{\text{gla}} + \frac{9 \sum_i K_i^{\text{gla}} \sum_i G_i^{\text{gla}}}{3 \sum_i K_i^{\text{gla}} + \sum_i G_i^{\text{gla}}} = 2900 + 765 = 3665 \text{ MPa} \quad (6.5a)$$

$$E^{\text{rub}} = E_{\infty}^{\text{rub}} + \frac{9 \sum_i K_i^{\text{rub}} \sum_i G_i^{\text{rub}}}{3 \sum_i K_i^{\text{rub}} + \sum_i G_i^{\text{rub}}} = 1000 + 247 = 1247 \text{ MPa} \quad (6.5b)$$

For the tests with $\dot{\varepsilon} = 1 \times 10^3/\text{min}$, the relaxation of the viscoelastic stresses affects the total stiffness and therefore this analytical calculation is not performed. However, the stiffness for $\dot{\varepsilon} = 1 \times 10^3/\text{min}$ is bounded by the stiffnesses obtained from $\dot{\varepsilon} = 1/\text{min}$ and $\dot{\varepsilon} = 1 \times 10^6/\text{min}$. As a result, given a strain of 10%, the forces can be calculated using the same method as given in Box 6.2.1:

	Test 1	Test 2	Test 3
E_∞	2900 MPa	$2900 \text{ MPa} < E_\infty < 3665 \text{ MPa}$	3665 MPa
F_t	$29.00 \times 10^3 \text{ N}$	$29.00 \times 10^3 \text{ N} < F_t < 36.65 \times 10^3 \text{ N}$	$36.65 \times 10^3 \text{ N}$
	Test 4	Test 5	Test 6
E_∞	1000 MPa	$1000 \text{ MPa} < E_\infty < 1247 \text{ MPa}$	1247 MPa
F_t	$10.00 \times 10^3 \text{ N}$	$10.00 \times 10^3 \text{ N} < F_t < 12.47 \times 10^3 \text{ N}$	$12.47 \times 10^3 \text{ N}$

Table 6.9: Analytical results for the varying strain rate tension test.

Figure 6.8 presents the load displacement response obtained for the varying strain rate monotonic tension tests with only linear viscoelasticity activated. It is apparent from this figure that the numerical loads at a strain of 10% match the analytical results for $\dot{\epsilon} = 1/\text{min}$ and $\dot{\epsilon} = 1 \times 10^6/\text{min}$ as computed in Table 6.9.

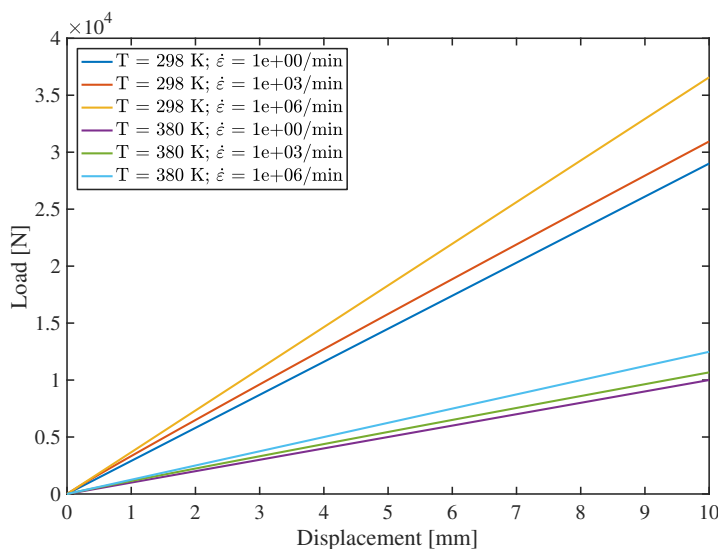


Figure 6.8: Numerical load displacement response for the varying strain rate linear viscoelasticity tension tests.

In Figure 6.8 some features of the degraded viscoelastic model are present. First, the stiffness is clearly dependent on the strain rate. As expected, an increase in the strain rate resulted in an increased stiffness. Second, as was the case for the previous simulation, the glassy response was stiffer than that of the rubbery state. Further, the increase in stiffness of the rubbery specimens was lower than the increases in the glassy specimens due to higher strain rates. This is because the viscoelastic Prony stiffnesses are also degraded in the viscoelastic degradation model. Because the glassy Prony stiffnesses provided as input in Table 6.5 are higher than the corresponding rubbery stiffnesses, the increase in viscoelastic stress resulting from an increased strain rate was lower for the rubbery specimens. As a result, this set of simulations demonstrates the rate dependency capabilities of the viscoelastic model and show how these properties are also dependent on the state of the epoxy resin.

6.2.1.3. Varying Strain Rates (VE-VP):

The same monotonic tension tests that were described in the previous section (varying strain rates with VE) were performed with viscoplasticity activated. The strain rates from the previous test were

modified and are presented in Table 6.10.

	Test 1	Test 2	Test 3	Test 4	Test 5	Test 6
Temperature	298 K	298 K	298 K	380 K	380 K	380 K
Strain Rate	0.1/min	20/min	100/min	0.1/min	20/min	100/min

Table 6.10: Temperature and strain rate used in each varying strain rate tension test. Note that a temperature of 298 K corresponds to $\zeta = 0$ and a temperature of 380 K corresponds to $\zeta = 1$.

Because the viscoplastic analysis is incremental, there is no simple way to calculate analytical yield strengths based on a given strain rate. However, two elementary predictions can be made. The first is that, at low strains rates, the viscoplastic response should coincide with perfectly plasticity because the time increment is large enough to make any delay in plastic strain development insignificant. Second, higher strain rates should result in a hardening behaviour and a subsequent increase in the observed yield strength.

Figure 6.9 presents the stress-strain response obtained for the varying strain rate monotonic tension tests with linear viscoelasticity and viscoplasticity activated.

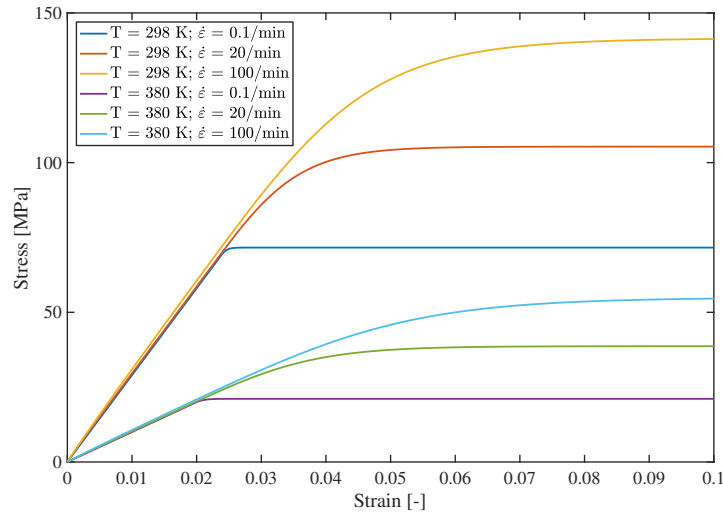


Figure 6.9: Numerical stress-strain response for the varying strain rate linear viscoelasticity and viscoplasticity tension tests.

The numerical results presented in Figure 6.9 match with the expected viscoplastic behaviour, in which higher strain rates result in a higher yield plateau. The delay of plastic strains caused by the viscoplasticity model is apparent, and for higher strain rates, there is a larger transition zone between elastic and perfectly plastic behaviour. The application of the degradation model to the yield strength is depicted clearly in Figure 6.9, in which the rubbery epoxy resin yields at a significantly lower stress when compared to the glassy sample. As a result, this numerical simulation highlights the ability of the constitutive model to capture rate dependent plasticity behaviour as well as material state dependent yielding.

6.2.2. Loading-Unloading

Two loading-unloading simulations were performed on the first constitutive model to highlight the unloading behaviour and the hysteresis caused by viscous dissipations. The first test was performed with only the linear viscoelasticity model activated, while the second test incorporated both linear viscoelasticity and viscoplasticity.

6.2.2.1. Varying Strain Rates (VE):

Numerical loading-unloading tests were performed at two different temperatures and three different strain rates, with a maximum strain of $\epsilon_{xx} = 5\%$. A total of six numerical tests were studied, in which the temperature and strain rate for each test were the same as for the monotonic tension VE tests and are given in Table 6.8.

Figure 6.10 presents the stress-strain response obtained for the varying strain rate loading-unloading tests with only linear viscoelasticity activated.

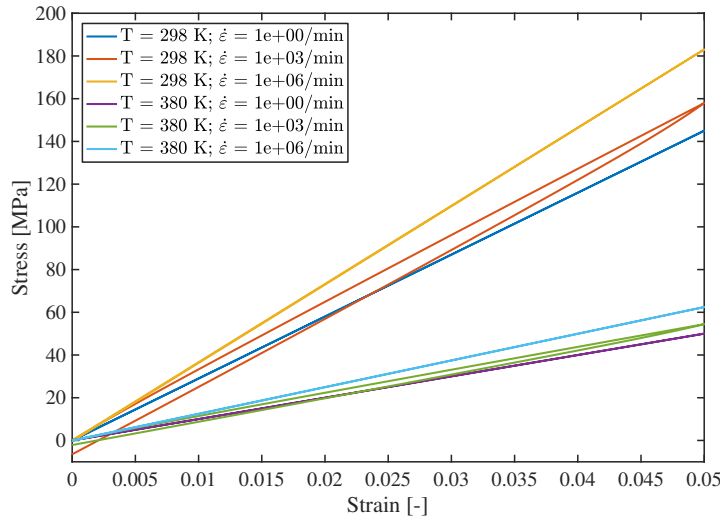


Figure 6.10: Numerical stress-strain response for the varying strain rate linear viscoelasticity loading-unloading tests.

The loading branches of the simulations in Figure 6.10 are identical to the results presented in Figure 6.8, with strain rate dependency and material property degradation captured. The unloading branches highlight some of the observed behaviour discussed in Section 2.1.1, notably hysteresis and stress relaxation.

The tests with $\dot{\epsilon} = 1/\text{min}$ did not exhibit this behaviour, as the strain rate was too low to activate significant viscoelastic stresses. However, the tests with $\dot{\epsilon} = 1 \times 10^3/\text{min}$ showed a relaxation of the viscoelastic stiffness once the unloading commenced, resulting in hysteresis during unloading. Once the strain was brought back to the initial state, a compressive stress was present within the specimen. This highlights the stress relaxation behaviour of the viscoelastic model, which manifested in the lowering of the mean cyclic stress. Similar to the monotonic tension tests, the degradation of the viscoelastic stiffnesses is visible in Figure 6.10 because a smaller degree of stress relaxation and hysteresis was present in the rubbery sample when compared to the glassy sample.

Although the tests with $\dot{\epsilon} = 1 \times 10^6/\text{min}$ show an increased stiffness resulting from the relatively high strain rate, no stress relaxation or hysteresis was present in the unloading branch. The loading and unloading of the specimen in this test occurred within a relatively short period of time $t = 1 \times 10^{-6}$ s as a result of the high strain rate. Because this time was significantly lower than any of the relaxation times for the material, as can be seen in Table 6.5, there was no appreciable decay of the viscoelastic stresses and the unloading branch is identical to the loading branch.

This loading-unloading simulation highlights the ability of the viscoelastic degradation model to capture significant observed mechanical behaviour of epoxy resins, such as hysteresis and stress relaxation.

6.2.2.2. Varying Strain Rates (VE-VP):

Numerical loading-unloading tests on the constitutive model with viscoplasticity activated were performed at two different temperatures and three different strain rates, with a maximum strain of

$\epsilon_{xx} = 5\%$. The strain rates chosen in this test correspond to the rates used in the monotonic VE-VP tests and are given in Table 6.10.

Figure 6.11 presents the stress-strain response obtained for the varying strain rate loading-unloading tests with linear viscoelasticity and viscoplasticity activated.

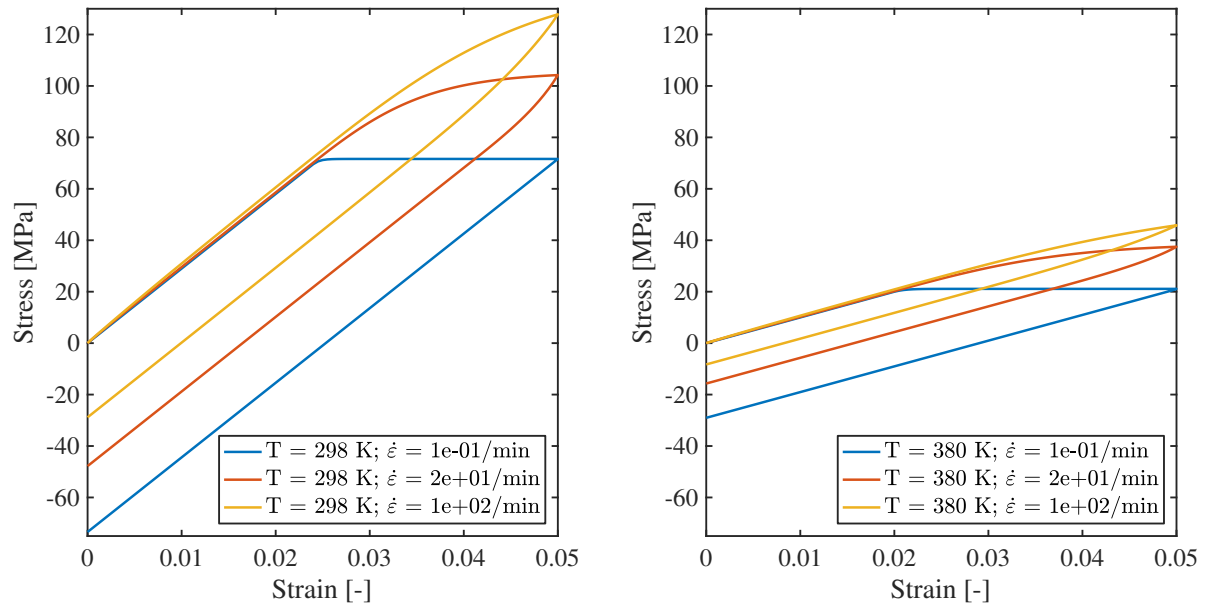


Figure 6.11: Numerical stress-strain response for the varying strain rate linear viscoelasticity and viscoplasticity loading-unloading tests.

As with the previous test, the loading behaviour observed in Figure 6.11 was identical to the monotonic tension test presented in Figure 6.9. The tests with $\dot{\epsilon} = 0.1/\text{min}$ exhibited a near perfectly elastic-plastic response, due to the fact that time dependent effects were negligible because of the relatively low strain rate. The tests with $\dot{\epsilon} = 20/\text{min}$ highlight the delay of plastic straining due to viscoplastic effects, however, also contained minor relaxation of viscoelastic stresses at the beginning of the unloading branch. It is apparent from Figure 6.11 that a higher strain rate resulted in a reduction of the residual stress, which can be attributed to the delay in plastic strain development. The tests with $\dot{\epsilon} = 100/\text{min}$ contained a larger component of viscoelastic stress due to the increased strain rate. This viscoelastic stress decayed over a larger portion of the unloading branch when compared with the branch from the $\dot{\epsilon} = 20/\text{min}$ tests.

When comparing Figure 6.11 with Figure 6.10 it is apparent from the hysteresis loops that the energy dissipation caused by viscoplastic deformation was significantly larger than the dissipation resulting from viscoelastic deformation. Further, for a given loading-unloading cycle, the energy dissipated by an epoxy resin in a glassy state was larger than if the epoxy resin were in a rubbery state. As a result, this simulation shows how the constitutive formulation can capture complex time and state dependent viscoelastic and viscoplastic behaviour.

6.2.3. Loading-Unloading-Reloading

A loading-unloading-reloading simulation was performed on the first constitutive model in order to highlight the full linear viscoelastic and viscoplastic behaviour in combination with the glass transition degradation model for cyclic and fatigue type tests.

6.2.3.1. Constant Strain Rate (VE-VP):

A constant strain rate of $\dot{\epsilon}_{xx} = 200/\text{min}$ was used to load and unload the specimen in 1% strain increments. Three tests were performed in which the temperature of the sample was chosen to

represent a degree of glass transition of $\zeta = 0$, $\zeta = 0.5$ and $\zeta = 1$ respectively.

Figure 6.12 presents the stress-strain response obtained for the loading-unloading-reloading tests performed on constitutive model 1.

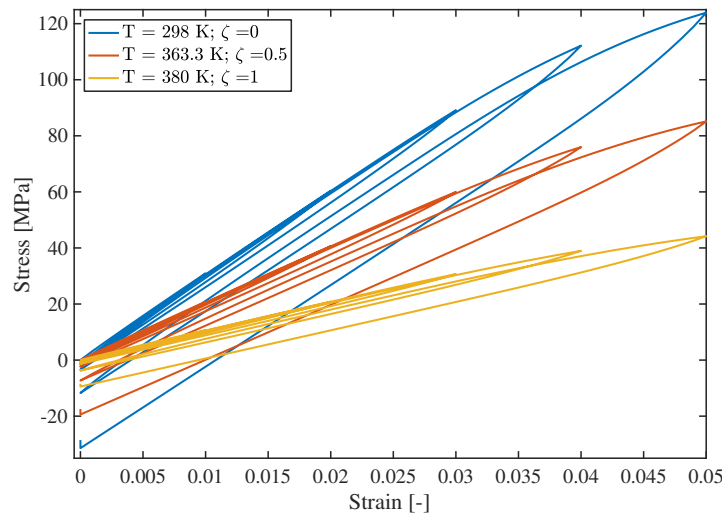


Figure 6.12: Numerical stress-strain response for the loading-unloading-reloading linear viscoelasticity and viscoplasticity tests.

In the results presented in Figure 6.12 capture both viscoelastic and viscoplastic behaviour, as well as the resulting material degradation effects present in both models. In particular, the long term and viscoelastic stiffness and the yield strength have been degraded.

In this particular example, the onset of viscoplasticity occurred at similar strains for all three tests. This is because the rubbery yield strength was degraded by a similar factor to the elastic modulus, see Table 6.11. Given a lower rubbery yield strength, it is possible that the onset of plasticity, as captured in the numerical model, could occur at a differing strains for different material states.

Also captured in this strain controlled test is the phenomenon of stress relaxation. After each successive load cycle, an increasing compressive residual stress was developed, which acted to lower the mean stress of the cycle. It should be noted that if a load controlled test was performed, this same phenomenon would be present in the form of ratcheting. At the conclusion of each test, the strain was kept at zero for an extended amount of time, allowing the viscoelastic stresses to relax. This allowed the viscoplastic stresses to be isolated from the viscoelastic stresses for the final stress state, which can aid model calibration. By examining the final stresses, it was apparent that the glassy specimen comprised of larger components of both viscoelastic and viscoplastic stresses, matching the results from the previous simulations.

In conclusion, this simulation, and all the previous simulations, illustrate the ability of the formulated constitutive model to describe the state dependent mechanical behaviour as mentioned in Section 2.1.1. The only mechanical behaviour not captured by the first constitutive model used in these simulations was the onset of elastic non-linearity, which is included in the second constitutive model. As a result, the glass transition, material degradation and viscoplastic models formulated in this thesis can be used to numerically model the mechanical behaviour of epoxy resins.

6.3. Multiphysics Model

Two simulations were performed in order to demonstrate the capabilities of the multiphysics model. Both simulations analysed a dogbone specimen, the geometry of which is described in Figure 6.13. In these simulations the first constitutive model was used (see Section 5.4.1), which, when used in a multiphysical sense, incorporates heat conduction, moisture diffusion, linear viscoelasticity, viscoplasticity, and a degradation model based on the concept of the glass transition surface. The first simulation focussed on the relationship between the transport behaviour and the degree of glass transition, while the second simulation investigated the multiphysical aspects of a mechanical fatigue test.

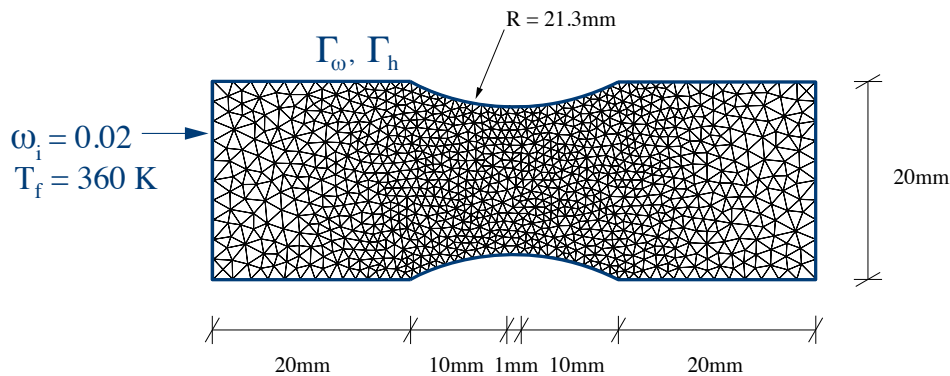


Figure 6.13: Mesh used for the multiphysics model, showing the applied boundary conditions.

6.3.1. Glass Transition Behaviour

In this simulation a multiphysics heat conduction and moisture diffusion problem was modelled and its effect on the state of an epoxy resin dogbone sample was investigated. Although no mechanical restraint was applied to the specimen, this analysis incorporated all three physics models because the glass transition model required the inclusion of the mechanics model. To simplify the problem and the interpretation of the results, the 2D plane strain assumption was used to constrain the transport behaviour to the plane of the dogbone sample.

In this problem, an initially dry epoxy resin sample at room temperature (298 K) was immersed in water with a temperature of 360 K. The relevant material properties for each physics model are described in Table 6.11 and the boundary conditions summarised in Figure 6.13. Note that although not entirely realistic, the conductivity and diffusivity of the heat and diffusion model were chosen such that moisture ingress into the specimen and eventual saturation occurred at a faster rate than the conduction of heat. This facilitated a more simple interpretation of the degree of glass transition results.

The simulation was performed with a time increment of 0.05 s and was run for a total simulation time of 100 s. Three noded triangular elements were used to discretise the domain of the dogbone and two noded line elements were used to model the convective boundary interface between the epoxy resin and the surrounding fluid for the heat model.

Figure 6.14 presents contour plots of the temperature, moisture concentration and degree of glass transition fields within the dogbone specimen at four different time steps. Figure 6.15 presents the variation of the temperature, moisture concentration and degree of glass transition with time. Note that in Figure 6.15, each field variable is normalised to a value between 0 and 1 with respect to the minimum and maximum values obtained in the analysis. The expressions for the normalised

Model	Material Properties
<i>Heat Model</i>	$\kappa = 0.35 \text{ J} / (\text{s} \cdot \text{m} \cdot \text{K})$; $h = 500 \text{ J} / (\text{s} \cdot \text{m}^2 \cdot \text{K})$ $\rho = 1250 \text{ kg} / \text{m}^3$; $c = 1000 \text{ J} / (\text{kg} \cdot \text{K})$;
<i>Diffusion Model</i>	$D_\omega(T) = D_\omega = 1 \times 10^{-6} \text{ m}^2 / \text{s}$
<i>Mechanics Model</i> <i>(Glass Transition)</i>	$T_g = 363.3 \text{ K}$; $H = 20 \text{ MPa}$ $\phi_T = 1 \text{ MPa}$; $\phi_\omega = 145 \text{ MPa}$

Table 6.11: Material properties used for the multiphysics simulation investigating glass transition behaviour.

variables are given below:

$$\bar{T} = \frac{T - 298 \text{ K}}{360 \text{ K} - 298 \text{ K}} \quad (6.6a)$$

$$\bar{\omega} = \frac{\omega}{0.02} \quad (6.6b)$$

$$\bar{\zeta} = \zeta \quad (6.6c)$$

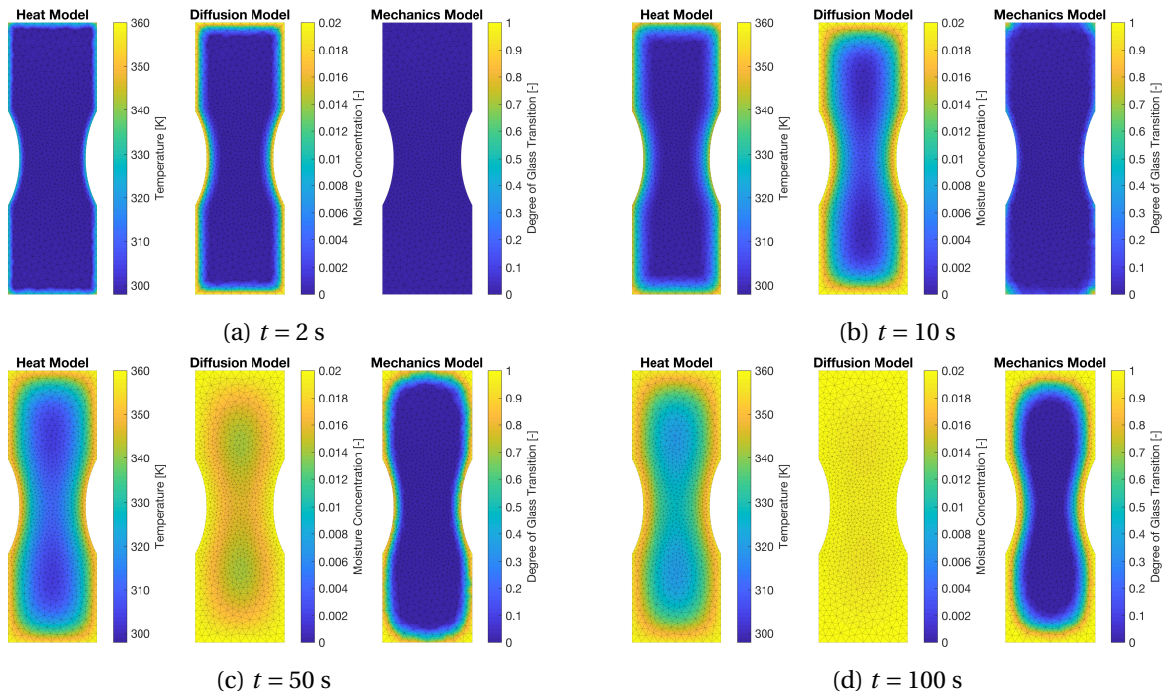


Figure 6.14: Contour plots of the temperature, moisture concentration and degree of glass transition for the multiphysics analysis.

Figure 6.14 clearly presents the development of glass transition within an epoxy resin dogbone sample. Figure 6.14b indicates that the glass transition began at the corners of the dogbone, where convective temperature flux from the ambient fluid is the greatest. The onset of glass transition can be analytically confirmed through the interpretation of Figure 6.15a, in which the onset of glass

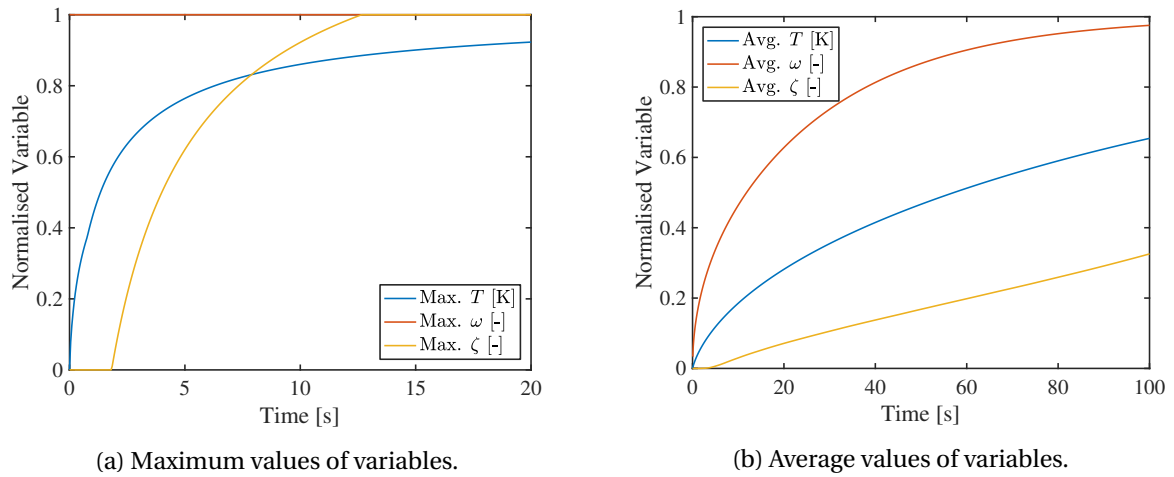


Figure 6.15: Variation of temperature, moisture concentration and degree of glass transition with time.

transition occurs at time $t = 1.8$ s. At this point in time the maximum temperature occurred at the corner of the specimen and is approximately 333 K, see Figure 6.15a. Equation 5.31 can be evaluated to determine the value of ζ given a moisture concentration of $\omega = 0.02$ and $T = 333$ K:

$$\zeta = \zeta^* = \frac{\phi_t(T - T_g) + \phi_\omega\sqrt{\omega} + \frac{H}{2}}{H} \quad (6.7)$$

$$= \frac{1(333 - 363.3) + 145\sqrt{0.02} + \frac{20}{2}}{20} \quad (6.8)$$

$$= 0.01 \quad (6.9)$$

thus coinciding with the onset of glass transition. Further, the onset of the rubbery state at $\zeta = 1$ can also be verified from Figure 6.15a, which occurs at $t = 12.7$ s. The corresponding maximum temperature at this time, seen in Figure 6.15a, is approximately 353 K. Therefore, evaluating Equation 5.31 results in:

$$\zeta = \min(\zeta^*, 1) = \min\left(\frac{\phi_t(T - T_g) + \phi_\omega\sqrt{\omega} + \frac{H}{2}}{H}, 1\right) \quad (6.10)$$

$$= \min\left(\frac{1(353 - 363.3) + 145\sqrt{0.02} + \frac{20}{2}}{20}, 1\right) \quad (6.11)$$

$$= \min(1.01, 1) \quad (6.12)$$

$$= 1.00 \quad (6.13)$$

thus coinciding with full development of the rubbery state. Further, from Figure 6.14, there is a clear correlation between the transport fields from the heat and diffusion models, and the degree of glass transition field in the mechanics model. As a result, the combination of these analytical calculations and the numerical results presented in Figures 6.14 and 6.15 validates the link between the results from the transport model and the glass transition model.

A significant simplification in the formulation by Yu et al. [32] is that their implementation requires a uniform temperature, moisture and strain field over the domain. This numerical simulation highlights one of the major advantages that the finite element formulation used in this thesis has over the model used by Yu et al. Figure 6.14 highlights the ability of this formulation to capture

complex field gradients in the transport models and, in conjunction with the degradation model, simulate an epoxy resin specimen consisting of varying material states. As an example, if a load was applied to the specimen from Figure 6.14d at $t = 100$ s, the mechanics model would be able to capture the stiffness variation throughout the specimen. In this hypothetical situation the edges of the specimen would lose a significant amount of stiffness due to the state transition and the load within the specimen would be redistributed to the glassy region. This phenomenon is studied in more detail in the next simulation.

The results from this simulation help to validate the sharing of field data between the various physical models. Further, this simulation highlights the versatility of the numerical framework formulated in this thesis. By utilising the finite element method, the constitutive model can be applied to simulate the response of composite laminates in complex problems.

6.3.2. Fatigue Test

In this test, simulations similar to the experimental fatigue tests undertaken by Chen et al. [4] and numerically studied by Yu et al. [32], were investigated using the constitutive model formulated in this thesis. As detailed in Section 2.1.3, Chen et al. observed cyclic softening of an epoxy resin sample subjected to a constant strain amplitude at varying strain rates. Chen et al. found that increasing cyclic softening occurred with larger strain rates and was accompanied by a rise in the average temperature of the specimen. They also found that the energy dissipated in one cycle does not monotonically increase with the applied strain rate. As a result, for a given epoxy resin, there exists a strain rate that maximises the peak energy dissipation.

A sinusoidal imposed tensile strain of 2.5% was applied to a three-dimensional dogbone sample. The sample remained dry throughout the test and as a result, only the heat model and mechanics model were used in this simulation. A convective boundary condition was applied to all surfaces of the dogbone sample in order to model the air surrounding the sample, which remained at room temperature. The material properties used for each model are given in Table 6.12.

Model	Material Properties
<i>Heat Model</i>	$\kappa = 0.035 \text{ J} / (\text{s} \cdot \text{m} \cdot \text{K})$; $h = 2 \text{ J} / (\text{s} \cdot \text{m}^2 \cdot \text{K})$ $\rho = 1250 \text{ kg} / \text{m}^3$; $c = 1000 \text{ J} / (\text{kg} \cdot \text{K})$;
<i>Mechanics Model</i>	as per Table 6.5, except: $\alpha_T = 0.85 \times 10^{-6} \text{ K}^{-1}$; $\alpha_\omega = 2.0 \times 10^{-3}$
<i>Glass Transition Model</i>	as per Table 6.5

Table 6.12: Material properties used for the multiphysics simulation investigating fatigue behaviour.

Note that some of the material properties have been modified from the previous simulation to suit this fatigue analysis. The thermal conductivity was reduced by a factor of 10 to reduce the heat flux, thereby reducing the convective cooling effect. Further, the coefficient of heat transfer h was reduced from the previous simulation to lower the cooling effect of the surrounding fluid, which now consists of air instead of water, closely matching the parameter used in the simulations by Yu et al. [32].

The simulation was performed for a number of different strain rates with a duration of 5000 cycles. The time step was chosen to capture 20 time increments within each cycle. Four noded tetrahedron elements were used to discretise the three-dimensional domain of the dogbone and three noded triangular elements were used to model the convective boundary interface between the epoxy resin sample and the surrounding fluid for the heat model. Figure 6.16 shows the mesh

used for the fatigue analysis.

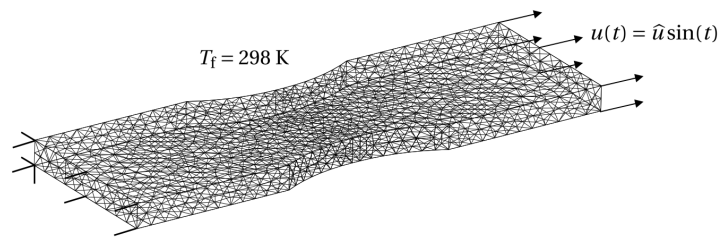


Figure 6.16: 3D mesh used for the fatigue analysis. Dimensions are identical to Figure 6.13, with a thickness of 3 mm. Boundary conditions as per Figure 6.13, except with $\omega_i = 0$ and $T_f = 298 \text{ K}$.

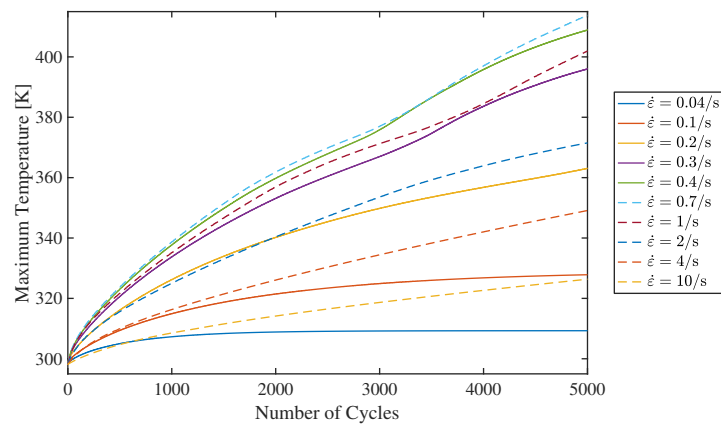


Figure 6.17: Maximum temperature within the epoxy resin specimen vs. number of cycles for varying strain rates.

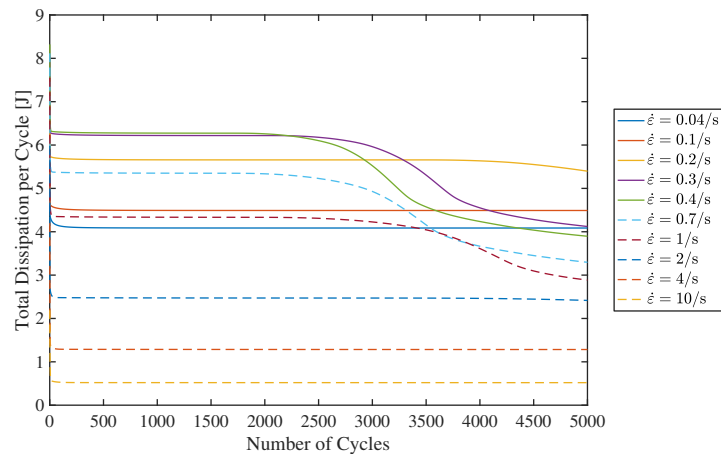


Figure 6.18: Total dissipation per cycle vs. number of cycles for varying strain rates.

All strain rates tested in this simulation resulted in an increase in the temperature of the epoxy resin specimen, see Figure 6.17. For this cyclic multiphysics simulation there are two competing mechanisms that govern the temperature rise of the specimen.

The first mechanism relates to the mechanical deformation of the specimen, which was accompanied by strain rate dependent viscous dissipations. As Figure 6.18 shows, the maximum dissipation per strain cycle occurred for strain rates between 0.3/s and 0.4/s. This is consistent with the

experimental results from Chen et al. [4], in which a peak in the cyclic dissipation did not coincide with the highest strain rate.

In this simulation, strain rates lower than 0.3/s generated a lower amount of dissipation per cycle. This is mainly because smaller strain rates generate a smaller amount of viscoelastic stress, meaning that the stress term in the dissipation equation $\Xi = \sigma \dot{\epsilon}$ is reduced. As Figure 6.18 shows, strain rates above 0.4/s also lead to a reduction in mechanical dissipation per cycle. This is because the hysteresis loop for larger strain rates is smaller due to the lack of stress relaxation, as evidenced in Figure 6.8. Therefore, for one strain cycle a smaller amount of energy is dissipated.

The second competing mechanism is related to the heat loss experienced by the specimen to the surrounding environment. As Figure 6.17 shows, for strain rates below 0.1/s to 0.2/s, a temperature equilibrium is reached. A lower strain rate means that each strain cycle occurs over a longer period of time, resulting in a larger degree of heat loss to the surrounding environment. Therefore, for the temperature of the specimen to continue to rise, more heat needs to be generated through mechanical dissipation than is lost through thermal convection. Even though higher strain rates generate less energy per cycle, this energy outweighs the heat lost to convection in the shorter cycle time.

Figure 6.19 presents the average temperature in the specimen as a function of the number of strain cycles. A notable feature in this figure is the reduction in the temperature gain seen for the strain rates between 0.3/s and 1/s, after approximately 3500 to 4000 cycles. At this stage, the maximum temperature within the sample for these strain rates is well above the glass transition temperature, meaning that a state change has occurred within the material. As a result, this phenomenon coincided with the onset of rubbery behaviour in the centre of the dogbone specimen, resulting in a degradation of the stiffness properties. This degradation of stiffness is consistent with the cyclic softening behaviour observed by Chen et al. and Yu et al. A lower stiffness results in a reduction in mechanical dissipation, explaining the drop in the dissipation per cycle in Figure 6.18 and the reduction in temperature gain in Figure 6.19.

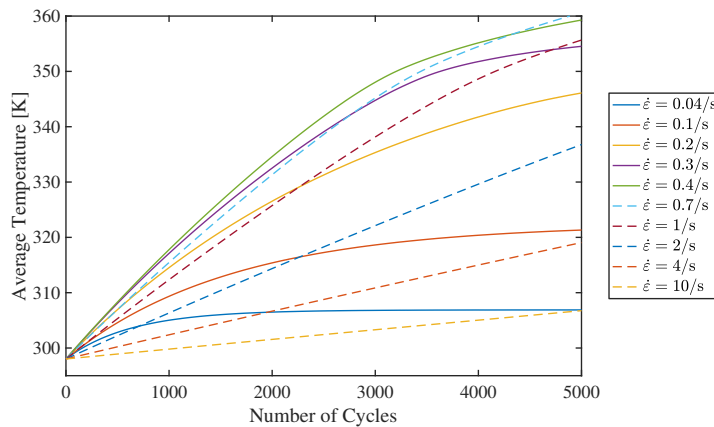


Figure 6.19: Average temperature within the epoxy resin specimen vs. number of cycles for varying strain rates.

To examine the cyclic softening behaviour of the epoxy resin dogbone sample, the results for the strain rate $\dot{\epsilon} = 0.4/s$ are studied in closer detail. Figure 6.20 presents the load displacement response of the epoxy resin specimen for selected load cycles. Figure 6.21 presents the maximum and average values of the temperature and degree of glass transition within the sample as a function of the number of cycles. Figure 6.22 presents contour plots of the temperature, axial stress and degree of glass transition fields within the epoxy resin specimen for selected load steps.

Within the first load cycle the specimen was stressed beyond the yield strength and, as a result, developed plastic strains. This can be seen in the load displacement response in Figure 6.20, as a

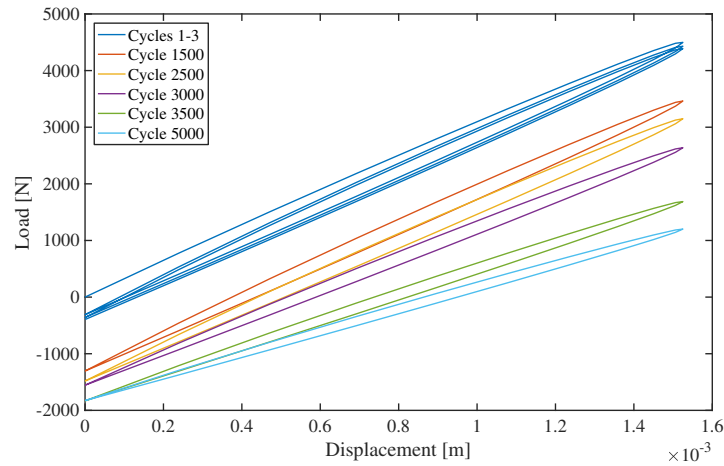


Figure 6.20: Load displacement response of the epoxy resin specimen for $\dot{\epsilon} = 0.4/s$.

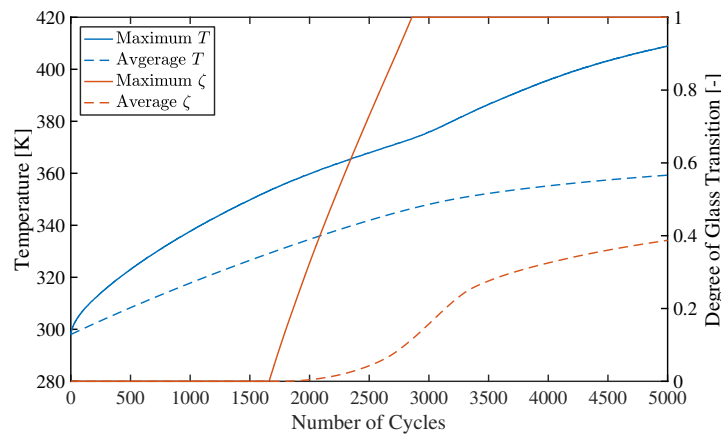


Figure 6.21: Maximum and average values of temperature and degree of glass transition within the epoxy resin specimen vs. number of cycles for $\dot{\epsilon} = 0.4/s$.

significant residual compressive stress was present when the specimen was brought back to a zero displacement for the first time. This plastic strain results in a considerable amount of dissipation within the first few load cycles, see Figure 6.18, which explains the initial fast gain in temperature that can be seen in Figure 6.21. The longitudinal stress distribution during the first cycle is characterised by a stress concentration within the throat of the dogbone sample, see Figure 6.22a.

After the first few cycles, there was almost no further plastic straining and the response was dominated by viscoelasticity, which resulted in a significant stress relaxation until cycle 1500. As Figures 6.21 and 6.22b show, the average temperature of the specimen increased by approximately 25 K, with a temperature increase at the edge of the dogbone of approximately 50 K. As per the provided material properties, the onset of glass transition began at $T_g - 0.5H = 353.3$ K, meaning that the entire specimen was characterised by glassy behaviour. By cycle 1500, the stress concentration that was present in the first cycle expanded to the entire width of the narrowed section, see Figure 6.22b. This was caused by the accumulation of plastic strain at the edges of the section, resulting in a reduction of stiffness in this region.

By cycle 2500, a rubbery state change was well developed at the edges of the dogbone, with the temperature in this region above the glass transition temperature. Figure 6.20 shows no appreciable loss of stiffness at this point. However, from Figure 6.22c it is clear that a redistribution of longitudinal stress has commenced. As the edges of dogbone transition into a mixed glassy-rubbery state

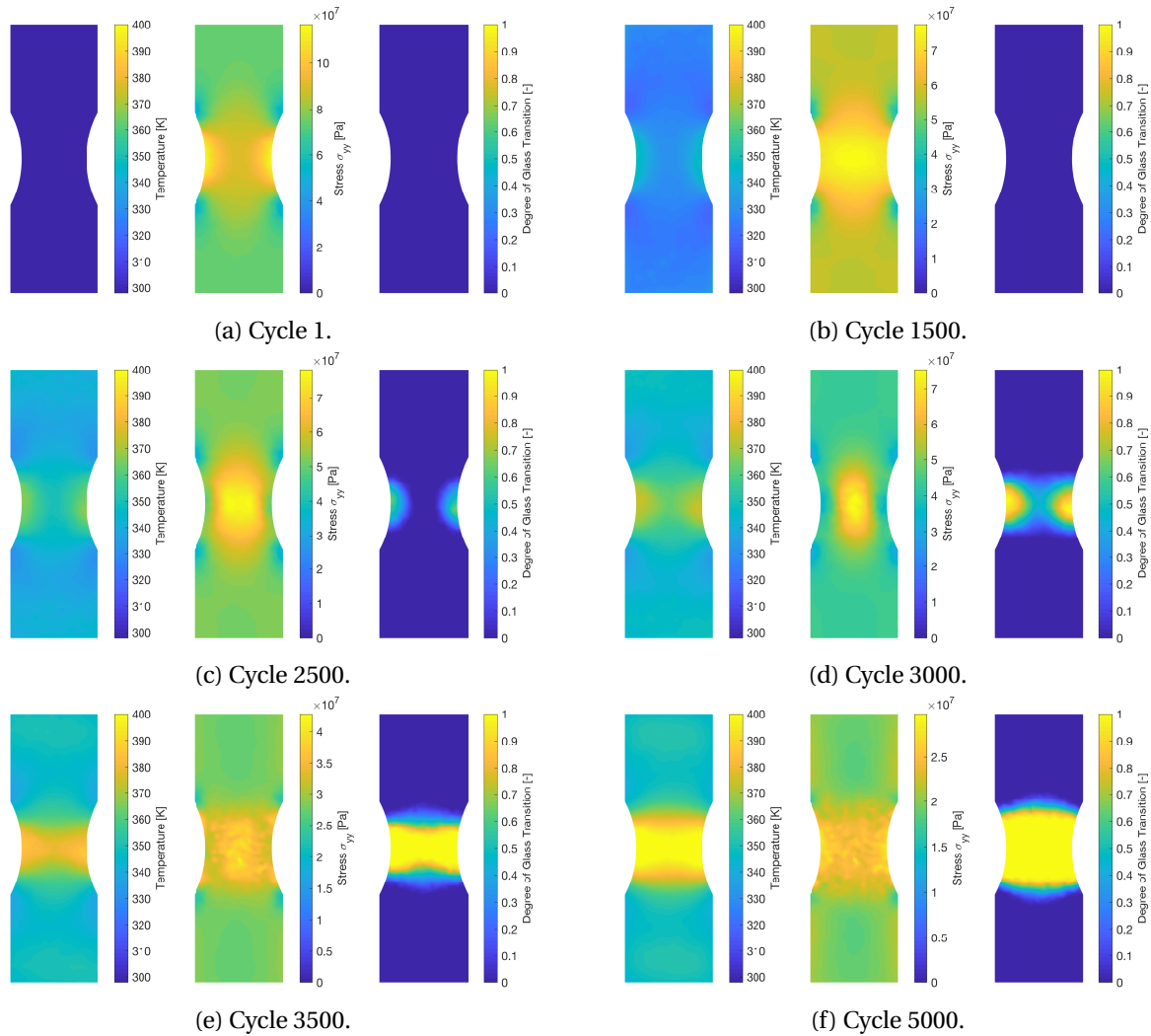


Figure 6.22: Top surface contour plots of the temperature, longitudinal stress σ_{yy} and degree of glass transition for the fatigue analysis.

they lost a significant amount of long term elastic and viscoelastic stiffness. This caused the central region of the dogbone, which was still in a glassy state, to resist a higher proportion of the axial load.

At cycle 3000, the edges of the specimen had completed their transition to a rubbery state and the entire central cross-section of the dogbone was no longer in a glassy state. As Figure 6.21 shows, the average degree of glass transition for the entire specimen was almost 20% resulting in a loss of global structural stiffness. This loss of stiffness can be seen in the load displacement response in Figure 6.20. At this point, the rate of temperature gain began to decrease, due to the reduction in total dissipation seen in Figure 6.18. This reduction of dissipation was caused by the degradation of the viscoelastic stiffnesses, resulting in a diminishing dissipation.

Cycle 3500 saw the entire central cross-section transition to a rubbery state. From Figure 6.22e it is clear that a new stress redistribution was underway as the degraded material properties across the central cross-section approached a new homogenous state. Figure 6.20 shows that the structural stiffness experienced a further reduction and that there occurred a significant stress relaxation between cycle 3000 and 3500. Further, Figure 6.21 shows that the rate of maximum temperature gain within the specimen increased when compared to cycle 3000. This stress relaxation and increase in temperature can be attributed to the development of a local band of plastic strain across the centre of the specimen, see Figure 6.23. The development of plastic strain during this point of the cyclic

test was caused by the significant degradation of the yield strength of the material across the entire width of the section. This stage of the test is the culmination of the cyclic softening effect, which, in reality, may result in structural failure of the specimen. However, as a damage model has not been included in this framework the onset of failure cannot yet be captured.

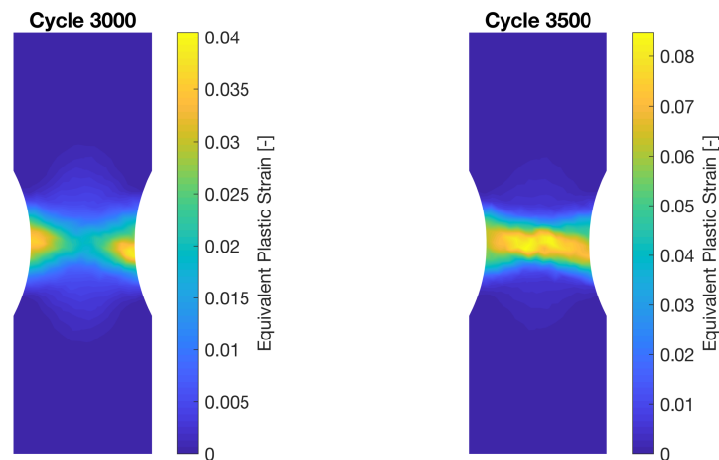


Figure 6.23: Equivalent plastic strain for cycle 3000 and cycle 3500.

By cycle 5000, the rubbery region encapsulated almost the entire throat of the dogbone specimen, resulting in pronounced cyclic softening. This also resulted in a relatively uniform longitudinal stress distribution within the throat of the dogbone specimen. The scattered stress profile in Figure 6.22f can be attributed to the fact that only the top surface of the three dimensional stress field is displayed. Because the mesh consisted of four noded tetrahedron elements, the top surface is made up of both element faces and the apices of other elements, meaning that the interpolated stress field presented at the top surface is impacted by the distribution of elements. The continually declining cyclic energy dissipation led to the development of a plateau in the average temperature of the specimen, see Figure 6.21. If the test were continued further, the degree of glass transition would continue to rise, following the trend in Figure 6.21 and resulting in further reductions in energy dissipation. Eventually, an equilibrium thermal state would be reached in which the dissipated energy balances the heat lost to convection. This would also coincide with an equilibrium in the material state, in which no further glass transitioning would occur.

This fatigue type simulation demonstrates the ability of the developed numerical framework to describe the relevant multiphysical aspects related to the structural performance of epoxy resin. Through an imposed cyclic loading, the numerical model was able to capture the experimentally observed strain rate dependent rise in specimen temperature and resulting cyclic softening. Thus, the numerical framework developed in this thesis has the capacity to model complex problems relating to structural epoxy resins.

6.4. Constitutive Model 2

Two simulations were performed in order to demonstrate how the second constitutive model extends the viscoelasticity model with non-linear effects and how this can be applied to model the observed behaviour of an epoxy resin sample. Both simulations were performed on a three dimensional prismatic model consisting of a single finite element. The first simulation highlights the non-linearity in the viscoelastic model while the second simulation shows how the second constitutive model can be calibrated to experimental data.

6.4.1. Loading-Unloading-Reloading

In this simulation, the response of the first constitutive model is compared to that of the second constitutive model, highlighting the non-linear viscoelastic behaviour. A loading-unloading-reloading test identical to the one performed in Section 6.2.3 was analysed with both constitutive models. The same material properties were used in the Section 6.2.3 are used for this test. However, an extra viscoelastic stiffness was added to emphasise the non-linear behaviour. The material properties used for each constitutive model are described in Table 6.13 below.

Model	Material Properties
<i>Constitutive Model 1</i>	as per Table 6.5 except: $K_4 = 1000 \text{ MPa}$; $\lambda_{4,k} = 10 \text{ s}$ $G_4 = 333.3 \text{ MPa}$; $\lambda_{4,g} = 20 \text{ s}$
	as per Table 6.5 except: $K_4 = 1000 \text{ MPa}$; $\lambda_{4,k} = 10 \text{ s}$ $G_4 = 333.3 \text{ MPa}$; $\lambda_{4,g} = 20 \text{ s}$ $\sigma_0 = 45 \text{ MPa}$; $d_{ve} = 500$; $m_{ve} = 8$ $c_2 = c_3 = 0$

Table 6.13: Material properties used in the non-linear viscoelastic loading-unloading-reloading tests.

Figure 6.24 presents the stress-strain response to the loading-unloading-reloading test for both constitutive models 1 and 2. The response of these models was identical until the stress reached 45 MPa, which coincided with the onset of non-linear viscoelasticity σ_0 , defined in the second constitutive model. After this point, the non-linear model proceeded to soften without developing additional plastic strain. This response matches the observed mechanical behaviour discussed in Section 2.1.1. This reduction in plasticity is evident after the last unloading cycle in which the linear viscoelasticity model displayed a larger residual stress and hence experienced a larger degree of plastic strain.

As a result, this simulation demonstrates the ability of the non-linear viscoelasticity model to overcome the drawback of the linear model, notably the observed softening behaviour that occurs without accompanying plastic strains. When used in conjunction with the glass transition, degradation and multiphysics transport models, the second constitutive model provides a numerical framework that can be used to model the complex behaviour of epoxy resins at both small and large material strains.

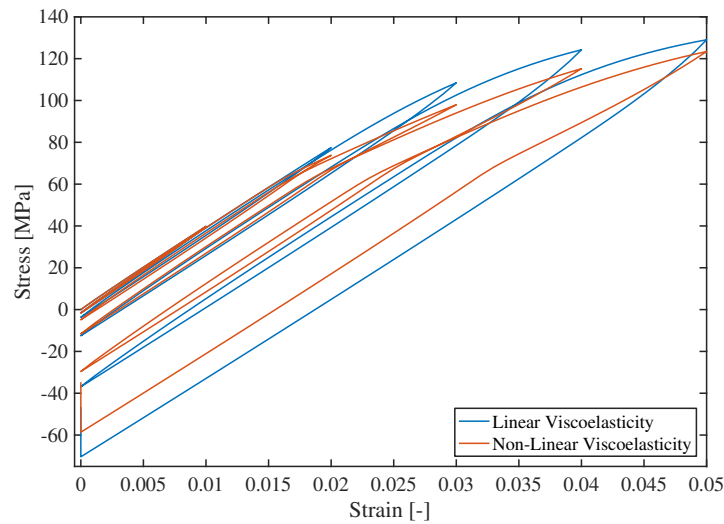


Figure 6.24: Stress-strain response of an epoxy resin sample modelled with constitutive model 1 (linear viscoelasticity) and constitutive model 2 (non-linear viscoelasticity).

6.4.2. Capturing Experimental Behaviour

Results from an experimental loading-unloading-reloading test on an epoxy resin specimen from Rocha et al. [24] were used in this simulation to demonstrate how the second constitutive model can capture the complex material behaviour at larger strains. The experimental data used for this simulation is presented in Figure 6.25. Note that only the data before the peak load was used for the calibration because, after this point, geometrical non-linearity in the form of necking developed during the experimental test.

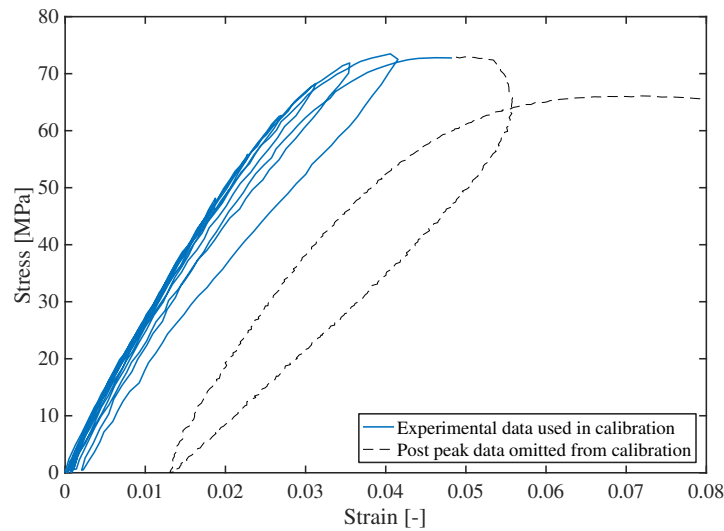


Figure 6.25: Experimental stress-strain response of an epoxy resin sample used for model calibration [24].

The finite element model consisted of a three dimensional single element model loaded in displacement control using the strain values and corresponding time steps from Figure 6.25. Two separate approaches were used to attempt to fit the numerical model to the experimental data. Both approaches attempted to determine the non-linear viscoelastic and viscoplastic parameters that minimised the difference between the experimental data and the corresponding numerical simulation. The following objective function was defined, consisting of a least squares fit between the

numerical results and experimental data:

$$f_{\text{obj}}(\Theta) = \sum_i (\sigma_{\text{exp},i} - \sigma_{\text{num},i}(\Theta))^2 \quad (6.14)$$

where f_{obj} is the objective function to be minimised by the optimisation algorithm, Θ represents the set of relevant material parameters used in the calibration and $\sigma_{\text{exp},i}$ and $\sigma_{\text{num},i}$ are the experimental and numerical stresses at time increment i respectively.

In the first approach, a global optimisation algorithm from the MATLAB optimisation toolbox, *patternsearch*, was used in an attempt to find the global minimum of the objective function, given a reasonable initial starting point. In the second approach, the same optimisation algorithm was used, however, the objective function was evaluated only for specific stress values. Further details regarding the MATLAB optimisation scripts are presented in Appendix C.

The material properties that minimised the least squares error between the experimental and numerical results for the first global optimisation method are presented in Table 6.14 and the resulting stress-strain curve is shown in Figure 6.26.

Model	Property
Viscoelasticity	$E_{\infty} = 1535 \text{ MPa}; \nu_{\infty}^{\text{gl}} = 0$
	$K_i = [82.38 \text{ MPa}, 160.1 \text{ MPa}, 142.4 \text{ MPa}]$
	$G_i = [123.6 \text{ MPa}, 240.2 \text{ MPa}, 213.6 \text{ MPa}]$
	$\lambda_i = [52.44 \times 10^3 \text{ s}, 8.414 \times 10^3 \text{ s}, 4.906 \times 10^3 \text{ s}]$
	$\sigma_0 = 23.96 \text{ MPa}; d_{\text{ve}} = 1.881; m_{\text{ve}} = 4.798$
	$c_2 = 0.125; c_3 = 10.51$
Viscoplasticity	$\sigma_t = \sigma_c = 96.72 - 24.27 \exp(-\varepsilon_{\text{eq}}^p / 0.0405) \text{ MPa}$
	$\eta_p = 0.0294 \text{ MPa} \cdot \text{s}; m_p = 6.625$

Table 6.14: Calibrated non-linear viscoelastic material properties using the first optimisation algorithm.

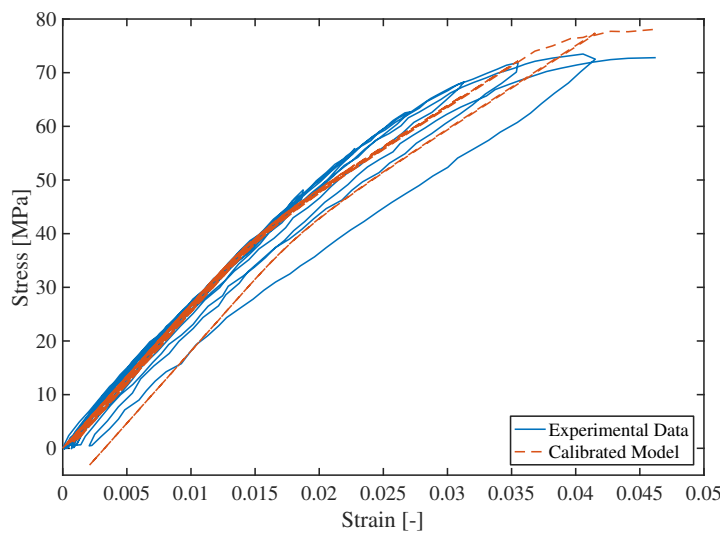


Figure 6.26: Experimental stress-strain response and calibrated numerical model using the first optimisation algorithm.

Figure 6.26 shows that the calibrated model was able to capture the initial elastic behaviour and subsequent softening response above a stress of approximately 40 MPa. Further, it is clear that this softening occurred without any plastic strains and that the only residual strain left at the end of each cycle was due to viscoelastic ratcheting.

However, the model was unable to capture the increasing hysteresis loops that developed after the onset of non-linear viscoelasticity. As a result, the optimisation procedure deferred to an averaging of the loading and unloading responses, meaning that the amount of non-linearity was over-compensated for in the calibration. Further, after the development of plasticity at a stress of 72.5 MPa, the calibrated model curve overshoot the experimental curve. It can therefore be concluded that plasticity did not develop at a fast enough rate.

The second optimisation algorithm was limited to loading branches and stresses above 50 MPa in order to obtain a better fit of the non-linear viscoelastic and viscoplastic parameters. This procedure also better highlights the discrepancy between the numerical and experimental unloading branches because the algorithm was no longer attempting to average the loading and unloading branches. The material properties that minimised the least squares error between the experimental and numerical results for the second global optimisation method are presented in Table 6.15 and the resulting stress-strain curve is shown in Figure 6.27.

Model	Property
<i>Viscoelasticity</i>	$E_{\infty} = 1535 \text{ MPa}; \nu_{\infty}^{\text{gla}} = 0$
	$K_i = [82.38 \text{ MPa}, 160.1 \text{ MPa}, 142.4 \text{ MPa}]$
	$G_i = [123.6 \text{ MPa}, 240.2 \text{ MPa}, 213.6 \text{ MPa}]$
	$\lambda_i = [53.47 \times 10^3 \text{ s}, 9.059 \times 10^3 \text{ s}, 5.455 \times 10^3 \text{ s}]$
	$\sigma_0 = 23.96 \text{ MPa}; d_{\text{ve}} = 1.000; m_{\text{ve}} = 3.100$
	$c_2 = 0.125; c_3 = 11.00$
<i>Viscoplasticity</i>	$\sigma_t = \sigma_c = 82.00 - 20.00 \exp(-\varepsilon_{\text{eq}}^{\text{p}}/0.0397) \text{ MPa}$
	$\eta_{\text{p}} = 0.0294 \text{ MPa} \cdot \text{s}; m_{\text{p}} = 19.21$

Table 6.15: Calibrated non-linear viscoelastic material properties using the second optimisation algorithm.

When compared to the first optimisation procedure, the second optimisation procedure, as summarised in Figure 6.27, showed a much improved fit between the experimental and numerical results. In particular, the loading branches of the numerical simulation almost exactly followed the experimental loading behaviour. Further, there was a good agreement between the experimental and numerical unloading behaviour above the non-linear threshold stress. However, the most significant deviation in the numerical results occurred during unloading, after the stress level fell below the non-linear threshold stress. In the current numerical model, viscoelastic stiffness is regained as g resets to a value of one, below the threshold stress. When this behaviour was compared to the experimental response, it was apparent that the epoxy resin did not completely regain all of its viscoelastic stiffness during unloading. A further complication was that upon reloading, the viscoelastic stiffness appeared to be instantly regained. As a result, the discrepancy between the experimental and numerical behaviour clearly demonstrates the necessity for a non-linear viscoelastic model for epoxy resin to distinguish between loading and unloading behaviour.

The unique unloading behaviour could be attributed to the complex molecular response of the cross-linked polymer chains that are present in epoxy resins. It is clear that, when loaded above a certain stress level, a recoverable softening phenomenon occurs in the deformation of the polymer

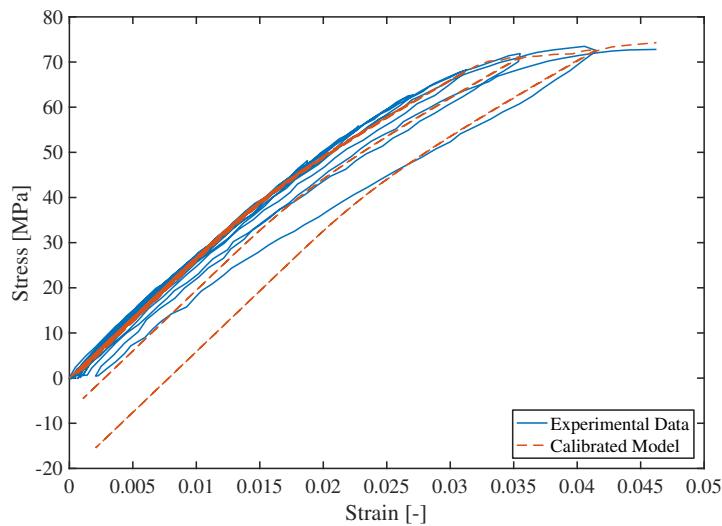


Figure 6.27: Experimental stress-strain response and calibrated numerical model using the second optimisation algorithm.

chains. This softening phenomenon influences the mechanical behaviour of the epoxy resin upon further loading and also during the entire unloading phase. An alternative approach to using a non-linear viscoelastic model to capture this behaviour would be to incorporate a multiscale molecular dynamics model, such as that used by Vu-Bac et al. [30]. Although the scheme would be successful in accurately modelling the complex time and temperature dependent behaviour of epoxy resins, it would also suffer from a significant increase in the computational cost and thus be unfeasible for more complex simulations.

Numerically, the deviation between the non-linear viscoelastic model and the experimental results in the non-linear elastic zone could be attributed to the omission of the memory surface $\mathcal{R}(f)$ in the numerical formulation used in this thesis. The memory surface was recommended by Xia et al. [31] to capture the proper hysteresis behaviour. Developed by Xia et al. and implemented by Yu et al. [32], this memory surface is able to distinguish between loading and unloading and thus can better represent hysteresis effects. It is therefore recommended that the variable unloading behaviour of epoxy resins should be included in further developments of the model used in this thesis. Some recommendations for the implementation of this behaviour are presented in Section 7.2.

Conclusions and Recommendations

7.1. Conclusions

The objective of this thesis was to better quantify the process of hygrothermal ageing in epoxy resins through the development of a constitutive numerical framework. Existing models describing epoxy behaviour by Rocha et al. [24] and Yu et al. [32] were critically analysed and areas for improvement were identified. To further motivate the choices made in the development of the numerical framework, experiments were performed to better ascertain the temperature dependent behaviour of an epoxy resin system. A numerical framework was developed drawing on the work by Rocha et al. and Yu et al. and incorporated thermal and moisture effects, as well as a method to describe non-linear elastic behaviour. Finally, numerical tests were performed using the new model in order to validate the implementation and illustrate the potential of the framework to capture realistic hygrothermal behaviour.

The main findings for each research question are briefly described below.

1. *How well does the existing damage model address the issue of mesh dependency?*

Three mesh dependency studies were performed on the damage model used by Rocha et al. In the original formulation, the effect of plasticity after damage initiation was excessively large. An alternative formulation was therefore pursued in which plasticity was deactivated after damage initiation. The formulation suffered from spurious hardening when a non-zero Poisson's ratio was modelled. However, when a zero Poisson's ratio was modelled, the formulation produced mesh independent results. Further, it was found that a crack band model was required to regularise the damage formulation due to the fact that the viscous components of the model did not provide any significant regularising effects.

2. *How can the existing constitutive model be extended to account for thermal effects?*

A multiphysics framework was developed with the aim of capturing hygrothermal effects. This numerical framework incorporates a heat conduction model, a diffusion model and a mechanics model. The mechanics model implements a glass transition model in order to describe the state of the epoxy resin depending on its temperature and moisture content. The material properties of the epoxy resin are then degraded based on the state of the material. Viscoelasticity and viscoplasticity were also included in the mechanics model in order to capture the time dependent behaviour of epoxy resins.

3. *How can the existing constitutive model be improved to better represent the elastic behaviour at large strains?*

A non-linear viscoelasticity model was formulated to better describe the softening behaviour observed in the elastic range of epoxy resins. The non-linear viscoelasticity model captures effects relating to the stress level, the state of the material and the amount of plastic strain. Further, a return mapping algorithm, integrating coupled non-linear viscoelasticity and viscoplasticity, was developed in order to enable finite element implementation with quadratic convergence.

4. *How well does the new constitutive model capture observed phenomena relating to the mechanical and hygrothermal ageing behaviour of epoxy resins?*

Numerical benchmark tests were performed to validate the individual components of the multiphysics framework, as well as the entire framework as a whole. These tests also served to demonstrate the capabilities of the numerical model in capturing the observed behaviour of epoxy resins. Notably, a fatigue test was performed that illustrated many aspects of the multiphysical behaviour of epoxy resins, such as time dependent mechanical effects, cyclic relaxation and softening, and deformation induced glass transition. Further, the non-linear viscoelastic model was calibrated to experimental data through an optimisation process. Although the non-linear viscoelastic model was able to capture the global experimental behaviour, the precise behaviour could not be fully captured.

5. *What effect does temperature have on the stiffness of the epoxy resin system?*

DMA tests were performed on epoxy resin samples and it was found that the temperature had a significant effect on the stiffness of the material. Three distinctive regimes were identified that relate to a glassy state, a rubbery state and a mixed glassy-rubbery state. The glass transition temperature for the epoxy resin system was determined to be $T_g = 72.7^\circ\text{C}$.

6. *What are the long term stiffness properties of the epoxy resin system in different material states?*

Creep tests were performed on epoxy resin samples in order to determine the long term elastic moduli at three different temperatures that correspond to the three state regimes. It was found that the long term elastic modulus at a temperature of 25°C was 2843 MPa, at 75°C was 51.51 MPa and at 100°C was 17.03 MPa.

7.2. Recommendations

In this section, recommendations for future research and development related to the work in this thesis are discussed.

Damage Model

Although the model produced mesh independent results for materials with a zero Poisson's ratio, spurious hardening was observed for non-zero Poisson's ratios. The inclusion of a degradation of the Poisson's ratio in the damage formulation is therefore recommended in order to obtain a mesh independent model. To further verify the mesh independency of the damage model, additional mesh sensitivity studies are recommended that cover a broader range of mesh dependency issues. Further possible mesh sensitivity studies might include a shear test, an open hole tension test and mesh bias tests.

Multiphysics Model Calibration and Verification

While the developed numerical framework represents a solid foundation for describing the hygrothermal ageing behaviour of epoxy resins, the numerical model still needs to be calibrated with a chosen epoxy resin system in order to properly verify its validity. The experimental work in this thesis has started this process of calibration by determining the dry glass transition temperature and the long term elastic moduli. Further work is required to calibrate the following aspects of the model:

- *Thermal conduction properties:* Material properties related to thermal conduction for the epoxy resin require calibration. Notably the thermal conductivity κ , the coefficient of heat transfer h for different configurations and the specific heat c .
- *Moisture diffusion properties:* Material properties related to moisture diffusion for the epoxy resin require calibration. Notably the diffusivity D_w and its dependence on temperature.
- *Non-linear viscoelastic properties:* This consists of the most involved part of the calibration process owing to the large number of parameters and complexity in behaviour. The non-linear viscoelasticity calibration will require a large number of tests owing to the different deformation time scales and multitude of mechanical effects it captures. Further, its coupling with plasticity means that it will be necessary to isolate viscoelastic strains from viscoplastic strains in some of the calibration tests. Therefore, it is recommended that the viscoelastic strains be allowed to relax after unloading in order to determine the viscoplastic strain. As a result, it is likely that an optimisation procedure similar to the one described in Section 6.4.2, will prove to be the most suitable method for obtaining the material parameters.
- *Viscoplastic properties:* Although calibration of the viscoplastic parameters has already been undertaken by Rocha et al. [24], it will need to be confirmed that these parameters are still valid with the adoption of a coupling non-linear viscoelasticity model.
- *Glass transition properties:* The relative driving force of the moisture content on the glass transition behaviour needs to be determined. The square root relationship between the degree of glass transition and the moisture content should also be verified.

Once model calibration is complete, it is recommended that further tests be performed to verify the results from the calibrated model. The recommended tests will expose the multiphysical and time dependent behaviour of epoxy resins. Possible verification tests include fatigue tests at varying temperatures and moisture contents in order to verify the degraded material properties, cyclic softening and internal heat dissipation. It would be ideal to perform a test that is able to capture

deformation induced glass transition, similar to the numerical study performed in Section 6.3.2. Further, once the model is calibrated it would also be possible to simulate a DMA test, in which the temperature and frequency of the loading is varied.

Currently, the transport and mechanics components of the multiphysics solver are evaluated at every time step. However, in reality the mechanical time scales are often significantly smaller than the transport time scales. In particular, the diffusion of moisture occurs in the order of hours and days, whereas heat conduction and, more significantly, cyclic deformation, operate at time scales of less than a second. This separation of time scales lends itself well to performance improvement techniques such as time homogenisation, which, when implemented, can significantly reduce the computation time for a fatigue analysis.

Finally, it is recommended that this constitutive model be implemented in a multiscale framework incorporating glass fibres and fibre/epoxy interfaces, similar to that developed by Rocha et al. [23]. By improving and expanding the numerical constitutive model for epoxy resins, the hygrothermal behaviour of glass/epoxy composites could thus be better described.

Non-Linear Viscoelasticity Model

While the non-linear viscoelasticity model is currently able to capture non-linear elastic behaviour, it is unable to accurately describe the unloading observed in the experimental data. In the formulation of the non-linear viscoelastic model, the memory surface recommended by Xia et al. [31] was omitted for simplicity. In combination with implementing this feature, it is also proposed to investigate other non-linear viscoelastic formulations in order to ascertain whether or not any improved model behaviour can be integrated into the current numerical framework for epoxy resins.

Some basic modifications to the non-linear viscoelasticity model were made in order to attempt to capture the observed unloading behaviour. Although these attempts were unsuccessful, the following recommendations can be drawn from the lessons learned during this process:

- The original assumption that the non-linear stiffness g was the same for loading and unloading produced unloading behaviour that was too stiff. This approach can be thought of as an upper bound for the unloading stiffness behaviour.
- The simple approach of maintaining a constant value for g during the entire unloading branch does not produce desirable results, as the resulting unloading stiffness was too soft. From examining the experimental behaviour, it is clear that the unloading response is not linear and therefore a linear approximation method cannot sufficiently describe the unloading behaviour. This approach can be thought of as a lower bound for the unloading stiffness behaviour.
- One approach that may yield suitable results would be the definition of a new lower non-linear viscoelastic threshold stress for material unloading. This would delay the onset of stiffening occurring in the unloading behaviour and perhaps produce numerical results that more closely match the experimental response. However, this approach would add another material parameter to an otherwise already complex set of material properties.
- Another possible approach, which does not require the introduction of any further material parameters, would be to define a bilinear unloading response. The proposed response would keep g constant while unloading above the non-linear threshold stress, and then set $g = 1$ for stresses below the non-linear threshold stress. While this model would not be able to represent the exact behaviour of the epoxy resin, it is possible that this approach may give relatively suitable results.

It is recommended that the above modifications be implemented and their suitability assessed with regard to their ability to capture the observed non-linear behaviour of epoxy resins and their

capacity to be calibrated to experimental results.

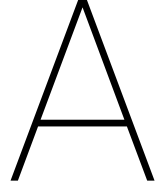
Further, in the current implementation of the return mapping algorithm viscoplasticity is prohibited from occurring before non-linear viscoelasticity. While this is typically a physically consistent assumption, due to the differing forms of the yield functions it is possible that, in a numerical model, a stress state can exist in which plasticity occurs before the onset of non-linear viscoelasticity. As a result, it is also recommended that the return mapping algorithm be extended to include this possibility.

Bibliography

- [1] Holm Altenbach and Wilfried Becker. *Modern trends in composite laminates mechanics*. Springer, Wien, 2003. ISBN 3211203028 9783211203026.
- [2] A Arefi and F. P. van der Meer. Formulation of a consistent pressure-dependent damage model with fracture energy as input. *Unpublished manuscript under review, TU Delft, Delft*, pages 1–26, 2018.
- [3] Hal F. Brinson and L. Catherine Brinson. *Polymer engineering science and viscoelasticity: An introduction*. Springer, 2nd ed. edition, 2015. ISBN 9781489974853. doi: 10.1007/978-1-4899-7485-3.
- [4] Kaijuan Chen, Guozheng Kang, Fucong Lu, Jia Chen, and Han Jiang. Effect of relative humidity on uniaxial cyclic softening/hardening and intrinsic heat generation of polyamide-6 polymer. *Polymer Testing*, 56:19–28, 2016. ISSN 01429418. doi: 10.1016/j.polymertesting.2016.09.020. URL <http://dx.doi.org/10.1016/j.polymertesting.2016.09.020>.
- [5] H S Choi, K J Ahn, J Nam, and H J Chun. Hygroscopic aspects of epoxy / carbon fiber composite laminates in aircraft environments. *Composites Part A: Applied Science and Manufacturing*, 32: 709–720, 2001.
- [6] Robert D. Cook, David S. Malkus, and Michael E. Plesha. *Concepts and applications of finite element analysis*. Wiley, New York, 4th ed. edition, 2002. ISBN 0471356050 9780471356059.
- [7] R. de Borst and L. J. Sluys. *Computational Methods in Non-Linear Solid Mechanics*. Delft University of Technology, Delft, The Netherlands, 2015.
- [8] Kai Dong, Kui Liu, Qian Zhang, Bohong Gu, and Baozhong Sun. Experimental and numerical analyses on the thermal conductive behaviors of carbon fiber/epoxy plain woven composites. *International Journal of Heat and Mass Transfer*, 102:501–517, 2016. ISSN 00179310. doi: 10.1016/j.ijheatmasstransfer.2016.06.035. URL <http://dx.doi.org/10.1016/j.ijheatmasstransfer.2016.06.035>.
- [9] Dynaflow Reseach Group. Jive - Software development kit for advanced numerical simulations., 2017. URL <https://jive.dynaflow.com/>.
- [10] European Wind Energy Association. EU Energy Policy to 2050. Technical report, European Wind Energy Association, Brussels, Belgium, 2011.
- [11] M.G.D. Geers. Viscous regularization of strain localisation for softening materials. Technical Report DCT rapporten; Vol. 1993.090, Technische Universiteit Eindhoven, Eindhoven, 1993.
- [12] Global Wind Energy Council. Global Wind Report 2016. Technical report, Global Wind Energy Council, Brussels, Belgium, 2017. URL <http://files.gwec.net/files/GWR2016.pdf>.
- [13] Yinghui Hu, Augustus W. Lang, Xiaochen Li, and Steven R. Nutt. Hygrothermal aging effects on fatigue of glass fiber/polydicyclopentadiene composites. *Polymer Degradation and Stability*, 110:464–472, 2014. ISSN 01413910. doi: 10.1016/j.polymdegradstab.2014.10.018. URL <http://dx.doi.org/10.1016/j.polymdegradstab.2014.10.018>.

- [14] David E. Keyes, Lois C. McInnes, Carol Woodward, William Gropp, Eric Myra, Michael Pernice, John Bell, Jed Brown, Alain Clo, Jeffrey Connors, Emil Constantinescu, Don Estep, Kate Evans, Charbel Farhat, Ammar Hakim, Glenn Hammond, Glen Hansen, Judith Hill, Tobin Isaac, Xiangmin Jiao, Kirk Jordan, Dinesh Kaushik, Efthimios Kaxiras, Alice Koniges, Kihwan Lee, Aaron Lott, Qiming Lu, John Magerlein, Reed Maxwell, Michael McCourt, Miriam Mehl, Roger Pawlowski, Amanda P. Randles, Daniel Reynolds, Beatrice Rivière, Ulrich Råde, Tim Scheibe, John Shadid, Brendan Sheehan, Mark Shephard, Andrew Siegel, Barry Smith, Xianzhu Tang, Cian Wilson, and Barbara Wohlmuth. Multiphysics simulations: Challenges and opportunities. *International Journal of High Performance Computing Applications*, 27(1):4–83, 2013. ISSN 10943420. doi: 10.1177/1094342012468181.
- [15] E. Kontou. Viscoplastic deformation of an epoxy resin at elevated temperatures. *Journal of Applied Polymer Science*, 101(3):2027–2033, 2006. ISSN 00218995. doi: 10.1002/app.23768.
- [16] Anouar Krairi and Issam Doghri. A thermodynamically-based constitutive model for thermo-plastic polymers coupling viscoelasticity, viscoplasticity and ductile damage. *International Journal of Plasticity*, 60:163–181, 2014. ISSN 07496419. doi: 10.1016/j.ijplas.2014.04.010. URL <http://dx.doi.org/10.1016/j.ijplas.2014.04.010>.
- [17] A. R. Melro, P. P. Camanho, F. M. Andrade Pires, and S. T. Pinho. Micromechanical analysis of polymer composites reinforced by unidirectional fibres: Part I-Constitutive modelling. *International Journal of Solids and Structures*, 50(11-12):1897–1905, 2013. ISSN 00207683. doi: 10.1016/j.ijsolstr.2013.02.009. URL <http://dx.doi.org/10.1016/j.ijsolstr.2013.02.009>.
- [18] Leon Mishnaevsky, Kim Branner, Helga Nørgaard Petersen, Justine Beauson, Malcolm McGugan, and Bent F. Sørensen. Materials for wind turbine blades: An overview. *Materials*, 10(11):1–24, 2017. ISSN 19961944. doi: 10.3390/ma10111285.
- [19] NETZSCH-Geratebau GmbH. *DMA 242 E - Operating Instructions*. NETZSCH-Geratebau, Selb, Germany, 2014.
- [20] I. Özdemir, W. A.M. Brekelmans, and M. G.D. Geers. FE2 computational homogenization for the thermo-mechanical analysis of heterogeneous solids. *Computer Methods in Applied Mechanics and Engineering*, 198(3-4):602–613, 2008. ISSN 00457825. doi: 10.1016/j.cma.2008.09.008. URL <http://dx.doi.org/10.1016/j.cma.2008.09.008>.
- [21] PerkinElmer Inc. Dynamic Mechanical Analysis (DMA). Technical report, PerkinElmer Inc., Waltham, MA, 2008.
- [22] I. B.C.M. Rocha, S. Raijmakers, R. P.L. Nijssen, F. P. van der Meer, and L. J. Sluys. Hygrothermal ageing behaviour of a glass/epoxy composite used in wind turbine blades. *Composite Structures*, 174:110–122, 2017. ISSN 02638223. doi: 10.1016/j.compstruct.2017.04.028.
- [23] I. B.C.M. Rocha, F. P. van der Meer, R. P.L. Nijssen, and L. J. Sluys. A multiscale and multiphysics numerical framework for modelling of hygrothermal ageing in laminated composites. *International Journal for Numerical Methods in Engineering*, 112(4):360–379, 2017. ISSN 10970207. doi: 10.1002/nme.5542.
- [24] I. B.C.M. Rocha, F. P. van der Meer, S. Raijmakers, F. Lahuerta, R. P.L. Nijssen, and L. J. Sluys. A pressure-dependent viscoelastic-viscoplastic model with continuum damage for monotonic and cyclic numerical analysis of epoxy. *Unpublished manuscript under review, TU Delft, Delft*, 2018.

- [25] David Roylance. Engineering Viscoelasticity. Technical report, Department of Materials Science and Engineering, Massachusetts Institute of Technology, 2001. URL <http://web.mit.edu/course/3/3.11/www/modules/visco.pdf>.
- [26] C.-H. Shen and G.S Springer. Environmental Effects on the Elastic Moduli of Composite Materials. *Journal of Composite Materials*, 11:250–264, 1977. ISSN 0021-9983. doi: 10.1177/002199837701100301.
- [27] Strand7 Pty Limited. Strand7 Verification Manual. Technical report, Strand7 Pty Limited, Sydney, Australia, 2013.
- [28] Gang Tao and Zihui Xia. Ratcheting behavior of an epoxy polymer and its effect on fatigue life. *Polymer Testing*, 26(4):451–460, 2007. ISSN 01429418. doi: 10.1016/j.polymertesting.2006.12.010.
- [29] Gang Tao and Zihui Xia. Mean stress/strain effect on fatigue behavior of an epoxy resin. *International Journal of Fatigue*, 29(12):2180–2190, 2007. ISSN 01421123. doi: 10.1016/j.ijfatigue.2006.12.009.
- [30] N. Vu-Bac, M. A. Bessa, Timon Rabczuk, and Wing Kam Liu. A Multiscale Model for the Quasi-Static Thermo-Plastic Behavior of Highly Cross-Linked Glassy Polymers. *Macromolecules*, 48(18):6713–6723, 2015. ISSN 15205835. doi: 10.1021/acs.macromol.5b01236.
- [31] Zihui Xia, Xinghe Shen, and Fernand Ellyin. Cyclic deformation behavior of an epoxy polymer. Part II: Predictions of viscoelastic constitutive models. *Polymer Engineering and Science*, 45(1): 103–113, 2005. ISSN 00323888. doi: 10.1002/pen.20235.
- [32] Chao Yu, Guozheng Kang, and Kaijuan Chen. A hygro-thermo-mechanical coupled cyclic constitutive model for polymers with considering glass transition. *International Journal of Plasticity*, 89:29–65, 2017. ISSN 07496419. doi: 10.1016/j.ijplas.2016.11.001. URL <http://dx.doi.org/10.1016/j.ijplas.2016.11.001>.



Material Model Mathematical Derivations

Derivation of the Non-Linear Viscoelastic Stress Update

The expressions for the volumetric and deviatoric viscoelastic stresses take the following form:

$$\boldsymbol{\sigma}^{\text{ve}}(t) = \sum_{i=1}^N \int_0^t \exp\left(-\frac{t-\tau}{\lambda_i}\right) \frac{df(\boldsymbol{\varepsilon}(\tau), \tau)}{d\tau} d\tau \quad (\text{A.1})$$

where $f(\boldsymbol{\varepsilon}(\tau), \tau)$ is defined differently for the volumetric and deviatoric stresses:

$$f_v(\boldsymbol{\varepsilon}(\tau), \tau) = \frac{K_i(\tau)}{g(\tau)} \varepsilon_v(\tau) \quad (\text{A.2a})$$

$$f_d(\boldsymbol{\varepsilon}(\tau), \tau) = \frac{2G_i(\tau)}{g(\tau)} \boldsymbol{\varepsilon}_d(\tau) \quad (\text{A.2b})$$

Equation A.1 involves an integral over the entire loading history and therefore is computationally cumbersome. This expression for the viscoelastic strain can be elaborated to arrive at a discretised expression for the viscoelastic strain increment. First, the integration limits are divided into two parts, the first from $\tau = 0$ to $\tau = t - \Delta t$ and the second from $\tau = t - \Delta t$ to $\tau = t$:

$$\boldsymbol{\sigma}^{\text{ve}}(t) = \sum_{i=1}^N \left\{ \int_0^{t-\Delta t} \exp\left(-\frac{t-\tau}{\lambda_i}\right) \frac{df(\boldsymbol{\varepsilon}(\tau), \tau)}{d\tau} d\tau + \int_{t-\Delta t}^t \exp\left(-\frac{t-\tau}{\lambda_i}\right) \frac{df(\boldsymbol{\varepsilon}(\tau), \tau)}{d\tau} d\tau \right\} \quad (\text{A.3})$$

Subtracting an expression for the viscoelastic stress at the previous time step,

$$\boldsymbol{\sigma}^{\text{ve}}(t - \Delta t) = \sum_{i=1}^N \int_0^{t-\Delta t} \exp\left(-\frac{t-\Delta t-\tau}{\lambda_i}\right) \frac{df(\boldsymbol{\varepsilon}(\tau), \tau)}{d\tau} d\tau \quad (\text{A.4})$$

from both sides of Equation A.3 results in the following viscoelastic stress increment:

$$\Delta \boldsymbol{\sigma}^{\text{ve}} = \sum_{i=1}^N \left\{ \int_0^{t-\Delta t} \left[\exp\left(-\frac{t-\tau}{\lambda_i}\right) - \exp\left(-\frac{t-\Delta t-\tau}{\lambda_i}\right) \right] \frac{df(\boldsymbol{\varepsilon}(\tau), \tau)}{d\tau} d\tau + \int_{t-\Delta t}^t \exp\left(-\frac{t-\tau}{\lambda_i}\right) \frac{df(\boldsymbol{\varepsilon}(\tau), \tau)}{d\tau} d\tau \right\} \quad (\text{A.5})$$

$$\therefore \Delta \boldsymbol{\sigma}^{\text{ve}} = \sum_{i=1}^N \left\{ \int_0^{t-\Delta t} \left[\exp\left(-\frac{t-\Delta t-\tau}{\lambda_i}\right) \exp\left(-\frac{\Delta t}{\lambda_i}\right) - \exp\left(-\frac{t-\Delta t-\tau}{\lambda_i}\right) \right] \frac{df(\boldsymbol{\varepsilon}(\tau), \tau)}{d\tau} d\tau + \int_{t-\Delta t}^t \exp\left(-\frac{t-\tau}{\lambda_i}\right) \frac{df(\boldsymbol{\varepsilon}(\tau), \tau)}{d\tau} d\tau \right\} \quad (\text{A.6})$$

$$\therefore \Delta \boldsymbol{\sigma}^{\text{ve}} = \sum_{i=1}^N \left\{ -\left(1 - \exp\left(-\frac{\Delta t}{\lambda_i}\right)\right) \int_0^{t-\Delta t} \exp\left(-\frac{t-\Delta t-\tau}{\lambda_i}\right) \frac{df(\boldsymbol{\varepsilon}(\tau), \tau)}{d\tau} d\tau + \int_{t-\Delta t}^t \exp\left(-\frac{t-\tau}{\lambda_i}\right) \frac{df(\boldsymbol{\varepsilon}(\tau), \tau)}{d\tau} d\tau \right\} \quad (\text{A.7})$$

Noting that:

$$\sum_{i=1}^N \int_0^{t-\Delta t} \exp\left(-\frac{t-\Delta t-\tau}{\lambda_i}\right) \frac{df(\boldsymbol{\varepsilon}(\tau), \tau)}{d\tau} d\tau = \boldsymbol{\sigma}^{\text{ve}}(t-\Delta t) \quad (\text{A.8})$$

Equation A.7 becomes:

$$\Delta \boldsymbol{\sigma}^{\text{ve}} = \sum_{i=1}^N \left\{ \int_{t-\Delta t}^t \exp\left(-\frac{t-\tau}{\lambda_i}\right) \frac{df(\boldsymbol{\varepsilon}(\tau), \tau)}{d\tau} d\tau - \left[1 - \exp\left(-\frac{\Delta t}{\lambda_i}\right)\right] \boldsymbol{\sigma}_i^{\text{ve}}(t-\Delta t) \right\} \quad (\text{A.9})$$

Assuming that the function $f(\boldsymbol{\varepsilon}(\tau), \tau)$ is constant over the time step:

$$\frac{df(\boldsymbol{\varepsilon}(\tau), \tau)}{d\tau} \approx \frac{\Delta f(\boldsymbol{\varepsilon}(t^*), t^*)}{\Delta t} \quad (\text{A.10})$$

with $t - \Delta t \leq t^* \leq t$, the integral in Equation A.9 can be evaluated in a semi-analytical manner:

$$\Delta \boldsymbol{\sigma}^{\text{ve}} = \sum_{i=1}^N \left\{ \frac{\Delta f(\boldsymbol{\varepsilon}(t^*), t^*) \lambda_i}{\Delta t} \exp\left(-\frac{t-\tau}{\lambda_i}\right) \Big|_{\tau=t-\Delta t}^{\tau=t} - \left[1 - \exp\left(-\frac{\Delta t}{\lambda_i}\right)\right] \boldsymbol{\sigma}_i^{\text{ve}}(t-\Delta t) \right\} \quad (\text{A.11})$$

$$\therefore \Delta \boldsymbol{\sigma}^{\text{ve}} = \sum_{i=1}^N \left[\left[1 - \exp\left(-\frac{\Delta t}{\lambda_i}\right)\right] \left(\frac{\Delta f(\boldsymbol{\varepsilon}(t^*), t^*) \lambda_i}{\Delta t} - \boldsymbol{\sigma}_i^{\text{ve}}(t-\Delta t) \right) \right] \quad (\text{A.12})$$

Viscoplastic Consistent Tangent Stiffness Matrix

The derivation of the viscoplastic algorithmic tangent is based on the procedure detailed by Rocha et al. [24] and is briefly reproduced here. The derivation begins by differentiating the expression for the stress in Equation 5.62a with respect to the strain:

$$\frac{\partial \boldsymbol{\sigma}}{\partial \boldsymbol{\varepsilon}} = \frac{1}{\zeta_s} \frac{\partial \mathbf{S}^{\text{tr}}}{\partial \boldsymbol{\varepsilon}} - \frac{6\widehat{G}}{\zeta_s^2} \mathbf{S}^{\text{tr}} \frac{\partial \Delta \gamma}{\partial \boldsymbol{\varepsilon}} + \frac{1}{3\zeta_p} \delta_{ij} \frac{\partial I_1^{\text{tr}}}{\partial \boldsymbol{\varepsilon}} - \frac{2\widehat{K}\alpha I_1^{\text{tr}}}{\partial \boldsymbol{\varepsilon}} \delta_{ij} \frac{\partial \Delta \gamma}{\partial \boldsymbol{\varepsilon}} \quad (\text{A.13})$$

where δ_{ij} is the Kronecker delta. The derivatives of the trial deviatoric stress vector and the first trial stress invariant are given by:

$$\frac{\partial \mathbf{S}^{\text{tr}}}{\partial \boldsymbol{\varepsilon}} = \widehat{G} \left(\mathbf{I} - \frac{2}{3} \mathbf{1} \otimes \mathbf{1} \right) \quad (\text{A.14a})$$

$$\frac{\partial I_1^{\text{tr}}}{\partial \boldsymbol{\varepsilon}} = 3\widehat{K} \delta_{ij} \quad (\text{A.14b})$$

where \mathbf{I} is the fourth order identity tensor and I is the second order identity tensor. The variation of plastic multiplier with respect to the strain comes from the definition of the return mapping function in Equation 5.64:

$$\delta\Phi = \frac{\partial\Phi}{\partial\boldsymbol{\varepsilon}}\delta\boldsymbol{\varepsilon} + \frac{\partial\Phi}{\partial\Delta\gamma}\delta\Delta\gamma = 0 \Rightarrow \frac{\partial\Delta\gamma}{\partial\boldsymbol{\varepsilon}} = -\frac{\partial\Phi}{\partial\Delta\gamma}\frac{\partial\Phi}{\partial\boldsymbol{\varepsilon}} = \mu\frac{\partial\Phi}{\partial\boldsymbol{\varepsilon}} \quad (\text{A.15})$$

where the derivative of Φ with respect to $\Delta\gamma$ has been determined for the return mapping algorithm, see Section 5.4.6.3. Differentiation of Φ with respect to the strain takes a form similar to Equation 5.93:

$$\frac{\partial\Phi}{\partial\boldsymbol{\varepsilon}} = \frac{m_p\Delta t}{\eta_p\sigma_t^0\sigma_c^0}\left(\frac{f_p}{\sigma_t^0\sigma_c^0}\right)^{m_p-1}\frac{\partial f_p}{\partial\boldsymbol{\varepsilon}} = \hat{V}\frac{\partial f_p}{\partial\boldsymbol{\varepsilon}} \quad (\text{A.16})$$

where the derivative of f_p with respect to the strain is given by:

$$\frac{\partial f_p}{\partial\boldsymbol{\varepsilon}} = \frac{6}{\zeta_s^2}\frac{\partial J_2^{\text{tr}}}{\partial\boldsymbol{\varepsilon}} + \frac{2(\sigma_c - \sigma_t)}{\zeta_p}\frac{\partial I_1^{\text{tr}}}{\partial\boldsymbol{\varepsilon}} + \frac{\partial f_p}{\partial\varepsilon_{\text{eq}}^p}\frac{\partial\varepsilon_{\text{eq}}^p}{\partial\boldsymbol{\varepsilon}} \quad (\text{A.17})$$

where the derivative of f_p with respect to the equivalent plastic strain is given in Equation 5.92 and redefined here as \hat{H} . The derivative of the first invariant with respect to the strain is given in Equation A.14b and the derivative of J_2^{tr} is given by:

$$\frac{\partial J_2^{\text{tr}}}{\partial\boldsymbol{\varepsilon}} = \mathbf{S}^{\text{tr}}\frac{\partial\mathbf{S}^{\text{tr}}}{\partial\boldsymbol{\varepsilon}} = 2\hat{G}\mathbf{S}^{\text{tr}} \quad (\text{A.18})$$

The last term to evaluate is the derivative of the equivalent plastic strain with respect to the strain:

$$\frac{\partial\varepsilon_{\text{eq}}^p}{\partial\boldsymbol{\varepsilon}} = \frac{1}{1+2\nu_p^2}\frac{(\Delta\gamma)^2}{\Delta\varepsilon_{\text{eq}}^p}\left(\frac{3\mathbf{S}^{\text{tr}}}{\zeta_s} + \frac{2\alpha I_1^{\text{tr}}\delta_{ij}}{9\zeta_p}\right)\left(\frac{\hat{G}}{\zeta_s}(3\mathbf{I} - 2 \cdot I \otimes I) + \frac{2\hat{K}\alpha}{3\zeta_p}I \otimes I\right) = \hat{\mathbf{E}} \quad (\text{A.19})$$

As a result, the consistent tangent stiffness matrix can be written as:

$$\frac{\partial\boldsymbol{\sigma}}{\partial\boldsymbol{\varepsilon}} = \beta\mathbf{I} + \left(\phi - \frac{\beta}{3}\right)I \otimes I - \rho\mathbf{S}^{\text{tr}}\delta_{ij} - \chi\mathbf{S}^{\text{tr}}\mathbf{S}^{\text{tr}} - \psi\mathbf{S}^{\text{tr}}\delta_{ij} - \omega\mathbf{S}^{\text{tr}}\hat{\mathbf{E}} - \xi\hat{\mathbf{E}}\delta_{ij} \quad (\text{A.20})$$

where the following coefficients are defined for this section only as:

$$\begin{aligned} \beta &= \frac{2\hat{G}}{\zeta_s} & \phi &= \frac{\hat{K}}{\zeta_p} - \frac{4\alpha I_1^{\text{tr}}(\sigma_c - \sigma_t)\hat{V}\hat{K}^2}{\mu\zeta_p^3} \\ \rho &= \frac{36(\sigma_c - \sigma_t)\hat{V}\hat{K}\hat{G}}{\mu\zeta_p\zeta_s^2} & \chi &= \frac{72\hat{V}\hat{G}^2}{\mu\zeta_s^4} \\ \psi &= \frac{8\alpha I_1^{\text{tr}}\hat{V}\hat{K}\hat{G}}{\mu\zeta_p^2\zeta_s^2} & \omega &= \frac{6\hat{V}\hat{G}\hat{H}}{\mu\zeta_s^2} & \xi &= \frac{2\alpha I_1^{\text{tr}}\hat{V}\hat{K}\hat{H}}{3\mu\zeta_p^2} \end{aligned} \quad (\text{A.21})$$

Coupled Return Mapping Algorithm Derivatives

In this section, derivatives further to those derived in Section 5.4.6 are computed.

The following relates to the derivatives of the first stress invariant calculated in Equations 5.78a and 5.78b:

$$\frac{\partial I_1^{\text{tr}}(g)}{\partial g} = 3 \frac{\partial \Delta p^{\text{ve}}(g)}{\partial g} = -3 \sum_{i=1}^N \left[1 - \exp\left(-\frac{\Delta t}{\lambda_i}\right) \right] \left(\frac{K_i(t) \lambda_i \Delta \varepsilon_v^e}{g(\boldsymbol{\sigma}, \zeta, \varepsilon_{\text{eq}}^p)^2 \Delta t} \right) \quad (\text{A.22a})$$

$$\frac{\partial \zeta_p(g, \Delta \gamma)}{\partial g} = 2\alpha \Delta \gamma \frac{\partial K_{\text{ve}}(g)}{\partial g} = -2\alpha \Delta \gamma \sum_{i=1}^N \left[1 - \exp\left(-\frac{\Delta t}{\lambda_i}\right) \right] \left(\frac{K_i(t) \lambda_i}{g(\boldsymbol{\sigma}, \zeta, \varepsilon_{\text{eq}}^p)^2 \Delta t} \right) \quad (\text{A.22b})$$

$$\frac{\partial \zeta_p(g, \Delta \gamma)}{\partial \Delta \gamma} = 2\hat{K}(g)\alpha \quad (\text{A.22c})$$

The following relates to the derivatives of the second deviatoric stress invariant calculated in Equations 5.78c and 5.78d:

$$\frac{\partial J_2^{\text{tr}}(g)}{\partial g} = \frac{\partial J_2^{\text{tr}}}{\partial \mathbf{S}^{\text{tr}}} \cdot \frac{\partial \mathbf{S}^{\text{tr}}(g)}{\partial g} = \frac{\partial J_2^{\text{tr}}}{\partial \mathbf{S}^{\text{tr}}} \cdot \frac{\partial \Delta \mathbf{S}^{\text{ve}}(g)}{\partial g} = -\mathbf{S}^{\text{tr}} \cdot \sum_{i=1}^N \left[1 - \exp\left(-\frac{\Delta t}{\lambda_i}\right) \right] \left(\frac{2G_i(t) \lambda_i \Delta \varepsilon_d^e}{g(\boldsymbol{\sigma}, \zeta, \varepsilon_{\text{eq}}^p)^2 \Delta t} \right) \quad (\text{A.23a})$$

$$\frac{\partial \zeta_s(g, \Delta \gamma)}{\partial g} = 6\Delta \gamma \frac{\partial G_{\text{ve}}(g)}{\partial g} = -6\Delta \gamma \sum_{i=1}^N \left[1 - \exp\left(-\frac{\Delta t}{\lambda_i}\right) \right] \left(\frac{G_i(t) \lambda_i}{g(\boldsymbol{\sigma}, \zeta, \varepsilon_{\text{eq}}^p)^2 \Delta t} \right) \quad (\text{A.23b})$$

$$\frac{\partial \zeta_s(g, \Delta \gamma)}{\partial \Delta \gamma} = 6\hat{G}(g) \quad (\text{A.23c})$$

The following relates to the derivatives of the equivalent plastic strain calculated in Equations 5.80a and 5.80b.

$$\frac{\partial \hat{A}(g, \Delta \gamma)}{\partial g} = \frac{18}{\zeta_s(g, \Delta \gamma)^2} \frac{\partial J_2^{\text{tr}}(g)}{\partial g} - \frac{216\Delta \gamma J_2^{\text{tr}}(g)}{\zeta_s(g, \Delta \gamma)^3} \frac{\partial G_{\text{ve}}(g)}{\partial g} + \frac{8\alpha^2 I_1^{\text{tr}}(g)}{27\zeta_p(g, \Delta \gamma)^2} \frac{\partial I_1^{\text{tr}}(g)}{\partial g} - \frac{16\alpha^3 \Delta \gamma I_1^{\text{tr}}(g)^2}{27\zeta_p(g, \Delta \gamma)^3} \frac{\partial K_{\text{ve}}(g)}{\partial g} \quad (\text{A.24})$$

$$\frac{\partial \Delta \varepsilon_{\text{eq}}^p(g, \Delta \gamma)}{\partial \Delta \gamma} = \sqrt{\frac{1}{1+2\nu_p^2}} \left[\sqrt{\hat{A}(g, \Delta \gamma)} + \Delta \gamma \frac{\partial}{\partial \Delta \gamma} \left(\sqrt{\hat{A}(g, \Delta \gamma)} \right) \right] \quad (\text{A.25})$$

$$= \sqrt{\frac{1}{1+2\nu_p^2}} \left[\sqrt{\hat{A}(g, \Delta \gamma)} + \frac{\Delta \gamma}{2\sqrt{\hat{A}(g, \Delta \gamma)}} \frac{\partial \hat{A}(g, \Delta \gamma)}{\partial \Delta \gamma} \right] \quad (\text{A.26})$$

with:

$$\frac{\partial \hat{A}(g, \Delta \gamma)}{\partial \Delta \gamma} = 18 J_2^{\text{tr}}(g) \frac{-2}{\zeta_s(g, \Delta \gamma)^3} \frac{\partial \zeta_s(g, \Delta \gamma)}{\partial \Delta \gamma} + \frac{4\alpha^2 I_1^{\text{tr}}(g)^2}{27} \frac{-2}{\zeta_p(g, \Delta \gamma)^3} \frac{\partial \zeta_p(g, \Delta \gamma)}{\partial \Delta \gamma} \quad (\text{A.27a})$$

$$= -\frac{216\hat{G}(g) J_2^{\text{tr}}(g)}{\zeta_s(g, \Delta \gamma)^3} - \frac{16\alpha^3 \hat{K}(g) I_1^{\text{tr}}(g)^2}{27\zeta_p(g, \Delta \gamma)^3} \quad (\text{A.27b})$$

B

Jive Implementation of the Constitutive Model

Constitutive Model

The *update* method used by the finite element implementation to form the constitutive matrix \mathbf{D} and internal force vector \mathbf{f} , and calculate the mechanical dissipation Ξ , is presented in Algorithm 1.

Box B.1: Constitutive Model Update Method

Algorithm 1 Constitutive Model Update Method

Require: $\mathcal{E}(t), T(t), \omega(t), \Delta t$

- 1: $\zeta \leftarrow \text{COMPUTEZETA}(T, \omega)$ ▷ Equation 5.31
 - 2: $\mathbf{D}_\infty(\zeta) \leftarrow \text{COMPUTELONGTERMD}(E_\infty^{\text{gla}}, E_\infty^{\text{rub}}, \nu_\infty^{\text{gla}}, \nu_\infty^{\text{rub}}, \zeta)$ ▷ Equation 5.42
 - 3: $K_i(\zeta), G_i(\zeta) \leftarrow \text{COMPUTEVESTIFFS}(K_i^{\text{gla}}, K_i^{\text{rub}}, G_i^{\text{gla}}, G_i^{\text{rub}}, \zeta)$ ▷ Equations 5.40a and 5.40b
 - 4: $\boldsymbol{\varepsilon} \leftarrow \text{COMPUTEMECHSTRAIN}(\mathcal{E}, T, \alpha_T, \omega, \alpha_\omega)$ ▷ Equation 5.95
 - 5: $\Lambda \boldsymbol{\sigma}^{\text{ve}}(t - \Delta t) \leftarrow \text{DECAYVESTRESS}(\boldsymbol{\sigma}^{\text{ve}}(t - \Delta t), \Delta t)$ ▷ Equation 5.72
 - 6: $\mathbf{g}, \Delta \gamma \leftarrow \text{COUPLED RM}$ ▷ Algorithm 2
 - 7: $\boldsymbol{\sigma} \leftarrow \text{EVALUATESTRESS}$ ▷ Equation 5.75
 - 8: $\mathbf{D} \leftarrow \text{EVALUATE TANGENT}$ ▷ Equation A.20
 - 9: $\Xi \leftarrow \text{EVALUATE DISSIPATION}$ ▷ Equations 5.54 and 5.67
-

Coupled Return Mapping Algorithm

The main function used to solve the coupled non-linear viscoelasticity and viscoplasticity problem is presented in Algorithm 2. The return mapping algorithms that solve the single variable problem and the coupled problem are presented in Algorithms 3 and 4 respectively.

Box B.2: Coupled Return Mapping Algorithm

Algorithm 2 Return Mapping Function**Require:** $\boldsymbol{\varepsilon}(t)$, $\Delta\boldsymbol{\varepsilon}$, $\boldsymbol{\varepsilon}^p(t - \Delta t)$, $\boldsymbol{\varepsilon}_{\text{eq}}^p(t - \Delta t)$, $\mathbf{D}_\infty(t)$, $\Lambda\boldsymbol{\sigma}^{\text{ve}}(t - \Delta t)$, Δt

- 1: Compute initial elastic strains: $\boldsymbol{\varepsilon}_0^e(t)$, $\Delta\boldsymbol{\varepsilon}_0^e$ ▷ Equations 5.70e and 5.70f
- 2: Compute the initial trial stress: $\boldsymbol{\sigma}_0^{\text{tr}}$ ▷ Equation 5.74
- 3: Evaluate f_{ve} ▷ Equation 5.56
- 4: **if** $f_{\text{ve}} \leq 1$ **then**
- 5: Evaluate f_p ▷ Equation 5.60a
- 6: **if** $f_p > 0$ **then**
- 7: **return** Error: Plasticity occurs before non-linear viscoelasticity.
- 8: **else**
- 9: **return** $g = 1$; $\Delta\gamma = 0$
- 10: **else**
- 11: $g_k \leftarrow \text{SOLVEG}$ ▷ Algorithm 3
- 12: Evaluate f_p ▷ Equation 5.60a
- 13: **if** $f_p > 0$ **then**
- 14: $g_k, \Delta\gamma_k \leftarrow \text{SOLVECOUPLED}$ ▷ Algorithm 4
- 15: **return** $g = g_k$; $\Delta\gamma = \Delta\gamma_k$
- 16: **else**
- 17: **return** $g = g_k$; $\Delta\gamma = 0$

Algorithm 3 Non-Linear Viscoelasticity Return Mapping Algorithm

- 1: **function** SOLVEG
- 2: **for** $k = 1$ **to** maxIt **do**
- 3: Evaluate Γ_k ▷ Equation 5.68a
- 4: **if** $|\Gamma_k| < \Gamma_{\text{tol}}$ **then**
- 5: **return** $g = g_k$
- 6: **else**
- 7: Evaluate $\frac{\partial \Gamma_k}{\partial g}$ ▷ Equation 5.81
- 8: $g_{k+1} = g_k - \left(\frac{\partial \Gamma_k}{\partial g}\right)^{-1} \Gamma_k$
- 9: Update strains: $\boldsymbol{\varepsilon}_{k+1}^p$, $\boldsymbol{\varepsilon}_{\text{eq},k+1}^p$, $\boldsymbol{\varepsilon}_{k+1}^e$, $\Delta\boldsymbol{\varepsilon}_{k+1}^e$ ▷ Equations 5.70a to 5.70f
- 10: Update trial stress: $\boldsymbol{\sigma}_{k+1}^{\text{tr}}$ ▷ Equation 5.74

Algorithm 4 Non-Linear Viscoelasticity and Plasticity Return Mapping Algorithm

```

1: function SOLVECOUPLED
2:   for  $k = 1$  to maxIt do
3:     Evaluate  $\Gamma_k$  and  $\Phi_k$                                 ▷ Equations 5.68a and 5.68b
4:     if  $|\Gamma_k| < \Gamma_{tol}$  and  $|\Phi_k| < \Phi_{tol}$  then
5:       return  $g = g_k; \Delta\gamma = \Delta\gamma_k$ 
6:     else
7:       Evaluate Jacobian Matrix                                ▷ Equation 5.69
8:       Update  $g_{k+1}$  and  $\Delta\gamma_{k+1}$                        ▷ Equation 5.69
9:       Update strains:  $\boldsymbol{\epsilon}_{k+1}^p, \boldsymbol{\epsilon}_{eq,k+1}^p, \boldsymbol{\epsilon}_{k+1}^e, \Delta\boldsymbol{\epsilon}_{k+1}^e$     ▷ Equations 5.70a to 5.70f
10:      Update trial stress:  $\boldsymbol{\sigma}_{k+1}^{tr}$                     ▷ Equation 5.74
11:      Update current stress:  $\boldsymbol{\sigma}_{k+1}$                        ▷ Equation 5.75

```


C

MATLAB Optimisation Script for Model Calibration

This section presents the MATLAB scripts used for the calibration of experimental results to the couple non-linear viscoelastic and viscoplastic model. The relevant properties used by the finite element implementation are also presented.

First Global Optimisation Method

Listing C.1 presents the MATLAB script used for the first global optimisation method. First, the experimental data is loaded and the parameters for the optimisation set. Note that a Poisson's ratio of $\nu_\infty = 0$ and correspondingly, $G_i = 1.5K_i$ and $\lambda_{i,k} = \lambda_{i,g}$ were used for the calibration in order to reduce the number of unknowns. The function *loadMaterialProperties* sets the user defined initial value *x0*, lower bound *lb* and upper bound *ub*. This function is presented in Listing C.3. The constraints *A* and *b* are set to ensure that non-linear viscoelasticity occurs before viscoplasticity. This inequality constraint ensures that the yield stress is always above the upper bound of the onset of non-linear viscoelasticity. The *patternsearch* algorithm then begins, using the objective function *objFun*, which is presented in Listing C.2. Note that the function defined as *myOutputFunction* is used to write the minimised material property for each iteration to a .mat file so that the algorithm can be terminated at any point without losing the results.

The finite element program is run with a time increment of $\Delta t = 0.1$ s and with imposed displacements based on the strains recorded from the experimental data. One eight noded hexahedron element is used to model the bar. Only one Gauss point is required for numerical integration due to the constant strain state within the element. This greatly improves the computational performance of the algorithm.

Listing C.1: First Global Optimisation Script

```
1 %% Load experimental data and set initial properties and bounds
2 clear; clc; close all;
3
4 % load raw experimental data
5 data = dlmread('3352_45_prepeak.plot', ' ', 1, 0);
6
7 % define the experimental range over which calibration occurs
8 endIndex = 512;
9 nu = 0.0; % poissons ratio
10
```

```

11 t_exp = data(:,1); % experimental times
12 tmax = t_exp(endIndex); % final time
13 stry_exp = data(:,3); % experimental strains
14 sigy_exp = data(:,4); % experimental stresses
15
16 % define initial point, lower bound and upper bound
17 [x0,lb,ub] = loadMaterialProperties();
18
19 % set the constraints
20 A = [0 0 0 0 0 0 0 0 0 0 -1 1 0 0 0 -ub(8) 0];
21 b = -ub(8);
22
23 %% Optimisation algorithm
24 options = psoptimset('Display','iter','OutputFcns',...
25     {@myOutputFcn},'SearchMethod',@MADSPositiveBasis2N,...
26     'CompleteSearch','on','MaxFunEvals',100000,...
27     'MaxIter',10000,'Cache','on');
28
29 [x,fval,exitflag,output] = patternsearch(@(x) objFun(x,...
30     sigy_exp,t_exp,tmax,nu),x0,A,b,[],[],lb,ub,[],options);
31
32 save('results.mat');

```

The objective function script begins by writing the current value of the material properties to a data file so that it can be read by the finite element implementation of the constitutive model. The *writeMaterialData* function can be found in Listing C.4 The finite element program is then run by MATLAB and the stress strain results read. The numerical data is then linearly interpolated at the corresponding time values from the input experimental data using the built in MATLAB function *interp1*. Finally, the objective function is evaluated as per Equation 6.14 and its value returned to the optimisation function.

Listing C.2: Objective Function Script

```

1 function f = objFun(x,sigy_exp,t_exp,tmax,nu)
2     % write current material properties to data file
3     writeMaterialData(x,nu,tmax);
4
5     % run the analysis
6     cmd = './vevpd-opt *.pro';
7     [status,~] = system(cmd);
8
9     % load the analysis results
10    try
11        resultData = dlmread('curve.dat');
12        dataRead = true;
13    catch
14        disp('Could not read data');
15        dataRead = false;
16    end
17
18    if dataRead

```

```

19     % extract result points
20     sigy_num = interp1(resultData(:,1),resultData(:,3),t_exp)
        / 1e6;
21
22     % set value for least squares to zero
23     f = 0;
24
25     % loop through time values up to tmax
26     for i = 1:find(t_exp>tmax,1)-1
27         % ensure the data point was interpolated properly
28         % first value (NaN) is zero stress
29         if isnan(sigy_num(i))
30             x = 0;
31         else
32             x = sigy_num(i);
33         end
34
35         % compute square of difference
36         f = f + (sigy_exp(i) - x) * (sigy_exp(i) - x);
37     end
38 else
39     f = Inf;
40 end
41 end

```

Listing C.3: Load Material Properties Script

```

1 function [x0,lb,ub] = loadMaterialProperties()
2     % initial optimisation properties
3     x0 = zeros(17,1); % preallocate initial vector
4     x0(1) = 1.53515e+09; % long term elastic modulus;
5     x0(2) = 8.23828e+07; % VE bulk stiffness 1
6     x0(3) = 1.60115e+08; % VE bulk stiffness 2
7     x0(4) = 1.42421e+08; % VE bulk stiffness 3
8     x0(5) = 5.24370e+04; % VE bulk time 1
9     x0(6) = 8.41436e+03; % VE bulk time 2
10    x0(7) = 4.90550e+03; % VE bulk time 3
11    x0(8) = 2.39632e+07; % sigma0
12    x0(9) = 1.88111e+00; % d_ve
13    x0(10) = 4.79789e+00; % m_ve
14    x0(11) = 9.67221e+07; % sigmaT factor 1
15    x0(12) = 2.42679e+07; % sigmaT factor 2
16    x0(13) = 4.05178e-02; % sigmaT factor 3
17    x0(14) = 2.93554e+04; % eta_p
18    x0(15) = 6.62500e+00; % m_p
19    x0(16) = 1.25000e-01; % c2
20    x0(17) = 1.25000e-01; % c3
21
22    % lower bound
23    lb = zeros(17,1); % preallocate initial vector

```

```

24     lb(1) = 1000e6; % long term elastic modulus;
25     lb(2) = 1e6; % VE bulk stiffness 1
26     lb(3) = 1e6; % VE bulk stiffness 2
27     lb(4) = 1e6; % VE bulk stiffness 3
28     lb(5) = 1e-3; % VE bulk time 1
29     lb(6) = 1e-3; % VE bulk time 2
30     lb(7) = 1e-3; % VE bulk time 3
31     lb(8) = 5e6; % sigma0
32     lb(9) = 1; % d_ve
33     lb(10) = 0.1; % m_ve
34     lb(11) = 20e6; % sigmaT factor 1
35     lb(12) = 0; % sigmaT factor 2
36     lb(13) = 1e-8; % sigmaT factor 3
37     lb(14) = 1e3; % eta_p
38     lb(15) = 0.1; % m_p
39     lb(16) = 0; % c2
40     lb(17) = 10; % c3
41
42     % upper bound
43     ub = zeros(17,1); % preallocate initial vector
44     ub(1) = 3500e6; % long term elastic modulus;
45     ub(2) = 2e9; % VE bulk stiffness 1
46     ub(3) = 2e9; % VE bulk stiffness 2
47     ub(4) = 2e9; % VE bulk stiffness 3
48     ub(5) = 1e6; % VE bulk time 1
49     ub(6) = 1e6; % VE bulk time 2
50     ub(7) = 1e6; % VE bulk time 3
51     ub(8) = 60e6; % sigma0
52     ub(9) = 1000; % d_ve
53     ub(10) = 20; % m_ve
54     ub(11) = 200e6; % sigmaT factor 1
55     ub(12) = 200e6; % sigmaT factor 2
56     ub(13) = 0.1; % sigmaT factor 3
57     ub(14) = 1e9; % eta_p
58     ub(15) = 20; % m_p
59     ub(16) = 0.7; % c2
60     ub(17) = 1e4; % c3
61 end

```

Listing C.4: Write Material Properties Script

```

1 function writeMaterialData(x,nu,tmax)
2     fout = fopen('material.dat', 'w'); % open a file for output
3
4     % print maximum analysis time
5     fprintf(fout, ['control.runWhile = t<',num2str(tmax),';\n']);
6
7     % print long term properties
8     fprintf(fout, ['model.model.bulk.material.eInfGlass = ', ...
9         num2str(x(1), '%.5e'),';\n']);

```

```
10 fprintf(fout, ['model.model.bulk.material.nuInfGlass = ', ...
11             num2str(nu, '%.5e'), ';\n']);
12
13 % print viscoelastic properties
14 fprintf(fout, 'model.model.bulk.material.kStiffsGlass = [ ');
15 for i = 1:3
16     fprintf(fout, num2str(x(1+i), '%.5e'));
17     if i == 3
18         fprintf(fout, ' ];\n');
19     else
20         fprintf(fout, ', ');
21     end
22 end
23
24 fprintf(fout, 'model.model.bulk.material.kTimes = [ ');
25 for i = 1:3
26     fprintf(fout, num2str(x(4+i), '%.5e'));
27     if i == 3
28         fprintf(fout, ' ];\n');
29     else
30         fprintf(fout, ', ');
31     end
32 end
33
34 fprintf(fout, 'model.model.bulk.material.gTimes = [ ');
35 for i = 1:3
36     fprintf(fout, num2str(x(4+i), '%.5e'));
37     if i == 3
38         fprintf(fout, ' ];\n');
39     else
40         fprintf(fout, ', ');
41     end
42 end
43
44 % compute shear stiffnesses
45 gFac = 3 * (1 - 2 * nu) / (2 * (1 + nu));
46
47 fprintf(fout, 'model.model.bulk.material.gStiffsGlass = [ ');
48 for i = 1:3
49     fprintf(fout, num2str(x(1+i)*gFac, '%.5e'));
50     if i == 3
51         fprintf(fout, ' ];\n');
52     else
53         fprintf(fout, ', ');
54     end
55 end
56
57 % print nlve properties
58 fprintf(fout, ['model.model.bulk.material.sigma0Glass = ', ...
```

```

59     num2str(x(8), '%.5e'),';\n']);
60     fprintf(fout, ['model.model.bulk.material.d = ', ...
61     num2str(x(9), '%.5e'),';\n']);
62     fprintf(fout, ['model.model.bulk.material.mve = ', ...
63     num2str(x(10), '%.5e'),';\n']);
64
65     % print vp properties
66     fprintf(fout, ['model.model.bulk.material.sigmaTGlass =
        ',formatExp(x(11)),'-',formatExp(x(12)),'*exp(-x/',formatExp(x(13)),'');\
        n']);
67     fprintf(fout, ['model.model.bulk.material.sigmaCGlass =
        ',formatExp(x(11)),'-',formatExp(x(12)),'*exp(-x/',formatExp(x(13)),'');\
        n']);
68     fprintf(fout, ['model.model.bulk.material.eta = ', ...
69     num2str(x(14), '%.5e'),';\n']);
70     fprintf(fout, ['model.model.bulk.material.mp = ', ...
71     num2str(x(15), '%.5e'),';\n']);
72
73     % print remaining nlve properties
74     fprintf(fout, ['model.model.bulk.material.c2 = ', ...
75     num2str(x(16), '%.5e'),';\n']);
76     fprintf(fout, ['model.model.bulk.material.c3 = ', ...
77     num2str(x(17), '%.5e'),';\n']);
78
79     fclose(fout); % close file
80 end

```

Second Global Optimisation Method

The second global optimisation method is identical to the first method apart from a few exceptions. To distinguish loading from unloading, the gradient of the experimental stress curve is evaluated with the *gradient* function. Further, the objective function in Line 36 in Listing C.2 is modified to limit the optimisation to stresses above 50 MPa and the loading branches. The changes are summarised in Listing C.5 below.

Listing C.5: Modified Objective Function Script

```

1 % evaluation of gradient for distinguishing loading from
    unloading
2 grad_sig_y = gradient(sigy_exp);
3
4 % Modified objective function
5 if grad_sig_y(i) > 0 && sigy_exp(i) > 50
6     f = f + (sigy_exp(i) - x) * (sigy_exp(i) - x);
7 end

```



Experimental Data

In this appendix, the dimensions of the experimental specimens and the raw load displacement data for the creep tests are presented.

Creep Test Specimen Dimensions

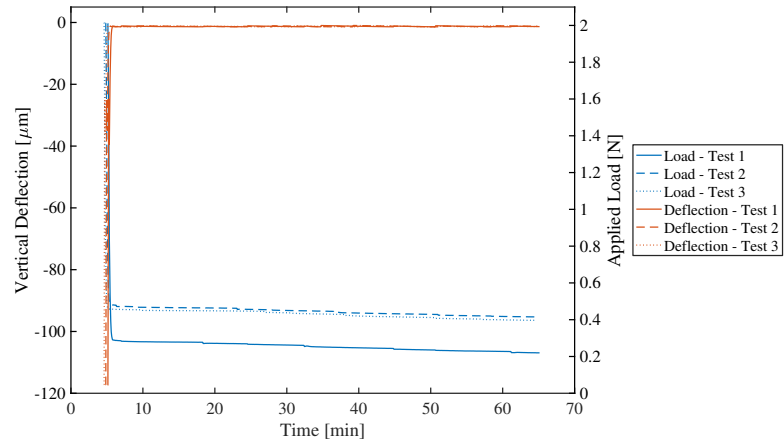
Table D.1 presents the dimensions for each specimen used in the creep tests.

Temperature $T = 25^{\circ}\text{C}$	Average Width	Average Thickness
Specimen 1	9.173 mm	2.872 mm
Specimen 2	9.670 mm	2.840 mm
Specimen 3	9.553 mm	2.860 mm
Temperature $T = 75^{\circ}\text{C}$	Average Width	Average Thickness
Specimen 1	9.287 mm	2.928 mm
Specimen 2	9.610 mm	2.860 mm
Specimen 3	9.593 mm	2.867 mm
Temperature $T = 100^{\circ}\text{C}$	Average Width	Average Thickness
Specimen 1	9.943 mm	2.853 mm
Specimen 2	9.017 mm	2.873 mm
Specimen 3	9.393 mm	2.860 mm

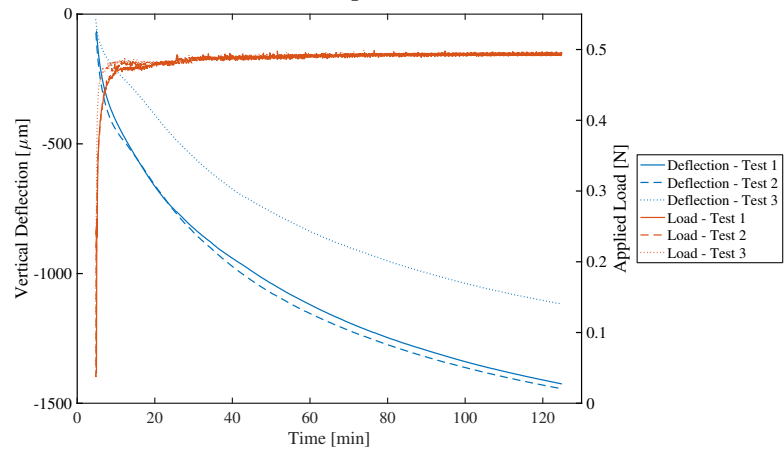
Table D.1: Dimensions of the epoxy resin specimens used in the creep test.

Raw Creep Data

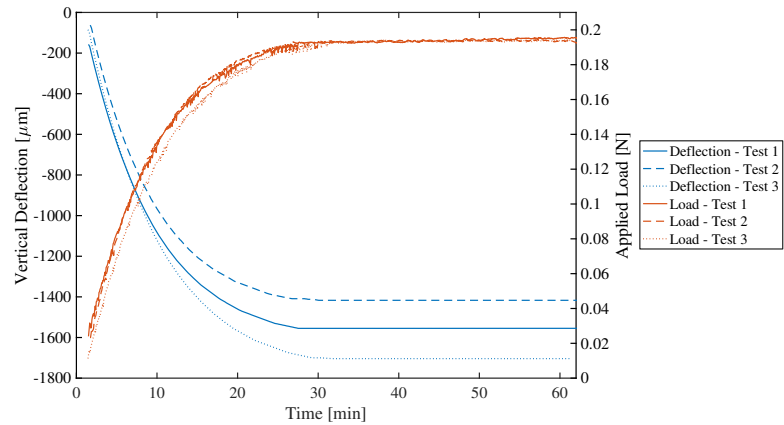
Figure D.1 presents the raw load displacement data obtained from the creep test. This data is used to determine the elastic modulus through the application of Equation 4.1.



(a) Raw load and displacement data for $T = 25^\circ\text{C}$.



(b) Raw load and displacement data for $T = 75^\circ\text{C}$.



(c) Raw load and displacement data for $T = 100^\circ\text{C}$.

Figure D.1: Raw experimental data from the creep test.

Raw Stress Relaxation Data

Figure D.2 presents the raw load displacement data obtained from the failed stress relaxation tests at a temperature of 75°C.

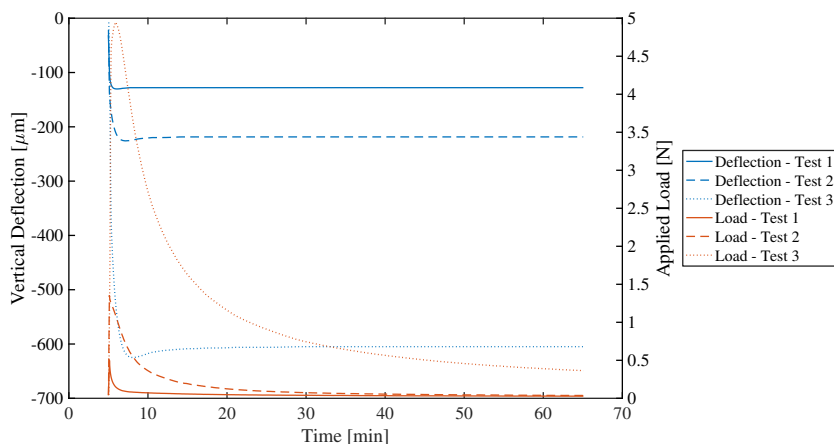


Figure D.2: Raw experimental data from the failed stress relaxation tests at 75°C.

Figure D.2 shows that the chosen displacements in the first two tests resulted in forces that were too small to be accurately recorded by the DMA machine after relaxation of the stress. The third test was performed at an increased imposed displacement and resulted in a force that was higher than the resolution of the DMA machine so could be recorded with confidence. However, upon inspection of the sample it was clear that significant plastic deformation had occurred at the chosen imposed displacement, see Figure 4.4. As a result, it was determined that the stress relaxation test was not the most suitable test for determining the long term elastic properties of epoxy resins at elevated temperatures and as such, a creep test was performed.